

Physik in ultrakurzen und ultraintensiven Feldern

Habilitationsschrift

zur Erlangung des akademischen Grades
doktor rerum naturalium habilitatis (Dr. rer. nat. habil.)

vorgelegt dem Rat der Physikalisch-Astronomischen Fakultät
der Friedrich-Schiller-Universität Jena

von Dr. sc. nat. Heinrich Schwoerer
geboren am 19. Oktober 1964 in Waiblingen.

Gutachter

1. Prof. Dr. Roland Sauerbrey
2. Prof. Dr. Hans-Christoph Wolf
3. Prof. Dr. Klaus Witte

Tag der öffentlichen Verteidigung: 10. Dezember 2002

Tag des öffentlichen Vortrags (Lehrprobe): 17. Dezember 2002

Inhaltsverzeichnis

1 Einleitung	1
2 Moleküle	3
3 Atome	6
3.1 EUV-Strahlung	6
3.2 K _α -Strahlung	8
3.3 Harte Röntgenstrahlung, relativistische Plasmaphysik	10
4 Kerne	12
4.1 Photoneutronen	12
4.2 Deuteriumfusion	13
4.3 Spaltung schwerer Kerne	14
5 Laser	16
5.1 Das Jenaer 15 Terawatt-Lasersystem	16
5.2 Diagnostik eines TW-Laserpulses	17
6 Zukunft	19
7 Veröffentlichungen	25
7.1 Moleküldynamik und kohärente Kontrolle	25
7.2 Wechselwirkung intensiver Laserfelder mit Materie	46
7.3 Apparatives	76
7.4 Weitere eigene Veröffentlichungen	89

1 Einleitung

Licht, wie wir es aus dem täglichen Leben kennen, ist dauerhaft und schwach. Eine Glühlampe beispielsweise oder die Sonne strahlen kontinuierlich Licht ab. Man kann sie mit bloßem Auge betrachten. Ihr Licht setzt sich aus Photonen zusammen, deren Energie gerade ausreicht, um elementare biologische Prozesse durch photoinduzierte Reaktionen mit Energie zu versorgen, meist ohne dabei Moleküle zu zerstören, Atome zu ionisieren oder gar Atomkerne anzuregen.

Ich werde in dieser Arbeit zeigen, daß man ebenfalls mit sichtbarem Licht, allerdings nicht mit kontinuierlichem, sondern nun mit extrem kurzen Lichtpulsen, ebendiese elementare intramolekulare Dynamik beobachten und sogar steuern kann. Und mit nahezu demselben experimentellen Aufbau kann man das Geschehen untersuchen, das sich abspielt, wenn man Licht einer so hohen Intensität erzeugt, daß Atome bis zur Nacktheit ionisiert und Atomkerne gespalten werden.

Die zum Beispiel durch Sonnenlicht ausgelösten mikroskopischen Prozesse, wie intramolekularer Energie- oder Ladungstransfer spielen sich typischerweise innerhalb von einer Pikosekunde ab. Um solche photoinduzierten Elementarprozesse in Molekülen in Echtzeit zu beobachten und insbesondere um einen aktiven Einfluß auf sie zu gewinnen, muß die experimentelle zeitliche Auflösung an die mikroskopische Dynamik angepaßt werden. Eine elegante und konzeptionell einfache Methode ist es, hierfür Laserpulse zu verwenden, deren Dauer kürzer ist, als die intramolekularen Prozesse. Die ultrakurzen Pulse können einerseits impulsiv Molekuldynamik starten, sie gezielt unterbrechen und sie auch umlenken und andererseits diese wie in einem sehr schnellen Stroboskop beobachtbar machen. Die ultrakurzen Laserpulse dienen hier also als diagnostisches Werkzeug zur Untersuchung molekularer Vorgänge.

Konzentriert man ein wenig mehr Energie, sagen wir 1 Joule, in einem solchen ultrakurzen Laserpuls, so wird er zum Präparator eines auf der Erde exklusiven Zustandes: Im Fokus eines solchen Laserpulses herrscht eine Flußdichte von über 10^{38} Photonen pro Sekunde und Quadratzentimeter, oder eine Lichtintensität von 10^{20} W/cm^2 . Diese Intensität ist so hoch, als würde man das gesamte auf die Erde fallende Sonnenlicht auf eine Fläche von einem Zehntel eines Quadratmillimeters bündeln. Materie am Ort des Laserfokus wird in ein extrem heißes und meist dichtes Plasma verwandelt. Dieses Plasma emittiert Röntgenlinienstrahlung bei der Rekombination seiner Ionen. Bei sehr hohen Intensitäten wird das magnetische Feld des Laserlichts dominant und treibt die Plasmaelektronen in Propagationsrichtung des Lichts. Die Elektronen werden dabei bis auf relativistische Energien beschleunigt.

Dringen diese heißen Elektronen in eine Probe ein, so können darin Atome bis in tiefe Schalen ionisiert werden, und es entsteht zum Beispiel sehr effizient K_α -Strahlung. In inelastischen Stößen wird Bremsstrahlung mit Photonenergien bis zu vielen Megaelektronenvolt erzeugt. Diese Bremsstrahlung kann ihrerseits elementare Kernreaktionen wie Abspaltung eines Neu-

trons oder Spaltung großer Kerne induzieren.

Und schließlich kann durch hochenergetische Stöße im heißen Laserplasma Kernverschmelzung zum Beispiel zweier Deuteriumkerne stattfinden.

Alle Emissionen laserproduzierter Plasmen, Strahlung und Teilchen, tragen wertvolle, sich ergänzende Informationen über die Wechselwirkung des intensiven Lichtfeldes mit der Materie und helfen, die Erzeugung und die Eigenschaften relativistischer Laserplasmen zu verstehen. Darüber hinaus finden viele der Emissionen interessante Anwendungen: Röntgenlicht in der Lithographie und in der Röntgenbeugung mit hoher Zeitauflösung, in Zukunft auch in der nicht-linearen Röntgenoptik. Mit der hochenergetischen Bremsstrahlung lassen sich schwere Atomkerne spalten und Neutronen freisetzen, mit denen wiederum Transmutationen aktiver in stabile oder stabiler in aktive Kerne möglich sind.

Die in dieser Arbeit beschriebenen Experimente beschäftigen sich mit beiden Aspekten, sowohl mit der Diagnostik laserproduzierter Plasmen als auch mit der Suche nach Anwendungen ihrer Emissionen.

Die folgenden drei Kapitel sind nach der Größe der untersuchten Systeme geordnet: In Kapitel 2: Moleküle, beschreibe ich meine Arbeiten zur zeitaufgelösten Molekülspektroskopie, die zwischen 1995 und 1998 am Institut für Physikalische Chemie der Universität Würzburg entstanden sind. Die Experimente zur Erzeugung und Charakterisierung von Röntgenstrahlung aus laserproduzierten Plasmen (Kapitel 3: Atome) und die Experimente zu laserinduzierter Kernphysik (Kapitel 4: Kerne) habe ich am Institut für Optik und Quantenelektronik der Universität Jena durchgeführt. Es schließt sich noch ein kurzes Kapitel über den Jenaer TeraWatt-Laser an, da dieser unter meiner Leitung zu einem der intensivsten Laser der Welt ausgebaut wurde. In Kapitel 6 werde ich zeigen, wie sich die zunächst sehr unterschiedlich erscheinenden Gebiete der zeitaufgelösten Molekülspektroskopie und der Laserplasmaphysik gegenseitig befrieden und ergänzen können und wie sie hoffentlich auch in meiner zukünftigen Arbeit zusammenfinden werden. In Kapitel 7 sind ausgewählte Veröffentlichungen, auf die ich in den vorangegangenen Kapiteln Bezug genommen habe, abgedruckt, gefolgt von einer Liste meiner übrigen Veröffentlichungen. Die Seitenangaben im folgenden beziehen sich auf diese Arbeit.

2 Moleküle

Ultrakurze Laserpulse gestatten die Untersuchung intramolekularer Dynamik mit einer Zeitauflösung, die gleich ihrer Pulsdauer ist. Laserpulse, deren Wellenlänge meist im sichtbaren bis nahen infraroten Spektralbereich liegen, induzieren dabei elektronische Übergänge im Molekül. Aufgrund ihrer kurzen Dauer und damit spektralen Breite erzeugen sie kohärente Überlagerungen von einigen bis vielen vibronischen Zuständen, regen also ein Schwingungswellenpaket an. Durch Kombination mehrerer ultrakurzer Pulse geeigneter Wellenlänge und geeigneter zeitlicher Abstände lässt sich intramolekulare Dynamik beobachten und beeinflussen. Ein erster Laserpuls (Pumppuls) regt das Molekül elektronisch an und erzeugt ein Schwingungswellenpaket, siehe Skizze links. Dieses entwickelt sich frei, das Molekül schwingt, solange bis ein zweiter Laserpuls, der Probepuls, dieses Wellenpaket in einen weiteren elektronischen Zustand transformiert. Dieser Probezustand kann zum Beispiel ein fluoreszierender sein oder ein ionischer. Die Wahrscheinlichkeit des zweiten Übergangs ist im allgemeinen von der aktuellen Position des Wellenpakets auf der Potentialfläche abhängig: Die Franck-Condon-Faktoren, also die räumlichen Überlappintegrale zwischen den Schwingungszuständen in Zwischen- und Probezustand sind von den aktuellen Kernkoordinaten abhängig und bestimmen somit die Wahrscheinlichkeit des Prozesses. Die Bevölkerung des Probezustandes muß nun gemessen werden, zum Beispiel durch Detektion einer nachfolgenden Fluoreszenz oder durch die Messung der Anzahl erzeugter Ionen. Der Nachweis der Bevölkerung des Probezustandes kann sehr langsam erfolgen. Entscheidend für die Zeitauflösung der Beobachtung der Wellenpaketdynamik sind die Pulsdauer der Anregungen und die Genauigkeit des zeitlichen Abstandes zwischen Pump- und Probepuls. Durch häufige Wiederholung des gleichen Experiments unter Variation der Pulsabstände kann nun die Kernbewegung beobachtet werden.

Der erste und wichtigste Schritt zu optimaler Laserkontrolle des Pfades und der Ausbeute vieler chemischer Reaktionen ist die selektive Bevölkerung angeregter Molekülschwingungen des Reaktanten. Angeregte Schwingungszustände können als Übergangszustände zum angestrebten Produktzustand agieren, wenn sich während der kohärenten Entwicklung des Wellenpaketes Franck-Condon-Fenster zum Produktzustand öffnen. Zum Beispiel erlauben gebundene Schwingungszustände über der Barriere eines Doppelmuldenpotentials zweier Isomere den Übergang von einem Isomer zum anderen. Unimolekulare Reaktionen mit verschiedenen möglichen Endzuständen können durch Anregung eines Schwingungswellenpaketes geeigneter Energie und Form auf einen vorgewählten Reaktionspfad geleitet werden. Und schließlich können intramolekulare Schwingungsrelaxationsprozesse im Detail studiert werden, entweder zustandsselektiv oder auch zeitaufgelöst.

Zu Beginn meiner Arbeiten zur zeitaufgelösten Moleküldynamik waren einige solcher Experimente zur Femtosekunden-Schwingungswellenpaket-Spektroskopie bekannt. Diese Untersuchungen blieben jedoch auf Grund der Photonenergie der eingesetzten ultrakurzen Laserpulse

auf die Beobachtung elektronisch angeregter Zuständen beschränkt, die zum einen theoretisch schwierig zu beschreiben und zum anderen in der Natur nur selten relevant sind. Schwingungswellenpakete im elektronischen Grundzustand hingegen waren noch nicht gezielt angeregt worden.

Ein Ansatz zur selektiven und optimalen Bevölkerung von Schwingungswellenpaketen in elektronischen Grundzuständen wurde 1985 von Tannor und Rice vorgeschlagen [17]: Ein lokalisierter Schwingungswellenpaket wird mit einem ultrakurzen Laserpuls in einem elektronisch angeregten Zustand des betrachteten Moleküls erzeugt. Dieses Wellenpaket beginnt auf seiner elektronischen Potentialfläche so lange zu laufen, bis es ein großes Franck-Condon-Fenster in den gewünschten Zielzustand im elektronischen Grundzustand erreicht und wird dann mit einem zweiten ultrakurzen Laserpuls in dieses abgeregelt. Wir haben dieses klassische Tannor-Rice-Schema, das die konzeptionelle Grundlage eines jeden coherent-control-Experiments ist, erstmals experimentell realisiert. Dazu haben wir ein einfaches zweiatomiges Molekül gewählt, nämlich das Kaliumdimer, weil dieses wie alle Alkalioligomere große elektronische Übergangsmomente hat und seine Schwingungsperioden von unserem Laser zeitlich aufgelöst werden konnten. Das Vorgehen bestand aus drei Schritten: Zunächst die Untersuchung der Dynamik in Zwischenzuständen ([1], S. 26), zweitens die Erzeugung eines Wellenpaketes im elektronischen Grundzustand ([2], S. 32) und drittens die erstmalige experimentelle Demonstration eines Tannor-Rice-Schemas zur Optimierung der Besetzung im Grundzustand ([3], S. 38).

Die Anregung der Grundzustandsschwingung erfolgte über einen mit einem elektronischen Zustand des Kaliumdimers ($|B\rangle$) resonanten Zweiphotonenprozeß. Da die Effizienz des Mechanismus von der kohärenten Entwicklung dieses Zwischenzustandes bestimmt wird, haben wir zunächst diesen untersucht. In [1], Seite 26, ist die kohärente Dynamik eines K_2 -Moleküls in seinem $|B\rangle$ -Zustand detailliert beschrieben. Besondere Aufmerksamkeit haben wir dabei dem Verständnis der Detektion des Wellenpaketes gewidmet. Das Kaliumdimer in $|B\rangle$ wurde mit einem variabel verzögerten ultrakurzen Probepuls ionisiert. Mit Hilfe zeitabhängiger quantenmechanischer Rechnungen haben wir gezeigt, daß für die Selektivität des Ionensignals auf die Position des $|B\rangle$ -Wellenpaketes sowohl die Franck-Condon-Faktoren als auch ein koordinaten-abhängiges Übergangsdipolmoment verantwortlich sind (siehe Abschnitt IV in [1], S. 29). Der letzte Aspekt wurde in dieser Arbeit zu erstenmal experimentell beobachtet.

Schwingungswellenpakete im elektronischen Grundzustand wurden über einen stimulierten Ramanprozeß mit zwei zunächst gleichzeitigen Laserpulsen unterschiedlicher Wellenlänge, dem Pump- und dem Stokespuls, erzeugt. Die Energiedifferenz der beteiligten Photonen ergibt die mittlere Energie des Schwingungswellenpaketes im elektronischen Grundzustand. Dieses Schwingungswellenpaket im Grundzustand wird geprobt mit einem zeitverzögerten ionisierenden Probepuls. Durch eine Resonanzverstärkung auf dem Ionisationspfad, die auf die Kernabstandsordinate selektiv ist, bildet das Ionensignal die Primärschwingung im elektronischen Grundzustand ab, siehe Bild 1 in [2], S. 33.

Bild 3 in [2], S. 35 zeigt das detektierte Ionensignal als Funktion der Zeit zwischen dem Stokespuls und dem Probepuls. Eine Fouriertransformation der Oszillationen (Bild 4, S. 36) offenbart, daß sie im wesentlichen aus Grundzustandswellenpaketen mit Beiträgen bei 92 cm^{-1} und bei 88 cm^{-1} bestehen. Das Signal bei höherer Energie stammt von einem kalten Schwingungswellenpaket um die Schwingungszustände $v' = 0$ und $v' = 1$, das durch An- und Abregung mit Photonen gleicher Wellenlänge generiert wird. Das in diesem Experiment interessante Signal ist das bei niedrigerer Energie, das von einem durch einen stimulierten Ramanprozeß erzeugten heißen Wellenpaket um $v' = 6$ stammt (siehe auch Bild 1 in [3], S. 40). Diese erstmalige experimentelle Beobachtung kohärenter Schwingungsdynamik im elektronischen Grundzustand ist in [2] beschrieben.

Aus den einleitenden Gedanken und diesen beiden Vorexperimenten folgt nun fast zwingend die nur noch kleine Variation zur großen Tat, die systematische Variation der Zeit zwischen Pump- und Stokespuls bei fester Wellenlänge und der Vergleich der jeweils generierten Population im heißen Grundzustandswellenpaket. Man läßt also das kohärente Wellenpaket sich im Zwischenzustand bis zu einem Zeitpunkt frei entwickeln, an dem der Überlapp mit dem angestrebten Zielzustand maximal ist. In diesem Moment regt man es mit dem ultrakurzen Stokespuls dorthin ab.

In Bild 7 in [3], S. 43 ist die Besetzung eines Schwingungswellenpaketes mit mittlerer Schwingungsquantenzahl 11 im elektronischen Grundzustand als Funktion der Pump-Stokes-Verzögerung aufgetragen. Dieses Schwingungswellenpaket kann ganz offensichtlich 150 fs und 650 fs nach Anregung in den Zwischenzustand optimal erzeugt werden. Zu diesen Zeiten ist das Kaliumdimer gerade gestreckt. Damit ist uns der erstmalige saubere experimentelle Nachweis der Tannor-Rice-Methode zur selektiven Erzeugung von Schwingungswellenpaketen im elektronischen Grundzustand gelungen.

Seinerzeit und vereinzelt auch noch heute, wurden und werden viele methodisch wichtige Experimente zur Femtosekundenchemie und -physik an einfachen Molekülen, nämlich zum Beispiel homonuklearen zweiatomigen Molekülen getestet. Erst darauf aufbauend können die entwickelten experimentellen Schemata und theoretischen Modelle auf komplexere Systeme mit unbekannter intramolekularer Dynamik angewendet werden.

In den Experimenten zur Moleküldynamik haben stets wenige Photonen aus dem Laserpuls, nämlich eins, zwei oder drei, einen elektronischen Prozeß induziert. Demzufolge mußte die Laserintensität klein gehalten werden; die Wellenlänge der bis zu drei verschiedenen Pulse hingegen mußte über den sichtbaren Wellenlängenbereich flexibel sein.

Im folgenden werden Elektronenanregungen beschrieben, in denen nicht einzelne, sondern zunächst hunderte, dann tausende und schließlich millionen von Laserphotonen einen Prozeß induzieren, primär nämlich die Beschleunigung von Elektronen.

3 Atome

In diesem Kapitel werde ich drei Experimente zu lasererzeugter Röntgenstrahlung vorstellen. Diese entsteht, wenn Atome von einem intensiven Laserfeld bis in innerste Schalen ionisiert wurden und wenn von diesem Laserfeld beschleunigte Elektronen Bremsstrahlung erzeugen.

Ab Lichtintensitäten über etwa 10^{10} W/cm^2 wird Materie durch Feldionisation und Multiphotonenabsorption ionisiert. Die vom Licht beschleunigten Elektronen heizen durch Stöße das entstandene Plasma auf hohe Temperaturen und ionisieren die Materie weiter. Diese Stoßabsorption oder inverse Bremsstrahlung ist der dominante Absorptionsmechanismus für Lichtintensitäten unter 10^{16} W/cm^2 . Darüber bestimmt die sogenannte Resonanzabsorption den Energietransfer von Licht in das Plasma: an Orten, an denen die Plasmafrequenz gleich der Lichtfrequenz ist, also an Orten mit der sogenannten kritischen Plasmadichte, wird resonant Energie in Plasmaschwingungen eingekoppelt.

Die Absorption des Laserlichts durch das Plasma ist bei allen Intensitäten von den Eigenschaften des Plasmas, wie seiner Elektronendichte und seinem Dichtegradienten, abhängig. Um das Aufheizen der Materie zu steuern, ist es aus diesem Grund häufig vorteilhaft, zunächst mit einem kleinen Laservorpuls ein sogenanntes Vorplasma zu erzeugen, dieses sich eine bestimmte Zeit lang entwickeln zu lassen und es dann mit dem Hauptlaserpuls zu heizen. Dieser Trick wird in den folgenden Kapiteln beschriebenen Experimenten mehrfach angewandt.

Sekundär entsteht nun Strahlung: weiche Röntgenlinienstrahlung bei Rekombination der Plasmaionen, mittelharte Linienstrahlung aus inneren Schalen kalter Atome und Bremsstrahlung bis zu sehr hohen Energien durch inelastische Stöße von Elektronen mit Atomen.

Die Experimente in diesem Kapitel sind nach aufsteigender Röntgenphotonenenergie geordnet. Im Unterschied zu den Moleküldynamik-Experimenten des vorigen Kapitels sind die meisten dieser Experimente noch in vollem Gang.

3.1 EUV-Strahlung

Liniенstrahlung im extrem ultravioletten Spektralbereich (EUV) um 13 nm wird in naher Zukunft die Strahlung für die lithographische Massenproduktion kleinster Halbleiterbauelemente werden. Während für die meisten Prozeßschritte dieser zukünftigen Lithographietechnologie Lösungen zu erkennen sind, ist über die Technologie der eigentlichen Strahlungsquelle noch nicht entschieden. Neben Synchrotron und Entladungsplasmen kommen lasererzeugte Plasmen von Elementen mit Emissionslinien um 13 nm in Frage. Im Rahmen einer nationalen Evaluierung der Möglichkeiten und Chancen verschiedener EUV-Lichtquellenkonzepte haben wir Experimente zur absoluten Messung der Umwandlungseffizienz von Laserstrahlung in EUV-Strahlung an einem Sauerstoffplasma durchgeführt. Dabei haben wir insbesondere den Einfluß

der zeitlichen Laserpulsstruktur auf die Konversionseffizienz untersucht [8], S. 47. Hinter diesem Experiment steht die Vorstellung, daß für eine maximale Strahlungsausbeute zunächst ein optimal Laserlicht absorbierendes Plasma erzeugt werden muß, das zum richtigen Zeitpunkt mit einem kurzen Laserpuls aufgeheizt wird und 13 nm Licht abstrahlt.

Für diese Versuche haben wir eine Wassertröpfchenquelle in einer Hochvakuumanlage aufgebaut, mit der mit einer Wiederholrate von 1 MHz 20 μm große H_2O -Tröpfchen erzeugt werden können. Diese Tröpfchen werden von Laserpulsen aus dem Jenaer TeraWatt-Ti:Saphir-Lasersystem, siehe Kapitel 5, so beschossen, daß sie vollständig ausgeleuchtet sind, wenig Licht sie jedoch verfehlt, siehe Abbildung 1 in [8], S. 48. In den ersten Experimenten wurden alle Parameter des Laserpulses wie Wellenlänge, Fokussierung und Energie konstant gehalten. Lediglich die Pulsdauer wurde zwischen 200 fs und 6 ns, also über mehr als vier Größenordnungen variiert. Die erzeugte EUV-Strahlung wurde mit einem bei der Physikalisch-Technischen Bundesanstalt in Berlin kalibrierten Transmissionsgitterspektrometer aufgezeichnet. Abbildung 5 in [8], S. 50, ist die EUV-Ausbeute in absoluten Einheiten dargestellt (% im vollen Raumwinkel in der 13 nm-Emissionslinie des fünffach geladenen Sauerstoffatoms, 4d \rightarrow 2p). Das Resultat zeigt für verschiedene Laserpulsenergien stets ein deutliches Maximum bei Pulsdauern um etwa 100 ps. Dies kann mit einfachen Plasmodynamikargumenten verstanden werden: Zu kurze Laserpulse (200 fs) werden im wesentlichen am noch überdichten Plasma reflektiert und tragen somit nicht zu seiner Aufheizung bei. Umgekehrt expandiert das bereits von der Vorderflanke eines langen Laserpulses (6 ns) erzeugte Plasma während der Dauer des Laserpulses so weit, daß seine Dichte unter die kritische Dichte für die Laserfrequenz sinkt und die hintere Flanke des Laserpulses durch das Plasma transmittiert wird, ohne absorbiert zu werden. Für in unserem Sinne mittlere Pulsdauern um 100 ps kann das Sauerstoffplasma hingegen am meisten Laserlicht absorbieren und damit ist auch die EUV Ausbeute am höchsten.

Neben der Pulsdauer von etwa 100 ps muß die Energie des Laserpulses auf das bestrahlte Tröpfchenvolumen abgestimmt werden. Für die hier verwendeten Wassertröpfchen mit einem Durchmesser von 20 μm ist die optimale Laserpulsenergie 50 mJ. Diese entspricht im wesentlichen der Summe der notwendigen Ionisationsenergie aller Sauerstoffatome und der Heizung des Plasmas auf eine Temperatur von etwa 30 eV, bei der das Strahlungsmaximum bei 13 nm liegt.

Die Arbeiten bestätigten die anfangs gestellte Hypothese, daß zunächst ein das Laserlicht optimal absorbierendes Plasma erzeugt werden muß, das dann von einem kurzen Laserpuls optimal geheizt werden kann. Dies ruft geradezu zwingend nach Einsatz eines Laservorpulses. In einem zweiten Experiment wurde somit zunächst mit einem wohl definierten Laservorpulse ein Plasma erzeugt. Nach einer variablen Zeit, während derer dieses Plasma frei expandieren kann, wurde der Hauptlaserpuls eingekoppelt, der die angestrebten fünffach geladenen Sauerstoffionen produziert. Der Einsatz des Vorpulses erhöht für alle Laserpulsdauern die Konversionseffizienz. Die größte Effizienzsteigerung und auch die höchste Konversionseffizienz von nahezu 2% wurde für Laserpulsdauern von 2 ps und einem Vorpulseabstand von 3 ns erreicht. Diese Messungen und

Vergleiche mit Plasmodynamik-Simulationen zeigen, daß Stoßabsorption im für die Laserwellenfrequenz unterdichten Plasma der wesentliche Absorptionsmechanismus für das Laserlicht ist.

Auf diese Weise konnte die Konversionseffizienz von Laserlicht in EUV-Strahlung um mehr als einen Faktor zehn gesteigert werden. Somit ist die Konversionseffizienz für Wasser und optimierte Pulsform durchaus anderen Targetkonzepten gleich oder gar überlegen. Die Plasmodynamiksimulationen reproduzieren dieses Resultat. Die Emissionsdauer der EUV-Strahlung aus der Rekombination äußerer Schalen von Plasmaionen ist durch die Dynamik und die Dichte des Plasmas bestimmt und somit nicht ultrakurz.

Die ersten Resultate sind bereits in Appl. Phys. B [8] veröffentlicht, die neueren werden in Kürze ebenfalls bei Appl. Phys. B zur Veröffentlichung eingereicht.

3.2 K_α-Strahlung

Die Elektronenenergien in lasererzeugten Plasmen reichen bei Lichtintensitäten von 10^{17} W/cm² bis weit über 100 keV. Diese schnellen Elektronen können also durch Stöße alle Atome selbst in der K-Schale ionisieren und somit Röntgenlinienstrahlung produzieren. Insbesondere kann sehr effizient K_α-Strahlung erzeugt werden, die aufgrund ihrer kurzen Emissionsdauer für einige Anwendungen wie zum Beispiel die zeitaufgelöste Röntgenbeugung interessant ist. In zwei grundlegenden Experimenten zur Vorplasmaabhängigkeit und zur Intensitätsabhängigkeit der K_α-Ausbeute zeigte es sich, daß diese Strahlungsquelle bei Photonenergien von einigen Kilo-elektronenvolt extrem hohe Röntgenintensitäten liefert, mit denen in Zukunft auch nichtlineare Prozesse realisierbar sein könnten, siehe Kapitel 6.

Die Vorplasmaabhängigkeit der K_α-Produktion wurde für die Elemente Silizium, Titan und Kobalt durchgeführt, indem, wie bei den EUV Experimenten, ein in zeitlichem Vorsprung und Intensität variabler Vorpuls eingesetzt wurde. Die dafür entwickelte voll automatisierte Vorpulseinheit ist in [4] beschrieben. Sowohl bei von Hand optimierten Parametern als auch bei Einsatz eines Optimierungsalgorithmus mit dem K_α-Signal als Rückkopplungssignal wurden Ausbeutensteigerungen von bis zum fünffachen erzielt (siehe Abbildung in [7]). Die optimalen Vorpulsabstände variieren von Element zu Element und liegen zwischen 50 ps und 150 ps. Diese in diesem Zusammenhang sehr langen Zeiten entsprechen so großen Plasmakalenlängen, daß die maximale K_α-Erzeugung nicht alleine durch Resonanzabsorption des Laserlichts im Vorplasma erklärt werden kann. Es scheint ein weiterer Mechanismus die K_α-Ausbeute zu erhöhen, der vermutlich eine relativistische Selbstfokussierung des Laserpulses im Vorplasma und damit eine Intensitätserhöhung und ein Aufsteilen des Plasmagradianten bewirkt.

Die Resultate sind bei Physical Review E veröffentlicht [7].

Die höchsten Röntgenflüsse haben wir durch Laserbeschuß einer 12 μm dünnen Titanfolie er-

reicht. Vor Beginn dieser Experimente war sowohl aus theoretischen [16] als auch aus experimentellen [13] Arbeiten bekannt, daß für laserproduzierte K_α-Strahlung aus dicken Proben eine optimale Laserintensität existiert, die im wesentlichen durch die Bedingung gegeben ist, daß die mittlere Energie bzw. die Temperatur der Plasmaelektronen etwa fünfmal höher sein sollte, als die Energie, die zur K-Schalenionisation aufgewendet werden muß. Diese Intensität beträgt bei dem von uns untersuchten Element Titan etwa 10^{17} W/cm², und wir haben bei dieser Intensität in der Tat ein lokales Maximum der K_α-Ausbeute gefunden. Es hat sich nun aber gezeigt, daß bei weiterer Erhöhung der Laserintensität bis über 10^{19} W/cm² nach Durchlaufen eines Minimums die K_α-Ausbeute wieder ansteigt (siehe Bild 3 in [9], S. 63). Dieser erstmals experimentell aufgetretene Befund läßt sich durch den bei relativistischen Elektronenenergien logarithmisch wieder ansteigenden Wirkungsquerschnitt der K_α-Produktion erklären: Das Feld eines relativistischen Elektrons ist transversal zu seiner Flugrichtung stärker als parallel zu dieser. Somit ist aus der Sicht des ruhenden, in der K-Schale gebundenen Elektrons das angreifende Feld höher als im Fall langsamer Stoßelektronen. Dieser relativistische Effekt wächst mit steigender Energie der Projektil. Die Wirkungsquerschnitte für K-Schalenionisation wurden seit den 70er Jahren mit Elektronenbeschleunigern systematisch für viele Elemente vermessen. Wir haben mit diesen Querschnitten ein detailliertes Modell der K_α-Produktion in einer dünnen Folie durch lasererzeugte relativistische Elektronen entwickelt. Mit der sinnvollen Annahme der Existenz einer Elektronentemperatur und dem Wissen um den Zusammenhang zwischen Elektronentemperatur und Laserintensität (siehe Abschnitt 3.3, Harte Röntgenstrahlung) lassen sich unsere zunächst überraschenden Resultate erklären, siehe auch Bild 5 in [9], S. 65.

Die experimentellen Ergebnisse und deren Erklärung wurden bei Europhysics Letters zur Veröffentlichung eingereicht [9].

Aus dem nur wenige $10 \mu\text{m}^3$ großen Quellvolumen werden pro Laserschuß bis zu 10^{12} Titan K_α-Photonen einer Energie von 4,5 keV emittiert. Leider, jedenfalls im Sinne einer Anwendung der K_α-Strahlung, emittiert das laserproduzierte Plasma nicht nur K_α-Strahlung, sondern auch andere Linienstrahlung und Bremsstrahlung und auch schnelle Elektronen und Ionen. Um eine reine K_α-Strahlungsquelle zu verwirklichen, haben wir einen monochromatisierenden, gekrümmten Röntgenspiegel eingesetzt, der die K_α-Strahlung aus der Laserplasmaquelle auf ein Target abbildet. Auf diesem konnten monochromatische Röntgenintensitäten von über 10^{10} W/cm² erreicht werden. Diese Strahlung ist inkohärent. Abschätzungen, die wir selbst und zusammen mit Herrn Fritzsche von der Universität Kassel gemacht haben, lassen nun hoffen, daß in diesen Feldern erstmals nichtlineare Prozesse mit Röntgenphotonen möglich sein sollten, siehe auch Kapitel 6.

3.3 Harte Röntgenstrahlung, relativistische Plasmaphysik

Erhöht man die Laserintensität bis auf die von unserem Laser maximal erzeugbare von 10^{20} W/cm² und plaziert ein Target mit hoher Kernladungszahl wie zum Beispiel Tantal in den Fokus, so wird ein Teil der Plasmaelektronen im intensiven Laserfeld auf suprathermische Energien von vielen MeV aufgeheizt und erzeugt durch Stöße mit den schweren Atomen des Targets Bremsstrahlung mit Photonenenergien ebenfalls bis zu vielen MeV.

Der Beschleunigung der Elektronen im Lichtfeld auf relativistische Energien liegt der folgende Mechanismus zu Grunde: In einem Lichtfeld einer Intensität von $2 \cdot 10^{18}$ W/cm² ist die transversale Schwingungsenergie eines freien Elektrons bereits so groß wie seine Ruheenergie. Somit kann die Wechselwirkung des relativistisch schnellen Elektrons mit dem Magnetfeld des Lichtes nicht mehr vernachlässigt werden. Dies führt zu einer Bewegung der Elektronen in Propagationsrichtung des Lichts. Die Bewegung der relativistischen Elektronen ist also gerichtet. Somit ist auch die von ihnen erzeugte hochenergetische Bremsstrahlung anisotrop. Dieses sogenannte ponderomotorische Potential skaliert mit der Wurzel der Laserintensität und erreicht bei 10^{20} W/cm² eine Elektronenenergie von etwa 5 MeV. Weiterhin wird das gesamte inhomogene Plasma durch Absorption des Laserlichts an der kritischen Dichte, durch die sogenannte Resonanzabsorption aufgeheizt. Resonanzabsorption führt bei Intensitäten über 10^{19} W/cm² ebenfalls zu relativistischen Energien der Plasmaelektronen. Sie ist im Detail stark von der Dichte und dem Dichtegradienten des Plasmas sowie von der Einfallrichtung und Polarisation des Laserlichts abhängig.

Zur Untersuchung dieser relativistischen Laserplasmen haben wir detaillierte Experimente zur spektralen und räumlichen Verteilung der hochenergetischen Elektronen- und Photonenemission dieser Plasmen durchgeführt: Ein Laserpuls mit einer Intensität von 5×10^{18} W/cm² (damals war er noch nicht so intensiv wie heute) wurde unter 45° und parallel polarisiert auf ein Tantalblech fokussiert. Mit 12 Spektrometern haben wir das gesamte Strahlungsfeld des Plasmas in der Ebene von Laserstrahl und Probennormaler vermessen. Die beiden wesentlichen Resultate dieser Experimente sind, daß erstens die Temperatur der heißen Elektronen dem durch das ponderomotorische Potential erwarteten Wert von etwa 500 keV entspricht (siehe Abbildung 2 in [5], S. 69) und daß zweitens die Emission der relativistischen Elektronen und der hochenergetischen Photonen stark anisotrop ist, Abbildungen 3 und 4 in [5] S. 70. Diese Anisotropie wurde dabei zum erstenmal experimentell festgestellt. Energie- und Winkelabhängigkeit der Emissionen lassen sich mit relativistischer Kinematik erklären. Somit erlauben diese Experimente einen neuen und sehr direkten Blick auf die relativistische Dynamik in laserproduzierten Plasmen. Diese Arbeiten wurden gemeinsam mit Paul Gibbon in Physical Review Letters veröffentlicht [5].

Für diese Experimente haben wir gemeinsam mit der Physikalisch-Technischen Bundesanstalt ein kompaktes Elektronen- und Röntgenspektrometer entwickelt, das es erlaubt, simultan das

Elektronenspektrum und das Röntgenspektrum zwischen etwa 20 keV und etwa 3 MeV zu vermessen. Das Spektrometer besteht aus einer Vielzahl von Thermolumineszenzdetektoren, eingepackt zwischen Absorbern verschiedener Dichte. Es erlaubt eine Messung der absolut einfallenden Dosis mit einer spektralen Auflösung von etwa 10%. Mit diesem Gerät können also simultan die im Laserplasma primär beschleunigten schnellen Elektronen und die sekundär von diesen erzeugte Bremsstrahlung charakterisiert werden. Aufgrund ihrer zudem noch sehr geringen Ausmaße konnten bis zu 12 solcher Spektrometer gleichzeitig eingesetzt werden. Eine detaillierte Beschreibung und Charakterisierung dieser Spektrometer haben wir bei Review of Scientific Instruments zur Veröffentlichung eingereicht [10].

4 Kerne

Wie wir in Abschnitt 3.3 gesehen haben, entsteht durch die Wechselwirkung eines hochintensiven Laserpulses mit Materie ein sehr heißes Plasma, das Elektronen und Photonen mit Energien von bis zu vielen Megaelektronenvolt emittiert. In diesem Plasma und mit seinen hochenergetischen Emissionen lassen sich einfache Kernreaktionen wie Neutronenabspaltung, Kernfusion und Kernspaltung auslösen. Ich werde in diesem Kapitel drei Experimente zu diesen Kernreaktionen beschreiben, die alle mit dem Jenaer TW-Ti:Saphir-Laser durchgeführt wurden. Die Neutronenabspaltung und die Spaltung großer Kerne sind dabei überhaupt zum erstenmal mit einem so kleinen Laser gelungen.

4.1 Photoneutronen

Der Kern mit der niedrigsten Energieschwellen für photoinduzierte Neutronenabspaltung (γ, n) ist ^9Be . Ab einer Gammaenergie von $E = 1,67 \text{ MeV}$ kann Beryllium in ein Neutron und ^8Be spalten, welches sofort in zwei Alphateilchen zerfällt. Um diese Kernreaktion mit lasererzeugter Röntgenstrahlung nachzuweisen, haben wir ein Stück Beryllium in die Nähe eines Tantaltargets gestellt, das als Konverter in Bremsstrahlung dient. Die Berylliumprobe wurde in der Richtung montiert, in der die meiste harte Röntgenstrahlung emittiert wird (siehe Abschnitt 3.3). Die Tantalprobe wurde mit 20000 Laserschüssen einer Intensität von $5 \cdot 10^{18} \text{ W/cm}^2$ bestrahlt und es wurde die Zahl der insgesamt produzierten Neutronen gemessen.

In einem ersten erfolgreichen Experiment im Frühjahr 2000 wurden etwa 100 Photoneutronen pro Laserschuß produziert. Es ist nach unserer Kenntnis der erste experimentelle Nachweis einer (γ, n)-Reaktion mit einem Table-Top-Lasersystem. Die Einschränkung auf Table-Top-Laser muß allerdings gemacht werden, da bereits mit zwei wesentlich größeren Lasern am Rutherford Appleton Laboratory und am Lawrence Livermore National Laboratory (γ, n)-Reaktionen nachgewiesen wurden [14, 11]. Berücksichtigt man die um etwa 10000 geringere Wiederholrate dieser Lasersysteme, so ist die Neutronenproduktionsrate mit unserem kleinen Laser jedoch vergleichbar bis höher. Neben der grundsätzlichen Bedeutung dieses Experiments steht nun eine Neutronenquelle für zukünftige Anwendungen zur Verfügung, die außer ihrer Kompaktheit insbesondere die einzigartige Eigenschaft besitzt, extrem kurze Neutronenpulse zu produzieren. Die hochenergetische Bremsstrahlung erzeugenden heißen Elektronen werden nur während der Dauer des Laserpulses von ungefähr 100 fs beschleunigt. Berücksichtigt man noch Laufzeiten der Elektronen und der Bremsstrahlung bis zum Beryllium, so wird die Neutronenemissionsdauer in der Größenordnung weniger Pikosekunden liegen. Wegen der breiten Energieverteilung der spaltenden Gammastrahlung ist allerdings auch die Energieverteilung der Photoneutronen breit. Ob diese Eigenschaften eine Anwendung laserproduzierter Photoneutronen in der Neu-

tronenspektroskopie oder gar der zeitaufgelösten Spektroskopie eröffnen, ist wohl im Moment nicht zu übersehen.

Gleichzeitig mit diesem Photoneutronenexperiment wurde eine weitere laserinduzierte Kernreaktion realisiert, nämlich die Verwandlung von Gold in Quecksilber durch Neutroneneinfang. ^{197}Au besitzt einen hohen Einfangsquerschnitt für thermische Neutronen von etwa 100 barn. Das dadurch erzeugte ^{198}Au zerfällt mit einer Halbwertszeit von 2,7 Tagen durch einen γ -assistierten β^- -Zerfall in ^{198}Hg . Um diese Reaktion nachzuweisen, war die Berylliumprobe, in der Photoneutronen generiert wurden, auf eine Plastikkugel montiert, in deren Zentrum ein Stück Gold positioniert wurde. Im Plastikvolumen wurden die Photoneutronen moderiert, so daß sie mit hoher Wahrscheinlichkeit von der Goldprobe eingefangen werden konnten. Nach der Bestrahlung der Tantalprobe mit 20000 Laserschüssen wurde die Goldprobe vor einen extrem untergrundarmen Germaniumdetektor in der Physikalisch-Technischen Bundesanstalt gestellt, der die beim β -Zerfall des ^{198}Au emittierte γ -Strahlung der Energie 412 keV aufzeichnete. Die bestrahlte Goldprobe emittierte etwa dreimal so viel γ -Strahlung wie eine Referenzprobe, die durch ständige Hintergrundsneutronen aktiviert war.

Die quantitative Auswertung der Goldtransmutationsreaktion erlaubt eine Abschätzung der Anzahl der lasererzeugten Röntgenstrahlung mit Photonenergien über 1,67 MeV, der Quelle für die Photoneutron-Reaktion in Beryllium. Der erhaltene Wert stimmt innerhalb der Unsicherheit der Auswertung mit dem Wert, den Thermolumineszenzspektrometer ergaben, überein. Kernreaktionen mit bekannten Energieschwellen können somit zur Charakterisierung harter lasererzeugter Röntgenstrahlung eingesetzt werden. Dies ist insbesondere bei noch höheren Energien von vielen MeV sehr nützlich, da hier keine anderen Detektoren mehr existieren.

Details der Messungen sind in [5, 6] beschrieben.

4.2 Deuteriumfusion

Beschießt man mit der höchstmöglichen Laserintensität eine Deuteriumprobe, so werden dabei Deuteriumatome auf Energien von mehreren hundert Kiloelektronenvolt geheizt. Der Wirkungsquerschnitt für Deuteriumfusion, $d(d,n)^3\text{He}$, ist bei Stößen mit einer Relativenergie von 200 keV bereits etwa 50 mbarn. Mit einem deuterierten Target sollten also Fusionsreaktionen nachweisbar sein. Dies wurde vor unseren Messungen bereits durch Laserbeschuß von deuteriertem Plastik CD_2 und von Deuteriumclustern gezeigt [15, 12], wobei Ausbeuten von $10^4 - 10^5$ Neutronen pro Laser erreicht wurden.

Wir haben die im EUV-Projekt (Abschnitt 3.2) entwickelte Quelle kleiner Tröpfchen mit schwerem Wasser (D_2O) gefüllt und diese Tröpfchen mit den Laserpulsen aus dem Jenaer TW-Laser beschossen. In einer Zusammenarbeit mit dem Max-Planck-Institut für Quantenoptik in Garching wurde eine Neutronenflugzeitdetektion aufgebaut, mit der die Fusionsneutronen, die aus

der Fusion eine Energie von 2,45 MeV mitbringen, nachgewiesen werden können. Zusätzlich haben wir einen Fänger aus deuteriertem Plastik in die Nähe des Laserfokus gestellt, in dem aus dem Tröpfchen geschleuderte Deuteriumatome weitere Fusionsreaktionen auslösen können.

Das Experiment hat im wesentlichen zwei Resultate: Erstens konnten bis zu 10^5 Fusionsreaktionen pro Laserschuß ausgelöst, also aufgrund der Wiederholrate des Lasers 10^6 Neutronen pro Sekunde erzeugt werden. Zweitens zeigen die Flugzeitspektren mit eingebautem Fänger zwei Neutronensignale zu unterschiedlichen Flugzeiten. Das frühere Signal wird von Neutronen erzeugt, die im Wasserströpfchen entstanden sind, das spätere von Neutronen aus dem Fänger. Diese erreichen den Detektor um die Ionenflugzeit zwischen Tröpfchen und Fänger verzögert. Aus deren Abstand und Breite können die Energie und die Energieverteilung der fusionierenden Deuteriumatome bestimmt werden. Mit dem bekannten Fusionswirkungsquerschnitt kann daraus die Temperatur der im Tröpfchen beschleunigten Ionen berechnet werden. Sie betrug in diesen Experimenten etwa 100 keV. Durch Variation der Fängerposition relativ zur Lasereinfallsrichtung kann auch die Winkelverteilung der Ionenemission detektiert werden. Neben dem für laserproduzierte Neutronen außerordentlich hohen Neutronenfluß erlaubt dieses Experiment also auch eine detaillierte Diagnostik der Wechselwirkung intensiver Laserpulse mit Materie. Die letzten Messungen wurden erst im April 2002 durchgeführt. Sie werden zur Zeit sorgfältig ausgewertet und dann veröffentlicht.

Zum Schluß noch eine kleine Bemerkung: würden alle Deuteriumpaare des Tröpfchens fusionieren, so würde eine Energie von 50 Joule frei. Natürlich ist hier aber das Lawson-Kriterium für selbsttragenden vollständigen Abbrand nicht erfüllt und zwar um einen Faktor 10000. Es besteht also keine Gefahr und auch keine Hoffnung, mit diesem Aufbau Energie gewinnen zu können.

4.3 Spaltung schwerer Kerne

Seit den ersten Gedanken an laserinduzierte Kernreaktionen geistert die Idee durch den Raum, ob nicht mit Hilfe eines kleinen, einfach zu bedienenden und vergleichsweise preiswerten Lasers langlebige radioaktive Kerne in kurzlebige oder gar stabile umgewandelt werden können. Nicht um morgen der Welt den radioaktiven Abfall aus der Kernenergiegewinnung zu entsorgen, sondern zunächst aus Spaß an einem für Laser-, Molekül- oder Plasmaphysiker exotischen Experiment und besonders auch als Diagnostik der hochenergetischen Plasmaemissionen wie Elektronen und Photonen.

Für typische Spaltprodukte aus der Kernenergiegewinnung mit Massenzahlen um $A \simeq 100$ kommen (γ, n) - und (γ, xn) -Reaktionen mit lasererzeugter γ -Strahlung in Frage, für spaltbare Kerne mit Massenzahlen über $A \simeq 230$ ebenfalls (γ, n) -Reaktionen und zusätzliche direkte Photospaltung (γ, f) . Die Wirkungsquerschnitte für Photospaltung haben typischerweise eine Energie-

schwelle oberhalb von 6 MeV und ein Maximum bei der Riesenresonanz der Kerne um 15 MeV. Die Energieschwellen für (γ, n) -Reaktionen der Spaltprodukte liegen meist ebenfalls zwischen 5 MeV und 10 MeV, für (γ, xn) -Prozesse sind sie sehr viel höher. Die radioaktiven Proben für diese Experimente erhalten wir aus dem Institut für Transurane der Europäischen Kommission in Karlsruhe, das sich mit der Lagerung, Trennung und Umwandlung radioaktiver Abfallstoffe beschäftigt.

Wir haben im März 2002 folgendes erstes Experiment durchgeführt: Laserpulse aus dem Jenaer TW-Ti:Saphirlaser wurden mit einer Intensität von über $8 \times 10^{19} \text{ W/cm}^2$ auf ein Tantalblech fokussiert. In dem dabei entstehenden Plasma werden Elektronen auf relativistische Energien in das Tantalblech hineinbeschleunigt und erzeugen dort Bremsstrahlung. Hinter diesem Bremsstrahlungskonverter wurden 10 g metallisches, abgereichertes Uran montiert. In einem zweiten Experiment wurden 10 g Thoriumoxid bestrahlt. Nach jeweils etwa 10000 Laserschüssen wurden Gammaspektren der Uran- und Thoriumprobe aufgenommen. Zwischen den intensiven Linien der selbst stark strahlenden Uran- und Thoriumprobe konnten kleine Signale beobachtet werden, die über ihre Energie und ihre Lebensdauer kurzebigen Spaltprodukten zugeordnet werden konnten. Es konnten Spaltprodukte wie ^{87}Kr , ^{92}Sr , ^{128}Sb , ^{134}I und noch einige mehr identifiziert werden. Aus der Intensität der γ -Linien ergab sich die Anzahl der pro Laserschuß gespaltenen Kerne zu etwa 1000. Mit den bekannten Photospaltungsquerschnitten kann daraus berechnet werden, daß pro Laserschuß etwa 10^6 Photonen mit Energien über 6 MeV erzeugt wurden. Durch den quantitativen Nachweis von Kernreaktionen mit verschiedenen Energieschwellen wird es möglich sein, das Bremsstrahlungsspektrum bei Energien über vielen MeV zu charakterisieren. Daraus kann man auf die Temperatur der heißen Elektronen rückschließen und somit die Vorhersagen der Mechanismen zur Elektronenbeschleunigung in relativistischen Laserplasmen überprüfen. Die in Abschnitt 3.3 beschriebenen Thermolumineszenzspektrometer können nur Elektronen- und Photonentemperaturen unter etwa 2 MeV detektieren. Sie sind also nur für Experimente mit Laserintensitäten unterhalb von etwa $5 \cdot 10^{18} \text{ W/cm}^2$ geeignet. Darüber sind Kernreaktionen, wie die hier beschriebenen die einzige Möglichkeit, Spektren und Temperaturen zu vermessen.

Eine gemeinsame Veröffentlichung dieser Messungen mit dem Institut für Transurane ist in Arbeit. In den folgenden Messungen werden wir versuchen, laserinduzierte Photospaltung anderer schwerer Kerne und (γ, n) - und (γ, xn) -Reaktionen an radioaktiven mittelschweren Kernen nachzuweisen.

5 Laser

In den Jahren meiner Arbeit in Jena wurde unter meiner Leitung aus einem 2 Terawatt Titan:Saphir Femtosekundenlaser ein sehr gut charakterisiertes 15 Terawatt-Lasersystem, mit dem sich mit einer Wiederholrate von 10 Hz fokussierte Lichtintensitäten von bis zu 10^{20} W/cm² erzeugen lassen. Dabei blieb die Anlage kompakt und überschaubar und lässt sich von einer qualifizierten Person bedienen. Table-Top-Lasersysteme der Klasse um 10 TW gibt es zur Zeit weltweit ungefähr zehn. Experimentiert wird jedoch nur mit wenigen dieser Laser.

5.1 Das Jenaer 15 Terawatt-Lasersystem

Das Jenaer Lasersystem besteht aus vier wesentlichen Komponenten: einem modengekoppelten Femtosekundenlaser, einem Strecker, einer dreistufigen Versäkereinheit und einem Kompressor in Vakuum.

Der Kerrlinsen-modengekoppelte Ti:Saphir-Laser erzeugt Pulse einer Dauer von 45 fs und einer kleinen Energie von etwa 5 nJ. Diese Pulse sollen nun um einen Faktor 10^9 verstärkt werden. Da in modengekoppelten Oszillatoren der kurze Laserpuls immer im Resonator umläuft, ist die Wiederholrate des Lasers groß, in unserem Fall etwa 80 MHz. Da man nicht alle Pulse verstärken kann, werden zunächst zehn Pulse pro Sekunde aus dem Pulszug isoliert. Um während der Verstärkung nichtlineare Prozesse unter Kontrolle zu halten und um Zerstörung der optischen Elemente zu vermeiden, werden in der zweiten Komponente die Pulse auf 150 ps gestreckt und damit die Intensität um einen Faktor 3000 reduziert. Dieser Strecker besteht im Grunde nur aus zwei Dispersionsgittern, einer Linse und einem Spiegel, die so angeordnet sind, daß dem breitbandigen Laserpuls eine lineare normale Dispersion aufgeprägt wird und er am Ende wieder ein gebündelter Strahl ist. Nun folgen drei Verstärkerstufen, jeweils mit einem Ti:Saphir-Kristall als Verstärkermedium. Der erste ist ein sogenannter regenerativer Verstärker, der selbst ein Laserresonator ist und dadurch die räumliche Mode des Laserpulses während der Verstärkung erhält. Die beiden folgenden Stufen sind einfache Verstärker mit vier bzw. drei Durchgängen durch den jeweiligen Titan:Saphir-Kristall. Zwischen jeder Stufe wird der Strahldurchmesser vergößert, um trotz der endlichen Sättigungsenergiedichte des Lasermaterials möglichst viel Energie extrahieren zu können. Im letzten Schritt werden die Laserpulse im sogenannten Kompressor, einem Dispersionsgitteraufbau mit anomaler linearer Dispersion, wieder auf nahezu ihre ursprüngliche Dauer verkürzt.

Schließlich ist ein Laserpuls mit einer Energie von 1 Joule und mit einer Pulsdauer von 70 Femtosekunden entstanden, also einer Länge in Ausbreitungsrichtung von nur 20 Mikrometern, und einem transversalen Durchmesser von 70 Millimetern. Die räumliche Mode des Strahls ist dabei so gut, daß er nahezu beugungsbegrenzt auf eine Fläche von weniger als 5 Quadratmikrometer

fokussiert werden kann. An diesem Punkt herrscht dann, für eine kurze Zeit, eine Lichtintensität von 10^{20} Watt pro Quadratzentimeter. Dies ist gerade soviel, als würde man alles auf die Erde fallende Sonnenlicht auf ein Zehntel eines Quadratmillimeters bündeln.

5.2 Diagnostik eines TW-Laserpulses

Es genügt im Grunde, die Pulsenegie, die Pulsdauer und die Fokusfläche des Laserpulses zu kennen, um seine Intensität im Brennpunkt zu bestimmen. Um jedoch sicher zu sein, daß im Brennpunkt tatsächlich eine Intensität von 10^{20} W/cm² herrscht und um zu vermeiden, daß bereits vor Auftreffen des Laserpulses durch Vorpulse ein Plasma erzeugt wird, müssen die Laserpulse in Raum und Zeit extrem ebenmäßig sein. Um dies zu erreichen und zu überprüfen, haben wir neben der Aufrüstung und Verbesserung des Lasers eine ausgefeilte Laserpulsdiagnostik aufgebaut.

Ein Autokorrelator dritter Ordnung vermisst die zeitliche Pulsform in einem Bereich von 500 ps um den Hauptpuls mit einer Dynamik von 6 Größenordnungen. Zweitens und ebenso notwendig wird die Ebenheit der Front des Laserpulses vermessen. Denn nur wenn die dünne Lichtscheibe eben ist und senkrecht zur Ausbreitungsrichtung steht, ist der gesamte Laserpuls im Brennpunkt auch kurz. Dazu wurde in einer Diplomarbeit ein geeignetes Interferometer aufgebaut, das Pulsfrontverkippungen mit einer Genauigkeit von 0,01° zu messen erlaubt. Weiterhin kann die Energie des Laserpulses an der Stelle der Probe vermessen werden, indem die Probe durch eine 50 μm große Lochblende ersetzt wird und die transmittierte Energie bei einem Schuß mit voller Leistung gemessen wird. Zudem haben wir in einer weiteren Diplomarbeit eine Vorplasmadiagnostik am Target selbst aufgebaut, die auf einem Interferometer basiert. Damit wird die zeitliche Vorgeschichte des Hauptlaserpulses innerhalb der 4 ns vor seinem Erscheinen diagnostiziert. Schließlich wird der Anteil an spontaner verstärkter Emission aus der Plasmabeobachtung und aus Pulsdauer- und Energiemessungen auf kleiner als 5% abgeschätzt.

Der vielleicht wichtigste Fortschritt auf dem langen Weg zu 10^{20} W/cm² war die Verkleinerung der tatsächlichen Fokusfläche auf einen nahezu beugungsbegrenzten Wert von unter 5 μm². Wir haben dies einerseits durch Reinigen der Strahlmode erreicht und andererseits durch den Einbau einer ständigen Fokusbeobachtung an der Stelle des Experiments und durch sehr sorgfältiges Fokussieren des Laserstrahls mit einem parabolischen Spiegel.

Zwischen die ersten beiden Verstärkerstufen haben wir eine Vorpulseinheit eingebaut, die es erlaubt, in Energie und zeitlichem Abstand zum Hauptlaserpuls definierte Vorpulse zu erzeugen. Durch ein automatisiertes Strahlnachführungssystem wird dafür gesorgt, daß ganz am Ende des Weges nach 20 m, im Fokus des Laserstrahls, Haupt- und Vorpuls unabhängig von ihrem zeitlichen Abstand stets genau übereinander liegen. Eine Beschreibung dieser Vorpulseinheit haben wir in Review of Scientific Instruments veröffentlicht [4].

Mit all dieser Routinediagnostik kann der Laserpuls nahezu vollständig charakterisiert werden. Das Lasersystem ist von einer anfälligen, stets weiterzuentwickelnden und zu reparierenden Experimentieranordnung zu einem sehr zuverlässigen Arbeitspferd geworden. Es kann mit voller Leistung und voller Wiederholrate betrieben werden und der Laser kann, und das halte ich für sehr wichtig für den möglichst täglichen Betrieb, von einer einzelnen geübten Person bedient werden.

6 Zukunft

In der Zeit seit meiner Promotion habe ich mich in zwei verschiedenen Instituten mit zwei zunächst nicht verbunden erscheinenden Themen beschäftigt: in Würzburg mit zeitaufgelöster Molekülspektroskopie und fundamentalen Experimenten zu kohärenter Kontrolle mit Femtosekundenlaserpulsen und in Jena mit der Wechselwirkung höchstintensiver Laserpulse mit Materie und der Erzeugung und Anwendung dabei entstehender Röntgenstrahlung. Ich will in diesem letzten Abschnitt versuchen, die Zukunft der beschriebenen Experimente zu prognostizieren und wir werden dabei sehen, wie interessante Fragestellungen und Methoden aus beiden Bereichen aufeinander angewiesen sein werden.

Zeitaufgelöste Molekülspektroskopie

Intramolekulare Dynamik wird heute nahezu ausschließlich im sichtbaren und infraroten Spektralbereich untersucht. Dabei koppeln ultrakurze Laserpulse an Elektronen in äußeren Schalen und erzeugen dadurch Schwingungs- und Rotationswellenpakete im Molekül. Die Kontrolle über die Moleküldynamik und ihre Beobachtung werden durch zeitverzögerte elektronische Anregungen erreicht. Damit können Energietransportprozesse studiert werden. Um aus den elektronischen Eigenschaften auf die innere Dynamik des Moleküls, also die Bewegung der Atome zu schließen, ist allerdings in der Regel die Kenntnis des intramolekularen Potentials notwendig, was nur für einige kleine Moleküle und insbesondere nur selten für elektronisch angeregte Zustände der Fall ist. Man versucht zur Zeit, dieses Dilemma durch den Einsatz selbst lernender und optimierender Anregungen zu umgehen, die ohne diese Kenntnis, und meist auch ohne die Kenntnis zu liefern, Moleküle in vorgewählte Reaktionspfade lenken. Letztlich ist diese Art der blinden kohärenten Kontrolle, so modern und experimentell trickreich sie auch sein mag, eher unbefriedigend.

Einen direkten Blick auf die Dynamik komplexer Moleküle könnte in Zukunft die Verwendung ultrakurzer Röntgenpulse in Pump-Probe-Experimenten liefern. Statt die elektronischen Wellenfunktionen zu proben, wird damit direkt die Struktur und die Bewegung der Atome abgefragt. In ersten Experimenten ist es gelungen, phononische Anregungen und Schmelzprozesse in Halbleiterkristallen zu beobachten, indem nach Anregung mit einem sichtbaren Laserpuls die Intensitäts- und Winkeländerung eines Braggreflexes eines ultrakurzen Röntgenpulses aufgenommen wird. Die zeitliche Auflösung dieser Experimente ist durch die Pulsdauer der verwendeten K_{α} -Strahlung von unter 500 fs gegeben. Um diese Methode auf Systeme mit vielen Freiheitsgraden anzuwenden, sollte man nun versuchen, Laue-Spektroskopie zu betreiben. Erste zeitaufgelöste Laue-Messungen an Myoglobin mit 150 ps langen Synchrotronpulsen sind bereits erfolgreich. Ersetzt man die Synchrotron-Röntgenquelle durch eine laserproduzierte K_{α} -Quelle, wie sie in Kapitel 3 beschrieben ist, so ist diese nicht nur kleiner und billiger, sondern die potentielle Zeitauflösung steigt um fast drei Größenordnungen. Dies ist meines Erachtens ein sehr lohnenswertes Vorhaben.

Lasertechnologie

Für die oben und unten genannten Anwendungen ist die Weiterentwicklung der derzeitigen Laserquellen wichtig. Basierend auf den heute schon kommerziellen Ultrakurzpulslasern werden auch die Hochintensitätslaser in den nächsten Jahren durch Einsatz neuer Technologien einerseits kompakter und andererseits stärker werden: Alle oder zumindest einige der heutigen regenerativen und Multipass-Verstärkerstufen werden ersetzt werden durch optisch parametrische Verstärker. Diese erreichen eine sehr viel höhere Verstärkung bei einem gleichzeitig wesentlich besseren Vorpulskontrast. Außerdem wird sich dabei die Anzahl der notwendigen Pumplaser verringern, was die Kosten und die Komplexität des Lasersystems erheblich reduziert. Abschätzungen und erste Versuche zeigen, daß mit einem einzigen Pumplaser, einer parametrischen und einer konventionellen Pumpstufe Energien und Leistungen knapp unter denen des derzeitigen Jenaer Lasersystem erreichbar sein sollten.

Um die Pulsesnergie und die Intensität wesentlich höher zu treiben, müssen wohl in den letzten Verstärkerstufen wie schon seit 20 Jahren dotierte Gläser als Verstärkermaterial verwendet werden. Es werden allerdings in Zukunft Diodenlaser statt der bisher verwendeten Blitzlampen als Pumpquellen eingesetzt werden können. Dies reduziert die Kosten und erhöht die Stabilität und die Effizienz des Systems. Die Verstärkungsbandbreite der Gläser wird auch ultrakurze Pulse unterstützen.

In 10 Jahren wird es vermutlich turn-key-Lasersysteme mit den Leistungen des heutigen Jenaer Systems geben. Die experimentellen Lasersysteme werden entweder wesentlich höhere Repetitionsraten haben oder Pulsesnergien um 1 Kilojoule. Mit diesen Lasersystemen werden die lasergetriebenen Röntgenquellen intensiver werden, die Röntgenflüsse und die maximalen Röntgenphotonenenergien werden steigen.

Intensive Röntgenlinienstrahlung

Die Laserplasma-Röntgenquellen, wie ich sie in Kapitel 3 beschrieben habe, besitzen einige sehr nützliche Eigenschaften: die Zahl der Photonen ist groß, die Pulsdauer ist sehr kurz, die Ausdehnung der Quelle ist klein und mindestens die K_{α} -Strahlung ist auch noch monochromatisch. Zur optimalen Brillanz fehlt also nur noch die Bündelung. Tatsächlich ist die Leuchtstärke der K_{α} -Quelle, also die Zahl der Photonen pro Zeit und emittierende Fläche und Bandbreite, größer als die, die in zukünftigen Freien Elektronenlasern generiert werden kann. Röntgenlinienstrahlung aus (nichtrelativistischen) Atomen wird immer isotrop bleiben. Streut man jedoch einen starken Laserpuls an einem relativistischen Elektronenstrahl, so wird der Elektronenstrahl vom Lichtfeld wie in einem Undulator moduliert und strahlt gerichtet ab. Die Energie der Strahlung wird durch die Geometrie der Anordnung und die Elektronenenergie bestimmt und kann viele keV betragen, also genau die Photonenergie, die für Röntgenbeugung gewünscht ist. Die Pulsdauer bleibt dabei kurz, da der Elektronenstrahl nur während der Wechselwirkung mit dem ultrakurzen Laserpuls moduliert ist. Diese nichtlineare Thomsonstreuung könnte den Photonenuß in Röntgenbeugungsexperimenten erheblich steigern und außerdem den Einsatz komplizierter und ineffizienter Röntgenoptik vermeiden helfen.

Nichtlineare Röntgenoptik

Nichtlinear optische Prozesse erfordern in der Regel hohe Lichtintensitäten, weil die Suszeptibilitäten für höhere Ordnungen der Felder bzw. die Wirkungsquerschnitte für Mehrphotonenprozesse klein sind. Im sichtbaren Spektralbereich ist die Beobachtung, Charakterisierung und insbesondere die Anwendung nichtlinearer Prozesse bis in hohe Ordnungen durch die Existenz von starken Lasern einfach. Im Röntgenspektralbereich jedoch ist bislang noch kein einziger echter Mehrphotonenprozess gemessen worden, da keine geeignete Lichtquelle existiert. Laserproduzierte K_{α} -Quellen, wie ich sie in Kapitel 3 beschrieben habe, könnten in naher Zukunft intensiv genug sein, um einfache nichtlineare Prozesse mit Photonen mit Energien einiger keV zu induzieren. Zum Beispiel folgt aus dem Wirkungsquerschnitt für Zweiphotonen-K-Schalen-Ionisation mittels schwerer Kerne und den K_{α} -Photonenmessungen in Abschnitt 3, daß die Röntgenintensität im Laserfokus ausreicht, um 1000 Zweiphotonenereignisse pro Laserschuß zu produzieren. Leider kann man diese nicht von den viel häufigeren linearen Ionisationen durch Photonen oder Elektronenstöße unterscheiden. Mit einer nicht allzu großen Steigerung der Röntgenintensität sollte sich bald ein sauberes Experiment zur nichtlinearen Röntgenoptik durchführen lassen. Die erste Anwendung wird die Messung der Pulsdauer der ultrakurzen Röntgenpulse selbst sein, die bisher nur aus indirekten Messungen abgeschätzt werden kann. Die zweite ist die experimentelle Bestimmung der nichtlinearen Suszeptibilitäten im Röntgenspektralbereich. Anwendungen zum Beispiel zur Frequenzkonversion würden wie auch im sichtbaren Spektralbereich der Spektroskopie viele Möglichkeiten schaffen.

Laserinduzierte Kernphysik

Die im Kapitel 4 beschriebenen Experimente zu laserinduzierten Kernreaktionen wie Fusion kleiner oder Spaltung großer Kerne sind zunächst aus Neugier auf ein für Laser- oder Atomphysiker ungewohntes Thema entstanden. Daß die ersten Experimente erfolgreich waren, ist sehr erfreulich. Bei der Photoneutronenerzeugung und der Kernspaltung sind sie auch erstmalig Table-top-Laser gelungen. Bislang beschränken sich die beobachteten Reaktionen auf altbekannte Kernphysik. Dies wird sich erst ändern, wenn aufgrund der kurzen Dauer und damit hohen Intensität der Elektronen- und Photonensequenzen nichtlineare Kernanregungen induziert werden können.

Hingegen sind Anwendungen dieser Methoden in der Isotopenproduktion und -transmutation durch Neutroneneinfang, Protonenstoß oder Photo- und Elektronenspaltung denkbar. Basierend auf den Neutronenausbeuten der in Kapitel 4 beschriebenen Experimente haben wir eine detaillierte Abschätzung der erzeugbaren Aktivität eines kurzlebigen β^- aktiven Iodisotops durchgeführt (^{128}I). Unter optimalen Moderierungsbedingungen sollte mit einer Neutronenquelle wie der unseren eine Anfangsaktivität von vielen hundert Kilobecquerel erzeugt werden können. Dies ist nahe an einem für radiologische Zwecke notwendigen Wert. Der technische Vorteil einer solchen Anlage könnte ihre im Vergleich zu einem Neutronenreaktor geringe Größe sein, die insbesondere lokale Produktion kurzlebiger Isotope erlauben würde.

Eine weitere mögliche Anwendung ist die Transmutation langlebiger radioaktiver Isotope aus

der Kernenergiegewinnung. Diese können entweder durch thermische Neutronen oder durch Photospaltung oder durch Spaltung mit schnellen Neutronen in kurzlebige oder gar stabile Isotope umgewandelt werden. Für einige Isotope ist die Transmutation durch thermische Neutronen allerdings unpraktisch, da aufgrund der Neutroneneinfangquerschnitte des Isotops und seiner benachbarten Isotope eine größere Menge mehr des zu transmutierenden Isotops gebildet als vernichtet wird oder neue, schwere, ebenfalls radiotoxische Isotope erzeugt werden. In diesen Fällen ist eine Umwandlung durch Photospaltung oder (γ, xn) -Prozesse möglich. Es hat sich herausgestellt, daß diese Prozesse mit kleinen Laseranlagen ausgelöst werden können. Nun wird man zeigen müssen, welche Ausbeuten diese Prozesse erreichen können, um letztlich zu einer Aussage über die totale Effizienz lasergetriebener Kernspaltung zu gelangen. Dann erst kann man entscheiden, ob es ein realisierbares Lasersystem geben kann, das in einem sinnvollen Zeitrahmen von einigen zehn Jahren nuklearen Abfall in kurzlebige oder gar stabile Kerne umwandeln kann. Bis dahin wäre es aber noch ein weiter Weg.

Die experimentelle Physik in ultrakurzen und ultraintensiven Feldern wird in den kommenden Jahren spannend und interessant bleiben. Es werden grundlegende Fragen zur relativistischen Plasmaphysik bei den heute erreichbaren und vielleicht noch höheren Laserintensitäten bearbeitet werden. Es werden sich Bezüge zu hochenergetischen astrophysikalischen Problemen auftun und nichtlineare Prozesse mit Röntgenstrahlung werden möglich sein. Die von relativistischen Laserplasmen emittierten Photonen, Elektronen, Neutronen und Ionen werden wegen ihrer drei charakteristischen Eigenschaften, der Kürze, des hohen Flusses und des kleinen Quellvolumens, in vielen Gebieten Anwendungen finden. Gewiß wird dies in der zeitaufgelösten Spektroskopie der Fall sein, und zwar zunächst mit mittelharter Röntgenstrahlung, später vielleicht aber auch mit Teilchenstrahlen. Ob sich wegen einzigartiger Eigenschaften spezielle Anwendungen in der Isotopenproduktion entwickeln werden, muß sich noch zeigen. Im Bereich der intensiven weichen und mittelharten Röntgenstrahlung erwächst den laserproduzierten Plasmaemissionen die Konkurrenz des Freien Elektronenlasers. Die besonderen Stärken der Laserplasmen im Vergleich zu Freien Elektronenlasern oder Synchrotrons werden aber auf absehbare Zeit die Kürze und die wirklich hohen Photonenergien bleiben, und auch der vergleichsweise geringe Aufwand, sie zu erzeugen.

Literaturverzeichnis

- [1] Heinrich Schwoerer, Roman Pausch, Mario Heid, Volker Engel, Wolfgang Kiefer;
„Femtosecond time-resolved two-photon ionization spectroscopy of K₂“,
J. Chem. Phys. **107**, 9749-9754 (1997).
- [2] Heinrich Schwoerer, Roman Pausch, Mario Heid, Wolfgang Kiefer;
„Femtosecond vibrational wavepacket spectroscopy in the electronic ground state of K₂“,
Chem. Phys. Lett. **285**, 240-245 (1998).
- [3] Roman Pausch, Mario Heid, Tao Chen, Wolfgang Kiefer, Heinrich Schwoerer;
„Selective generation and control of excited vibrational wavepackets in the electronic ground state of K₂“,
J. Chem. Phys. **110**, 9560-9567 (1999).
- [4] Christian Ziener, Gregor Stobrawa, Heinrich Schwoerer, Ingo Uschmann, Roland Sauerbrey;
„A novel device for the generation of controlled prepulses in a Ti:Sapphire amplifier chain“,
Rev. Sci. Instr. **71**, 3313-3316 (2000).
- [5] Heinrich Schwoerer, Paul Gibbon, Stefan Düsterer, Rolf Behrens, Christian Ziener, Christian Reich, Roland Sauerbrey;
„MeV x-rays and photoneutrons from femtosecond laser produced plasmas“,
Phys. Rev. Lett. **86**, 2317-2320 (2001).
- [6] Stefan Düsterer, Heinrich Schwoerer, Rolf Behrens, Christian Ziener, Christian Reich, Paul Gibbon, Roland Sauerbrey;
„Hard x-rays and nuclear reactions from laser produced plasmas“,
Contrib. Plasma Phys. **41**, 171-174 (2001).
- [7] Christian Ziener, Ingo Uschmann, Heinrich Schwoerer, Christian Reich, Paul Gibbon, Thomas Feurer, Andreas Morak, Stefan Düsterer, Gregor Stobrawa, Eckard Förster, Roland Sauerbrey;
„Optimization of K_α bursts for photon energies between 1.7 and 7 keV produced by fs-laser produced plasmas of different scale-length“,
Phys. Rev. E **65**, 066411 (2002).
- [8] Stefan Düsterer, Heinrich Schwoerer, Wolfgang Ziegler, Christian Ziener, Roland Sauerbrey;
„Optimization of EUV radiation yield from laser produced-plasma“,
Appl. Phys. B. **73**, 693-698 (2001).

- [9] Friederike Ewald, Heinrich Schwoerer, Roland Sauerbrey;
„K_α radiation from relativistic laser-produced plasmas“,
Europhys. Lett. bf 60 710-716 (2002).
- [10] Rolf Behrens, Heinrich Schwoerer, Stefan Düsterer, Peter Ambrosi, Georg Pretzler, Stefan Karsch, Roland Sauerbrey;
„A TLD based few-channel spectrometer for simultaneous detection of electrons and photons from relativistic laser-produced plasmas“,
zur Veröffentlichung angenommen von Rev. Sci. Instr., Februar 2003.
- [11] T. E. Cowan *et al.*;
„Photonuclear Fission from High Energy Electrons from Ultraintense Laser-Solid Interactions“,
Phys. Rev. Lett. **84**, 903-906 (2000).
- [12] T. Ditmire, J. Zweiback, V.P. Yanovsky, T.E. and Cowan, G. Hays, K.B. Wharton;
„Nuclear fusion in gases of deuterium clusters heated with a femtosecond laser“,
Phys. Plasmas **7**, 1993-1998 (2000).
- [13] D.C. Eder, G. Pretzler, E. Fill, K. Eidmann, A. Saemann;
„Spatial characteristics of K_α radiation from weakly relativistic laser plasmas“,
Appl. Phys. B **70**, 211-217 (1999).
- [14] K.W.D. Ledingham *et al.*; „Photonuclear Physics when a Multiterawatt Laser Pulse Interacts with Solid Targets“,
Phys. Rev. Lett. **84**, 899-902 (2000).
- [15] G. Pretzler, A. Saemann, A. Pukhov, D. Rudolph, T. Schätz, U. Schramm, P. Thirolf, D. Habs, K. Eidmann, G.D. Tsakiris, J. Meyer-ter-Vehn, K. Witte;
„Neutron production by 200 mJ ultrashort laser pulses“,
Phys. Rev. E **58**, 1165-1168 (1998).
- [16] C. Reich, P. Gibbon, I. Uschmann, E. Förster;
„Yield optimization and time structure of femtosecond laser plasma K_α sources“,
Phys. Rev. Lett. **84**, 4846-4849 (2000).
- [17] D.J. Tannor, S.A. Rice;
„Control of selectivity of chemical reaction via control of wave packet evolution“,
J. Chem. Phys. **83**, 5013 (1985).

7 Veröffentlichungen

7.1 Moleküldynamik und kohärente Kontrolle

[1]: S. 26

Heinrich Schwoerer, Roman Pausch, Mario Heid, Volker Engel, Wolfgang Kiefer;
„Femtosecond time-resolved two-photon ionization spectroscopy of K₂“,
J. Chem. Phys. **107**, 9749-9754 (1997).

[2]: S. 32

Heinrich Schwoerer, Roman Pausch, Mario Heid, Wolfgang Kiefer;
„Femtosecond vibrational wavepacket spectroscopy in the electronic ground state of K₂“,
Chem. Phys. Lett. **285**, 240-245 (1998).

[3]: S. 38

Roman Pausch, Mario Heid, Tao Chen, Wolfgang Kiefer, Heinrich Schwoerer;
„Selective generation and control of excited vibrational wavepackets in the electronic ground
state of K₂“,
J. Chem. Phys. **110**, 9560-9567 (1999).

Femtosecond time-resolved two-photon ionization spectroscopy of K₂

H. Schwoerer, R. Pausch, M. Heid, V. Engel, and W. Kiefer

*Institut für Physikalische Chemie der Universität Würzburg, Am Hubland, D-97074 Würzburg,
Federal Republic of Germany*

(Received 11 August 1997; accepted 12 September 1997)

We investigated the coherent motion of vibrational wave packets in the $|B\rangle ^1\Pi_u$ state of the potassium dimer applying two color pump/probe spectroscopy with a sub 100 fs time resolution. Special interest was paid to the ionization probe step which was analyzed carefully by varying the probe energy over a wide range. Time-dependent quantum calculations explain the experimental outcomes by introducing a nonconstant transition dipole moment between the $|B\rangle$ and the ionic state $|X^+\rangle$ and by taking into account the excitation of long lived autoionizing Rydberg states. © 1997 American Institute of Physics. [S0021-9606(97)02647-0]

I. INTRODUCTION

Femtosecond time-resolved photoionization spectroscopy has become a widely applied experimental method to study coherent vibrations, rotations, and reaction dynamics of electronically excited molecules and clusters.

The method evolved from femtosecond time-resolved spectroscopy of chemical reactions pioneered by Zewail and co-workers.^{1–3} The key idea of the method is as follows: a first ultrashort laser pulse, the pump pulse, excites a coherent superposition of molecular eigenstates. This wave packet subsequently evolves in time until a second laser pulse, the probe pulse, perturbs its evolution by excitation into a final, for example, ionic state. In the latter case the number of ions measured as a function of the time between pump and probe process reflects the dynamics of the wave packet in the intermediate state if the probing step is sensitive to the location of the wave packet on the potential energy surface.^{1,4}

The probing pathway does not necessarily have to be ionization but can also be excitation to a fluorescence state or to a dissociative state. In these cases the fluorescence yield or the number of dissociation products is measured as a function of the delay time between pump and probe pulses.^{3,5} Recently the use of femtosecond time-resolved coherent anti-stokes Raman spectroscopy (CARS) to detect ground and excited state vibrational motion in a single experiment was demonstrated in our laboratory.⁷ The advantage of photoionization in comparison to these techniques is the additional possibility to discriminate easily between different ions by utilizing their different charge to mass ratio e/m . This is essential if molecular systems like clusters or complexes are investigated which have to be prepared in supersonic jet expansions. Even if several species are ionized by the laser pulses, a quadrupole or time of flight mass spectrometer can select the desired system.

Two-fold information can be extracted in principle from the transient signals: in the time domain the coherent motion of the wave packet appears as a superposition of harmonic signals with frequencies given by the energy spacings of the participating levels. Phase relaxation processes can be seen as a loss of coherence, and energy relaxation or transport can be identified if different modes are coupled. In the spectral

domain, obtained by Fourier transformation of the time domain signal, the primary results are the energy differences of the contributing levels. In vibrational wave packet spectroscopy these give the vibrational constants of the molecular system and therefore the potential energy surface,^{8,9} in rotational coherence spectroscopy they include the rotational constants or tensor components which in particular give information about the geometry of the molecular system.^{10,11} By a combination of the two coordinates in a spectrogram plotting intensity versus time and frequency energy exchange processes can be nicely demonstrated.^{12,13}

In particular, in a large variety of homonuclear and heteronuclear diatomic systems, vibrational wave packets along the internuclear bond were investigated. In Na₂ and K₂ vibrational dynamics in the $|A\rangle ^1\Sigma_g^+$ state could be pursued for several tens of ps including dephasing and rephasing of the signal due to the anharmonicity of the potential energy surface. Interference effects with the electronic ground state and with higher electronic states^{14,15} and spin orbit coupling effects with a closely lying $|b\rangle ^3\Pi_u$ state were observed in both molecules.¹⁶ Even isotope selective dynamics in ^{39,39}K and ^{39,41}K could be detected¹⁷ and an isotope separation scheme which rests on this selectivity was proposed.¹⁸ Quantum mechanical calculation to simulate the obtained transient ion signals was performed.^{19,20} Experiments on the wave packet dynamics in the $|C\rangle ^1\Pi_u$ state of Cs₂ were reported.²¹ The latter were analyzed recently with respect to the effect of thermal averaging.²² Long lived coherent signal showing distinct rephasing effects occurred in wave packets in the $|B\rangle$ state of molecular iodine, detected by ions as well as by zero kinetic energy electrons.²³ Fractional revivals, partial rephasing effects in strongly anharmonic potentials, were nicely demonstrated in Br₂.¹³ Also, in the heteronuclear NaK, vibrational wave packets could be observed.^{24,25}

In this contribution we describe experimental and theoretical investigations of vibrational wave packet dynamics in the $|B\rangle ^1\Pi_u^+$ state of the potassium dimer K₂. Figure 1 shows the potential energy as a function of the internuclear separation of the electronic ground state $|X\rangle ^1\Sigma_g^+$, the $|B\rangle ^1\Pi_u^+$ state,²⁶ and the ground state of the ion K₂ $|X^+\rangle ^2\Sigma_g^+$.²⁷ The vibrational constants in the $|B\rangle$ state are $\omega_e = 75 \text{ cm}^{-1}$ and $\omega_{ex_e} = 0.39 \text{ cm}^{-1}$ and the equilibrium

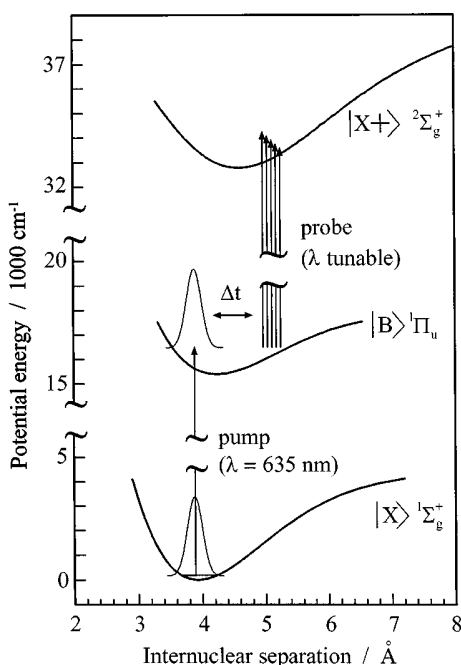


FIG. 1. Pump/probe scheme for femtosecond two-photon photoionization spectroscopy of the potassium dimer via the $|B\rangle^1\Pi_u$ state. At time $t=0$ the pump pulse creates a vibrational wave packet in the $|B\rangle$ state which evolves in time on the electronically excited potential energy surface. The motion of the wave packet is then monitored by applying a time delayed probe pulse that can be tuned in energy over a wide range, exciting the system to the ionic ground state $|X+\rangle$ of K₂.

nuclear separation in $|X\rangle$ is 3.924 Å, in $|B\rangle$ 4.236 Å.²⁶ The lower arrow represents the pump pulse exciting the vibrational ground state wave function of $|X\rangle$ to the vibrational manifold of $|B\rangle$. The five upper arrows indicate the probe process after a time delay of τ with different probing energies.

The paper is organized as follows: A short section (II) describes the experimental configuration. Section III presents the experimental observations of the wave packet dynamics in the $|B\rangle$ state of K₂ for different pump and probe wavelengths. In Sec. IV we will compare these with the theoretical predictions and develop possible explanations of the measured results.

II. EXPERIMENT

The experimental setup is composed of three major parts: the molecular beam apparatus, the two color femtosecond laser system, and the pump/probe and detection scheme (Fig. 2).

The molecular beam apparatus consists of two vacuum chambers, one for the potassium oven and one for spectroscopy and detection. The oven chamber is evacuated by a 5000 l/s diffusion pump to a pressure of approximately 10^{-4} mbar. The potassium cartridge is heated to 380 °C, its nozzle (diameter: 100 μm) to 450 °C to prevent plugging. A back pressure of 1–3 bar argon gas was applied to the cartridge. A skimmer with 1 mm opening separates the oven

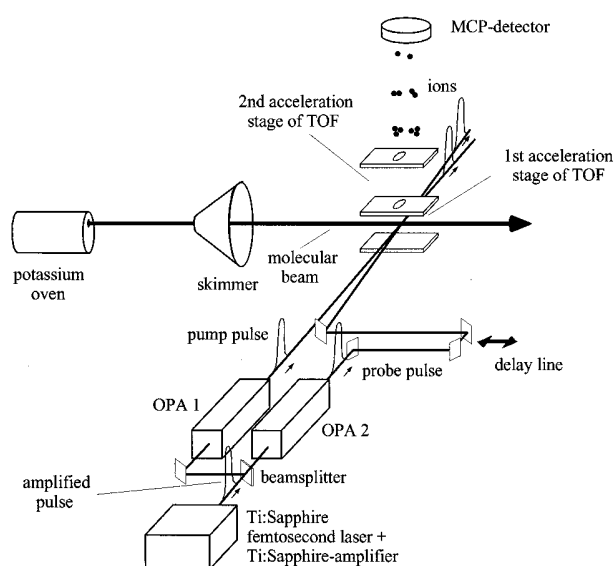


FIG. 2. Schematic view of the experimental setup. The skimmed molecular beam, cooled in a supersonic jet expansion, enters the interaction region from the left. Pump and probe pulses are generated by two identical OPA systems, driven by the output of a commercial Ti:sapphire regenerative amplifier. Pulses tunable in wavelength from about 500 to 750 nm with pulse energies of several μJ and 80 fs length are obtained. The ion signal is detected by a linear time of flight (TOF) mass spectrometer, oriented vertically in this figure.

chamber from the spectroscopy chamber. The latter is evacuated by a 550 l/s turbomolecular pump to about 10^{-7} mbar.

The two color femtosecond laser system is a combination of commercial products: it is headed by a Kerr lens mode-locked Ti:sapphire laser (MIRA, Coherent) producing pulses of 80 fs duration at a repetition rate of 76 MHz. These pulses are regeneratively amplified in a chirped pulse amplifier (CPA-1000, Clark-MXR) to 1.1 mJ per pulse within 90 fs at a repetition rate of 1 kHz. The amplified pulses are divided by a 1:1 beamsplitter and directed into two optical parametric amplifiers (TOPAS, Light Conversion). By second harmonic generation of the signal wave or sum frequency generation of the signal wave with the rest of the optical parametric amplifier (OPA) input beam both OPA output pulses can be tuned between 490 and 750 nm. Their spectral width is approximately 250 cm^{-1} . After passing through prism compressors the duration of the pulses is about 80 fs with energies of some μJ per pulse depending on the wavelength.

Both the pump and the probe beams are focused through pinholes for mode cleaning. The pathlength of the probe beam can be changed by a motorized delay line to control the relative time delay τ between pump and probe pulse. The beams enter the spectroscopy chamber collinearly. A 200 mm achromatic lens is used to focus them into the molecular beam. The interaction spot is located in the center of the acceleration region of a 25 cm linear time of flight (TOF) mass spectrometer equipped with a chevron multichannel plate detector. The potassium dimer signal is isolated from all other cluster ions by setting the integrating window of a

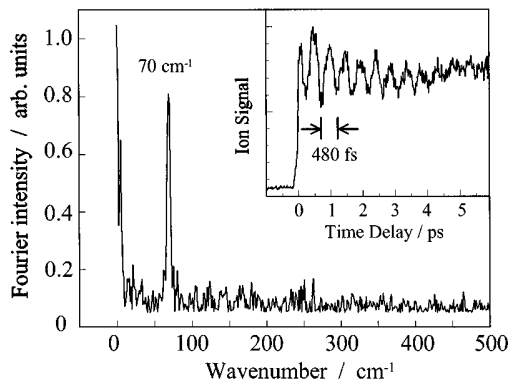


FIG. 3. Transient ion signals obtained for wavelengths of 635 nm (pump) and 578 nm (probe) and the Fourier transform of the time domain signal are shown. The latter exhibits the energy spacings of the coherently superposed vibrational levels in the $|B\rangle$ state. Because of the rapid decay of the oscillations in the transient ion signal energy, differences between neighboring levels due to anharmonicity effects could not be resolved.

boxcar integrator to the appropriate time. The boxcar output is averaged and stored together with the delay line position in a computer.

III. EXPERIMENTAL RESULTS

The vibrational wave packets in the $|B\rangle$ state of the potassium dimer are created by tuning one of the OPA to the $|B\rangle \leftarrow |X\rangle$ transition. Due to the bandwidth of the laser pulses of about 250 cm^{-1} , three to five vibrational levels are coherently excited ($\omega_e = 75\text{ cm}^{-1}$, $\omega_e x_e = 0.39\text{ cm}^{-1}$) at a center wavelength of 635 nm. As the equilibrium nuclear separation in $|X\rangle$ and $|B\rangle$ are similar, the Franck-Condon factors die off quickly with increasing $\Delta\nu$.²⁶ Under the realistic assumption that the complexes in the supersonic expansion are in their vibronic ground state, the mean vibrational level of the wave packet in $|B\rangle$ could not be chosen higher than $\nu' = 10$. The probe pulse had the same duration and bandwidth as the pump pulse. In a first experiment, the probe wavelength was set to the value corresponding to the energy difference between the mean energy of the wave packet and the bottom of the ionic potential. The total ion signal of the potassium dimer ion was detected as a function of delay τ between pump and probe, which was varied from -2 ps to some tens of ps.

In this case, where the sum of pump and probe energies is just the ionization potential, one can expect the transient signal to mirror the wave packet motion in the $|B\rangle$ state. From the potential energy surfaces and the wavelengths of pump and probe photon one can conclude that there should exist an ionization pathway only at the outer classical turning point of the wave packet.

Figure 3 shows a typical result for $\lambda_{\text{pump}} = 635\text{ nm}$, corresponding to the transition $|B(\nu' = 4)\rangle \leftarrow |X(\nu'' = 0)\rangle$ and $\lambda_{\text{probe}} = 578\text{ nm}$. Delay time zero means simultaneous pump and probe pulses. At negative times the probe pulse is first, at positive times the pump pulse is first. At negative times the ion signal is essentially time independent and zero. This ex-

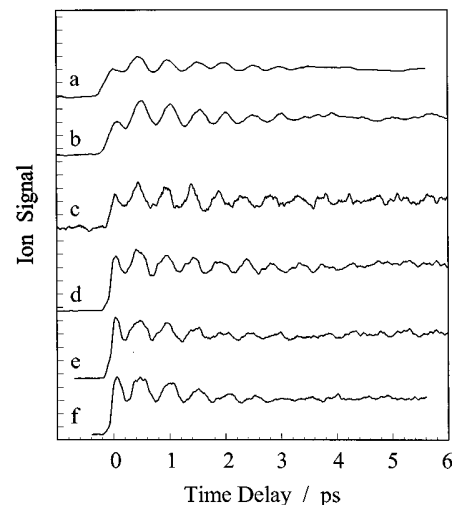


FIG. 4. Transient ion signals obtained by two-color photoionization pump probe spectroscopy are shown in this figure as a function of the probe pulse energy. Starting with low probe pulse energies a: ($\lambda = 585\text{ nm}$), where ionization to the bottom of the potential energy surface of the $|X^+\rangle$ takes place, corresponding to zero excess energy, the wavelength of the probe pulse photon is gradually decreased (b: $\lambda = 580\text{ nm}$, c: $\lambda = 556\text{ nm}$, d: $\lambda = 531\text{ nm}$, e: $\lambda = 517\text{ nm}$, and f: $\lambda = 499\text{ nm}$).

presses the fact that the Frank-Condon factor for a transition into high vibronic levels of $|B\rangle$ (578 nm excites to $\nu' \approx 30$) is negligible and neither pump nor probe pulse alone can ionize the K₂ molecule. Around $\tau = 0$ the ion signal rises with a slope determined by the cross correlation function between pump and probe pulse. For $\tau > 0$ the ion signal has two contributions: a constant offset which lasts longer than 1 ns and an oscillating signal. The latter one is the real time observation of the wave packet motion in the $|B\rangle$ state. Its period of 480 fs corresponds to the wave number spacing of the vibrational levels around $\nu' = 5$ which are ($E_{5 \leftarrow 4} = 71.4\text{ cm}^{-1}$, $E_{6 \leftarrow 5} = 70.7\text{ cm}^{-1}$). The inset of Fig. 3 shows a Fourier transformation of the oscillating part of the ion signal showing a single peak at 70 cm^{-1} . The difference between the wave number spacings due to the anharmonicity of the potential cannot be resolved in this measurement, since the oscillation disappears after $\sim 8\text{ ps}$ limiting the spectral accuracy to $\sim 3\text{ cm}^{-1}$.

In a second experiment we varied λ_{probe} step by step from 620 to 499 nm. The λ_{pump} was held constant at 635 nm for simplicity. If the probe energy is increased, more and more final ion states should participate in the ionization, belonging to all possible distributions of the excess kinetic energy between the electron and the ion. This distribution, however, is limited by the Franck-Condon factors for the $|X^+\rangle \leftarrow |B\rangle$ transition. Since all these pathways result in different, essentially phase shifted transients, the time dependence of the overall ion signal should vanish for large total energy.^{28,29} A simple theory taking into account only the ion ground state shows that at the latest at about 1600 cm^{-1} above the ionization potential, corresponding to 525 nm in our experiment, no transient signal should be left.

The experiment, however, shows a pronounced oscillation pattern for whatever probe wavelength (Fig. 4). Again

there is no ion signal at negative delays. At positive times in all transients the long living constant background is seen. Oscillations with a periodicity of 480 fs are found in all cases even if the total energy is more than 3000 cm⁻¹ higher than the ionization potential. Not only is the periodicity preserved but also its contrast does not change significantly for all probe pulse wavelengths between 620 and 499 nm. It is obvious that there exists a strong discrepancy between the experiment and the naïve theory of three states ($|X\rangle, |B\rangle, |X^+\rangle$) and two photons (pump, probe) taking part in the ionization process. This question will be discussed with the help of time-dependent quantum calculations in the following section.

IV. DISCUSSIONS

To simulate the transient ion spectra obtained in the experiment we performed time-dependent quantum calculations using three electronic states, i.e., the ground state $|X\rangle$, the excited state $|B\rangle$, which is accessed by the pump pulse of 635 nm, and the ionic ground state $|X^+\rangle$. Pump/probe ionization signals are calculated under the following assumptions:

- (i) the initial state before the interaction with the laser pulses is the vibrational ground state ψ_0 of the molecule in state $|X\rangle$.
- (ii) The rotational motion is negligible, i.e., all signals are calculated for a rotational quantum number of $J=0$.
- (iii) The electric dipole approximation is assumed and the dipole moments for the $|B\rangle \leftarrow |X\rangle$ and the $|X^+\rangle \leftarrow |B\rangle$ transitions are set to a constant (see, however, the discussion below).
- (iv) Second order perturbation theory is used, i.e., we assume weak electric fields.
- (v) The laser pulse envelopes are taken as Gaussians with a width (full width at half maximum) of 100 fs.
- (vi) No coupling between the nuclear and electronic degrees of freedom and between the core electrons and the emitted photoelectron is included.
- (vii) The ion signal is proportional to the ionization probability.

Under these assumptions which have been used before to simulate pump/probe ionization spectra,^{19,20,29,30} the nuclear ionic wave function which corresponds to the emission of a photoelectron with kinetic energy E is obtained as (atomic units are used)

$$\begin{aligned} \psi_E(t, \tau) \sim & \int_{-\infty}^t dt_2 \int_{-\infty}^{t_2} dt_1 U_+(t-t_2) \\ & \times f(t_2 - T_2) e^{-i(\omega_2 - E)t_2} U_B(t_2 - t_1) \\ & \times f(t_1 - T_1) e^{-i\omega_1 t_1} U_X(t_1) \psi_0. \end{aligned} \quad (1)$$

Here $f(t_i - T_i)$ are the Gaussian envelope functions of pump ($i=1$) and probe ($i=2$) pulse which are centered at times T_i . Thus the delay time between the pulses is $\tau = T_2 - T_1$. The frequencies of the pulses are ω_i and U_n and are the propagators in the different electronic states.

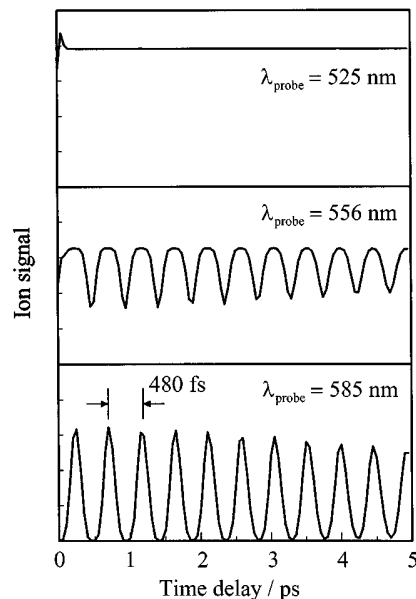


FIG. 5. Calculated transient ion signals [Eq. (2)] for a pump wavelength of 635 nm and probe wavelengths as indicated. Constant transition dipole moments were assumed in the calculation.

The total ion signal is calculated as

$$P(\tau) = \lim_{t \rightarrow \infty} \int dE \langle \psi_E(t, \tau) | \psi_E(t, \tau) \rangle, \quad (2)$$

where the brackets denote integration over the bond distance. In practice the limit in the above equation is reached after the second pulse decayed to zero since afterwards the norm of the wave functions $\psi_E(t, \tau)$ remains constant. We use the split-operator method³¹ for the propagation of the wave packets and the second order integral in Eq. (1) is evaluated as described in Ref. 32. The energy integral is evaluated by discretization of the continuum.

We use the potentials displayed in Fig. 1 in our calculation. Figure 5 shows the transient ion signals, calculated for different probe wavelengths, as indicated. We used an energy grid with a step size of $\Delta E = 0.02 \text{ eV}$. The shown results are converged with respect to this step size. The energy interval for which the ionic wave functions have to be calculated ranges from $\omega_2 - E = 2.06 \text{ eV}$ to $\omega_2 - E = 2.30 \text{ eV}$. For smaller or larger values, the norm of the wave function ψ_E is negligible. For a probe wavelength of 585 nm the signal shows oscillations which correspond to the vibrational period of the B state of K₂. These oscillations are still apparent if the wavelength is decreased to 559 nm. However, a background arises which is due to the summation over the electron energies which are energetically allowed. In the case of $\lambda_{\text{probe}} = 525 \text{ nm}$ the oscillatory behavior of the ion signal is completely missing. The only temporal change is obtained during the time when pump and probe pulse overlap. This behavior has been analyzed before.^{28,30}

If we compare the ion signals to those obtained in the experiment we find two discrepancies: (i) the background which is found experimentally already at longer probe wave-

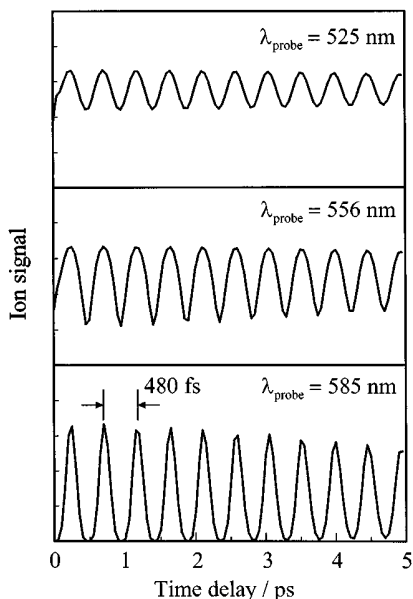


FIG. 6. Same as Fig. 5 but a coordinate dependent transition dipole moment (Eq. 3) for the $|X^+\rangle \leftarrow |B\rangle$ was included in the calculation.

lengths is missing in the theory and (ii) the oscillations apparent in the measured signal remain at shorter wavelengths, whereas they vanish in the calculated signals.

Let us first discuss the latter point. In the calculation it was assumed that the transition dipole moment $\mu_{X^+ \leftarrow B}$ for the $|X^+\rangle \leftarrow |B\rangle$ neither depends on the bond length R nor on the photoelectron energy E . To our knowledge these dependencies are not well known for diatomic molecules. The reason for this is quite simple: a quantum chemical calculation of these moments would involve the full scattering calculation for the ionic state which cannot be performed with standard quantum chemical computer codes. Let us, for simplicity, assume a transition dipole moment function which is a linear function of the bond length

$$\mu_{X^+ \leftarrow B} = \mu_{x^+ \leftarrow B}^0 + \alpha R \quad (3)$$

with α being a positive number. Then the wave packet at different locations is weighted differently. In other words, the transition probability to the final state is larger if the packet is located at the outer turning point of its vibrational motion as it is when the inner turning point is reached. Thus we expect that even for shorter wavelengths a time dependence of the signal can be obtained. The derivative of the dipole moment with respect to R then determines to which extent a deviation from the constant ion signal is obtained. Figure 6 shows the signal for the same wavelengths regarded before (see Fig. 5). The results were obtained with a dipole moment as given in Eq. (3) using a value of $\alpha = 1 \text{ a.u.}$ (corresponding to $\sim 2.5 \text{ Debye}$ at $R = 1 \text{ a.u.}$). Indeed now an explicit time dependence can be found in the ionic population for a wavelength of $\lambda_{\text{probe}} = 585 \text{ nm}$ which reflects the vibrational dynamics in the electronic $|B\rangle$ state.

Let us now turn to the second discrepancy between the calculated and measured transient ion spectra. From the cal-

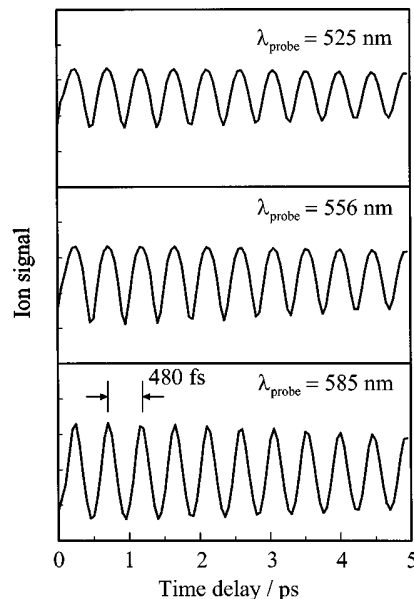


FIG. 7. Calculated total ion signal [Eq. (4)] including a coordinate dependent transition dipole moment and contributions from molecular Rydberg states which converge to the ionic ground state.

culation it is obvious that the direct ionization process cannot be the only one to be discussed since, for a wavelength of 585 nm, which is close to the ionization threshold, no constant background arises in our calculated signal. There exists, however, the possibility that singly excited Rydberg states of the molecule³³ are excited, which decay via autoionization. This, indeed is one of the basic processes which allow for highly resolved zero kinetic energy spectra (ZEKE).³⁴ The Rydberg states of K₂ were analyzed by Broyer *et al.* in two- and three-photon resonantly enhanced multiphoton ionization REMPI experiments and their decay by auto or field ionization was discussed.²⁷ Independent of the lifetimes of these states which range over a very large time scale, the ionization process will occur with a certain efficiency. We may simulate the contribution to the ion signal via the indirect ionization process by calculating the population in various Rydberg states which have potential energy curves equal to the ionic one but are shifted towards lower energies. Within our perturbative approach [see Eq. (1)] this is equivalent to an increase of the probe laser frequency ω_2 . This in fact yields the same constant background as in the case of the short wavelength excitation (see Fig. 5, upper panel). Of course here we have neglected possible interference effects between the different ionization pathways. The relative intensity of the background signal depends on the dipole coupling elements between the $|B\rangle$ state and the electronic Rydberg states. If we assume them to be equal to the one of the neutral-to-ion transition we may now calculate the signal as

$$P_{\text{tot}}(\tau) = P(\tau) + P_{\text{Ryd}}(\tau), \quad (4)$$

where $P_{\text{Ryd}}(\tau)$ is the signal obtained for $\lambda_{\text{probe}} = 525 \text{ nm}$. This is justified since contributions for shorter wavelengths have negligible intensities. The results are displayed in Fig.

7. The summed signal for 585 nm now shows the expected background signal. Of course the relative height of the background is not known since a proper calculation would have to take account of the full autoionization process which is not done here.

V. SUMMARY

The vibrational wave packet dynamics in the $|B\rangle\ ^1\Pi_u$ state of the potassium dimer was studied on a subpicosecond time scale. Oscillation periods of the vibrational wave packets of 480 fs were measured reflecting the energy spacing of the vibrational states of 70 cm^{-1} (Fig. 3). The interests were in particular focused on the probe process, since the experimental data cannot be understood by a simple model including only $|X\rangle$, $|B\rangle$, and ion-state $|X+\rangle$. All transients, detected as a function of the energy of the probe photon, show the $|B\rangle$ state dynamics on top of a long lived background signal (Fig. 4). These results can be explained by the inclusion of an R -dependent dipole moment for the $|X+\rangle \leftarrow |B\rangle$ transition and the addition of a second indirect ionization pathway via long lived Rydberg states.

ACKNOWLEDGMENTS

Financial support from the German Science Foundation (Project Ki 202/11-1/11-2) and from the Fonds der Chemischen Industrie is highly acknowledged.

- ¹A. Zewail, Faraday Discuss. Chem. Soc. **91**, 207 (1991).
- ²A. Zewail, J. Phys. Chem. **97**, 12427 (1993).
- ³A. Zewail, *Femtochemistry* (World Scientific, Singapore, 1994), Vols. 1 and 2.
- ⁴V. Engel, in *Atomic, Molecular and Optical Physics Handbook*, edited by G. W. F. Drake (AIP, Woodbury, NY, 1996).
- ⁵*Femtosecond Chemistry*, edited by J. Manz and L. Wöste (VCH, Heidelberg, 1995).
- ⁶C. C. Hayden and D. W. Chandler, J. Chem. Phys. **103**, 10465 (1995).
- ⁷M. Schmitt, G. Knopp, A. Materny, and W. Kiefer, Chem. Phys. Lett. **270**, 9 (1997).
- ⁸M. Gruebele, G. Roberts, M. Dantus, R. M. Bowman, and A. H. Zewail, Chem. Phys. Lett. **166**, 459 (1990); M. Gruebele and A. H. Zewail, J. Chem. Phys. **98**, 883 (1993).
- ⁹A. Assion, T. Baumert, V. Seyfried, V. Weiss, E. Wiedenmann, and G. Gerber, Z. Phys. D **36**, 265 (1996).
- ¹⁰P. M. Felker and A. H. Zewail, in Ref. 5, Chap. 5.
- ¹¹P. M. Felker, J. Phys. Chem. **96**, 7844 (1992).
- ¹²S. Rutz and E. Schreiber, Chem. Phys. Lett. **269**, 9 (1997).
- ¹³M. J. J. Vrakking, D. M. Villeneuve, and A. Stolow, Phys. Rev. A **54**, R37 (1996).
- ¹⁴T. Baumert, B. Bühl, M. Grosser, R. Thalweiser, V. Weiss, E. Wiedenmann, and G. Gerber, J. Phys. Chem. **95**, 8103 (1991).
- ¹⁵T. Baumert, V. Engel, C. Meier, and G. Gerber, Chem. Phys. Lett. **200**, 488 (1992).
- ¹⁶S. Rutz, S. Greschik, E. Schreiber, and L. Wöste, Chem. Phys. Lett. **257**, 365 (1996).
- ¹⁷S. Rutz, R. de Vivie-Riedle, and E. Schreiber, Phys. Rev. A **54**, 306 (1996).
- ¹⁸I. Sh. Averbukh, M. J. J. Vrakking, D. M. Villeneuve, and A. Stolow, Phys. Rev. Lett. **77**, 3518 (1996).
- ¹⁹T. Baumert, V. Engel, C. Rötgermann, W. T. Strunz, and G. Gerber, Chem. Phys. Lett. **191**, 639 (1992); T. Baumert, V. Engel, C. Meier, and G. Gerber, *ibid.* **200**, 488 (1992); V. Engel, T. Baumert, Ch. Meier, and G. Gerber, Z. Phys. D **28**, 37 (1993).
- ²⁰R. de Vivie-Riedle, K. Kobe, J. Manz, W. Meyer, B. Reischl, S. Rutz, E. Schreiber, and L. Wöste, J. Phys. Chem. **100**, 7789 (1996).
- ²¹G. Rodriguez and J. G. Eden, Chem. Phys. Lett. **205**, 371 (1993); G. Rodriguez, P. C. John, and J. G. Eden, J. Chem. Phys. **103**, 10473 (1995).
- ²²M. Brau and V. Engel, Z. Phys. D **39**, 301 (1997).
- ²³I. Fischer, M. J. J. Vrakking, D. M. Villeneuve, and A. Stolow, Chem. Phys. **207**, 331 (1996).
- ²⁴L.-E. Berg, M. Beutter, and T. Hansson, Chem. Phys. Lett. **253**, 327 (1996).
- ²⁵J. Heufelder, H. Ruppe, S. Rutz, E. Schreiber, and L. Wöste, Chem. Phys. Lett. **269**, 1 (1997).
- ²⁶J. Heinze, U. Schuehle, F. Engelke, and C. D. Caldwell, J. Chem. Phys. **87**, 45 (1987).
- ²⁷M. Broyer, J. Chevaleyre, G. Delacretaz, S. Martin, and L. Wöste, Chem. Phys. Lett. **99**, 206 (1983).
- ²⁸V. Engel, Chem. Phys. Lett. **178**, 130 (1991).
- ²⁹M. Seel and W. Domcke, J. Chem. Phys. **95**, 7806 (1991).
- ³⁰M. Seel and W. Domcke, Chem. Phys. **151**, 59 (1991).
- ³¹J. A. Fleck, J. R. Morris, and M. D. Feit, Appl. Phys. **10**, 129 (1976); M. D. Feit, J. A. Fleck, and A. Steiger, J. Comput. Phys. **47**, 412 (1982).
- ³²V. Engel, Comput. Phys. Commun. **63**, 228 (1991).
- ³³J. Mulliken, J. Am. Chem. Soc. **86**, 3183 (1964); **88**, 1849 (1966); **91**, 4615 (1969).
- ³⁴K. Müller-Dethlefs and E. W. Schlag, Annu. Rev. Phys. Chem. **42**, 109 (1991); K. Müller-Dethlefs, E. W. Schlag, E. Grant, K. Wang, and V. McKoy, Adv. Chem. Phys. **90**, 1 (1995).



20 March 1998

Chemical Physics Letters 285 (1998) 240–245

**CHEMICAL
PHYSICS
LETTERS**

Femtosecond vibrational wavepacket spectroscopy in the electronic ground state of K₂

H. Schwoerer, R. Pausch, M. Heid, W. Kiefer *

Institut für Physikalische Chemie der Universität Würzburg, Am Hubland, D-97074 Würzburg, Germany

Received 3 November 1997; in final form 30 December 1997

Abstract

Vibrational wavepacket propagation in the electronic ground state |X⟩ of supersonic jet cooled potassium dimers was investigated with a femtosecond pump–probe experiment. The wavepackets were generated by resonance enhanced stimulated Raman scattering into $\bar{v}_X'' = 5$ and interrogated by a time delayed three photon ionization process. The choice of the wavelength of the probe photons enabled a pure detection of ground state wavepacket dynamics. Fourier analysis of the wavepacket oscillation with a period of 375 fs reveals a one color stimulated emission pumped component around 92 cm⁻¹ and a stimulated Raman pumped component around 88 cm⁻¹. © 1998 Elsevier Science B.V.

1. Introduction

The concept of the preparation of a vibronic wavepacket with a femtosecond laser pulse and a subsequent probing step with a laser pulse on the same timescale to monitor the evolution of the vibronic wavepacket, pioneered by Ahmed Zewail in the late eighties, is a powerful experimental technique. It allows to study in real time phenomena like propagation of the wavepacket within a potential energy surface or in a transition state, photodissociation, intramolecular energy redistribution or even controlling of reaction pathways [1–3]. The method has been applied with great success to a large variety of molecular systems from diatomics and small clusters through small molecules undergoing elementary reactions to biologically relevant systems [4,5]. Several probing and detection schemes such as fluores-

cence [6], multiphoton ionization [7,8] and coherent anti-Stokes Raman scattering (CARS) [9] have been adapted to the technique.

Diatom systems and in particular alkali metal dimers, which can be produced purely in their vibronic ground state by a supersonic jet expansion, remained of interest since the first days of femtosecond wavepacket spectroscopy, because some fundamental aspects of the method could be demonstrated and highlighted with exceptional clarity: NaI for example serves as a model system for the behavior of a wavepacket at crossing potential energy surfaces [10,11]. Wavepacket dynamics in different, and also in coupled electronically excited states of Na₂ were extensively studied including detailed investigations of the multiphoton ionization pathways in the probe step [7,12]. Spin orbit coupled electronic states of K₂ were investigated by their influence on the wavepacket's propagation with isotopomer resolution [13]. Interferences of wavepackets in Cs₂ could

* Corresponding author.

be generated and detected [14]. Fractional revivals of wavepackets due to the beating of portions of the wavepacket with different periodicities were also reported in Br_2 and NaK and nicely illustrated with the help of spectrograms [15,16]. In a preceding pump–probe experiment on potassium dimers we could show that the electronic transition dipole moment which is responsible for the ionization probe step varies with the position of the wavepacket on its potential surface [17].

However, the method so far has been mainly applied to investigate the vibrational motion of neutral molecules in one of their electronically *excited states*, because the excited states are accessible with one photon from a femtosecond laser pulse in the visible wavelength regime. To our knowledge only a few exceptions have been reported: In an ordinary pump probe experiment in the case of very high pump intensity a small contribution of a ground state wavepacket can be generated by stimulated emission pumping within a single pump pulse in addition to the dominating generation of a wavepacket in an electronically excited state by one photon excitation [18]. A second approach is the socalled NENEPO (NEgative-NEutral-POsitive) technique: By detaching the extra electron of a singly charged anion with an fs pump pulse a ground state wavepacket of the neutral species can be generated and subsequently interrogated by ionizing to the cation. With the NENEPO method the nuclear motion of silver trimers after neutralization has been monitored [19]. And finally a coherent anti-Stokes Raman scattering experiment, where the second pump pulse was delayed with respect to the first pump and the Stokes pulse, was applied to benzene [9] and iodine [20] in the vapour phase. The coherent optical signal at the anti-Stokes wavelength as a function of the time delay displayed ground state wavepacket oscillations.

In this paper, we introduce an experimental concept which enables us to study selectively the vibrational wavepacket motion in the electronic *ground state* of a species produced in a supersonic jet expansion and show first results for an application to the potassium dimer. The method essentially consists of two major spectroscopic steps and a mass selective detection scheme (Fig. 1). First the preparation of a vibrational wavepacket in the electronic ground state via resonant two color stimulated Raman scattering:

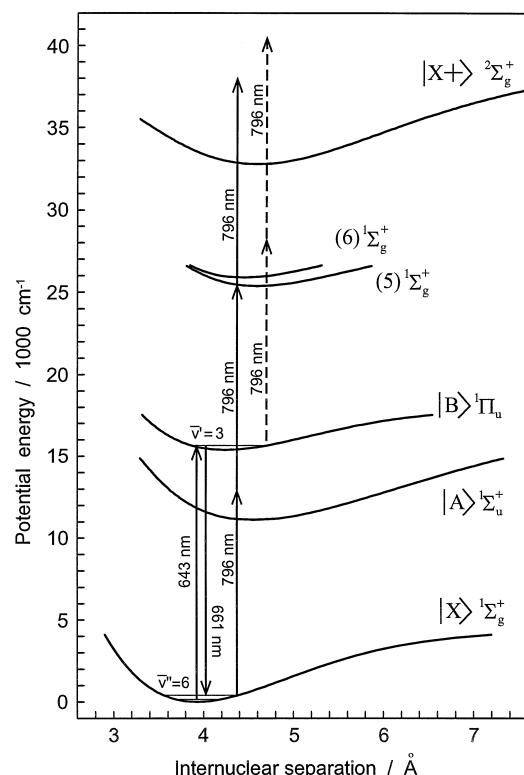


Fig. 1. Potential energy surfaces of the potassium dimer. The $|\text{X}\rangle^1\Sigma_g^+$ state wavepacket is generated by a stimulated Raman process with the pump pulse at 643 nm and the dump pulse at 661 nm. The $|\text{B}\rangle^1\Pi_u$ state is used as an intermediate resonance. The time delayed three photon ionization at $\lambda = 796 \text{ nm}$ selectively probes the ground state wavepacket by using the $(5)^1\Sigma_g^+$ state as an energy and a wavepacket position filter. In contrary to that, the probe process of a wavepacket in $|\text{B}\rangle$ (dashed arrows) does not exhibit a position selectivity.

The wavelength of an ultrashort laser pulse (pump) is tuned to the resonance of a transition from the ground state $|\text{X}\rangle$ to an electronically excited state. A second, simultaneous ultrashort laser pulse (dump) with a slightly longer wavelength transfers a part of the excited state population back to the ground state. Due to the bandwidth of the laser pulses of some hundreds of wavenumbers a wavepacket consisting of several coherently excited vibrational states of $|\text{X}\rangle$ is generated. Its mean vibrational level can be chosen by the energy difference of the two involved photons within the limits of the Franck–Condon rule.

This wavepacket starts evolving in time until it is probed by a time delayed multiphoton ionization process, which preferentially ionizes the ground state

population of the molecule by appropriate resonance enhancement. The ionization path from the ground state must be favoured from the path from the excited state by two aspects: The probability should be higher even though at least one more photon is needed, which requires one or more intermediate resonant states. The second even more important aspect is the selectivity of the path with respect to the vibrational coordinate. Only if the ionization depends on the position of the wavepacket on the potential energy surface its time evolution can be followed by counting the total number of ions at different delays of the probe pulse. This selectivity can be achieved either by pure energy conditions, e.g. if the first photon can only be absorbed at one of the turning points of the wavepacket on its way on the potential energy surface, or by a coordinate dependent transition dipole moment or of course a combination of both [17]. On the other hand the ionization from the intermediate state in the stimulated Raman process should neither be resonance enhanced nor coordinate selective, for example ending very high in the ion potential or even dissociating the ion. The mass selective detection to restrict the experiment to the desired species of the supersonic jet, in our case the potassium dimers, is accomplished by means of a time-of-flight mass spectrometer.

2. Experimental

The experimental setup consists of a molecular beam apparatus, a three color femtosecond laser system, a pump–probe setup and a mass selective detection scheme (Fig. 2).

The potassium dimers are generated in a supersonic jet expansion from a cartridge heated to 450°C through a nozzle of 100 μm diameter into a vacuum chamber. The expansion is backpressured with 1–3 atm of argon gas. The jet passes a skimmer before entering the interaction spot with the laser beams. More details of the molecular beam apparatus are described in Ref. [17].

The head of the femtosecond laser system is a Kerr lens modellocked Ti:sapphire laser (MIRA, Coherent). It is followed by a regenerative Ti:sapphire amplifier with a repetition rate of 1 kHz (CPA-1000,

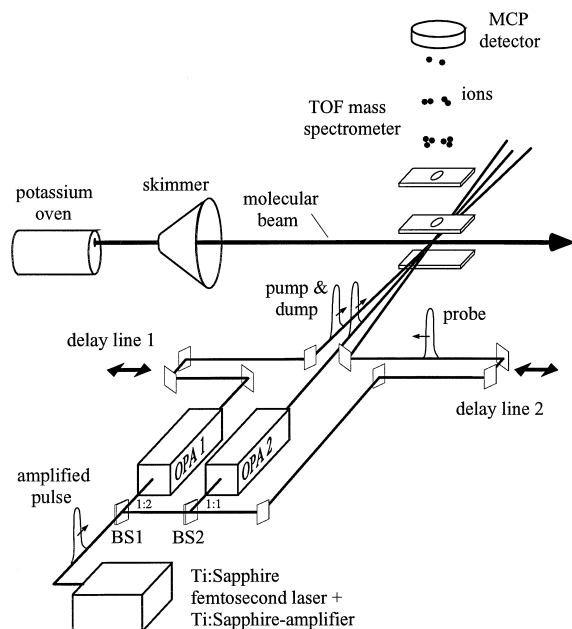


Fig. 2. Schematic view of the experimental setup. The skimmed molecular beam, cooled in a supersonic jet expansion, enters the interaction region from the left. The pump, dump and probe pulses are produced by splitting the output of a Ti:Sapphire based regenerative amplifier system into three equal parts (BS1 and BS2). The wavelengths of pump and dump pulses are independently tunable between 500 and 750 nm by two optical parametric amplifiers OPA 1 and OPA 2. Delay line 1 synchronizes pump and dump pulses at the crossing point with the molecular beam. The delay of the probe pulse ($\lambda_{\text{probe}} = 796 \text{ nm}$) with respect to pump and dump pulse is varied during the experiment by delay line 2. All three pulses cross the molecular beam collinearly which is not shown for clearness of the drawing. The ions are detected by a 250 mm linear time-of-flight mass spectrometer (TOF) oriented vertically in this figure.

Clark MXR), which delivers pulses with a wavelength of 796 nm, an energy of 1.1 mJ and a duration of about 90 fs. The beam is divided into three equal parts by beam splitters BS1 and BS2, two of which are pumping the optical parametric amplifiers (TOPAS, Light Conversion, Ltd.). The frequency doubled OPA outputs serve as pump and dump pulses with wavelengths of 643 nm and 661 nm, respectively. Both pulses are recompressed by two prism compressors (not shown in Fig. 2) to about 70 fs and are made synchronous with delay line 1. Just before entering the vacuum chamber they carry an energy of up to 100 nJ. The third portion of the amplifier output is used as the probe pulse. To achieve a variable time delay to the pump and dump

pulses it is passed through a second motorized delay line, its energy before entering the chamber is up to several tens of μJ . All three beams are made collinear by two additional beam splitters and are focused onto the molecular beam by a spherical lens with a focal length of 200 mm (not shown in Fig. 2).

To detect the ions, the interaction spot of the molecular beam and the laser pulses is located in the first acceleration stage of a 250 mm long linear time-of-flight mass spectrometer. By means of a BOXCAR integrator, the signals from the K_2 ions are selected and recorded as a function of the delay time between the pump/dump process and the probe process.

3. Results and discussion

The potassium dimers in the supersonic jet are assumed to be in their electronic and vibrational ground state before entering the interaction regime. The ground state vibrational wavepackets of K_2 are created by a resonance enhanced stimulated Raman process from the $|\text{X}\rangle^1\Sigma_g^+$ state via the $|\text{B}\rangle^1\Pi_u$ state back to $|\text{X}\rangle$ (Fig. 1). From previous fs pump–probe experiments it is known that wavepackets with mean vibrational quantum numbers up to 10 can be produced in $|\text{B}\rangle$ by a similar fs laser pulse for the pump process as is used here [17]. For higher quantum numbers the Frank Condon factors become very small [21]. The mean wavelength of the pump pulse was set to 643 nm corresponding to the $v'_\text{B} = 3 \leftarrow v''_\text{X} = 0$ transition. Corresponding to the spectral width of the pulses of about 200 cm^{-1} and the vibrational constant of $\omega_e(\text{B}) = 75 \text{ cm}^{-1}$ the $|\text{B}\rangle$ state wavepacket consists of around 3–5 coherently excited states. The wavelength of the synchronous dump pulse which stimulates instantaneous repopulation of the electronic ground state is chosen to be 661 nm. With the vibrational constant of the ground state $\omega_e(\text{X}) = 92 \text{ cm}^{-1}$ and the spectral width of about 300 cm^{-1} as the convolution of the bandwidths of pump and dump laser pulse the ground state wavepacket should consist again of about 3–5 vibrational states with a mean quantum number around 4–5. Both, the wavepacket in $|\text{B}\rangle$ and $|\text{X}\rangle$ now start oscillating in their potential, but due to the different energy spacings between the vibrational levels with different periodicities.

In order to monitor selectively the dynamics in the ground state $|\text{X}\rangle$ the wavelength of the probe laser pulse has to be selected carefully. One possibility in the given configuration is a probe wavelength of around 800 nm (Fig. 1) which just happens to be the fundamental wavelength of our amplifier: The ground state wavepacket can be ionized by a three photon process, exactly reaching the (5) $^1\Sigma_g^+$ state after absorption of two photons. This resonance increases the efficiency of the path and introduces a coordinate selectivity, since for energetic reasons the excitation of the (5) state is only possible at the outer turning point of the wavepacket's motion in $|\text{X}\rangle$. On the other hand the ionization from the $|\text{B}\rangle$ state needs two photons, surpasses the (5) and (6) states and ends up very high in the ion potential $|\text{X}+\rangle$ ($\sim 8000 \text{ cm}^{-1}$).

Fig. 3 shows the ion signal as a function of the time delay between pump/dump process and the probe pulse (delay line 2 in Fig. 2). At negative times the probe pulse ($\lambda_{\text{probe}} = 796 \text{ nm}$) interacts earlier with the molecules as the stimulated Raman process by the synchronous pump and dump pulse ($\lambda_{\text{pump}} = 643 \text{ nm}$ and $\lambda_{\text{dump}} = 661 \text{ nm}$). Time zero corresponds to the synchronous arrival of all three

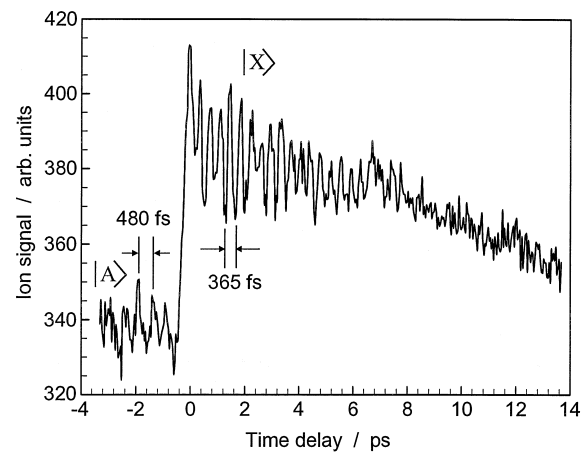


Fig. 3. Transient ion signal as a function of the time delay of the probe pulse with respect to pump and dump pulses. For positive delay times, when the pump/dump process precedes the probe process, the ion signal images the wavepacket oscillation in the electronic ground state $|\text{X}\rangle$. This wavepacket with a periodicity of 365 fs is generated by a two photon process from the pump and the dump pulse and interrogated by the probe pulse. At negative delay times a wavepacket in the excited $|\text{A}\rangle$ state with a period of 480 fs is observed. In this case the preceding probe pulse generates the wavepacket and pump or dump pulses act as the probe.

pulses. At positive times the probe is delayed with respect to pump and dump. The pulse energies of pump, dump and probe pulses were set to 20 nJ, 30 nJ and 100 nJ, respectively. Each data point is accumulated over 2000 events which takes 2 seconds.

At $t < 0$ a small oscillation pattern with a periodicity of 480 fs is detected on top of a constant background. At negative times the probe pulse can excite a wavepacket in the $|A\rangle^1\Sigma_u^+$ state with $\bar{v}_A = 21$ which will be probed by either the pump or the dump pulse. Due to the larger equilibrium internuclear distance in the $|A\rangle$ state compared to the one in $|X\rangle$ these high lying vibrational states can be populated [13]. The periodicity of the ion signal matches the vibrational spacing of 65 cm^{-1} around $v'_A \approx 21$.

At $t = 0$ the ion signal raises and starts oscillating for several ps with a period of 365 fs. This is the period of the internuclear vibration in the electronic ground state $|X\rangle$. The ion signal is a pure image of the ground state vibrational motion. A slight beating can be seen in the signal at the third, seventh and eleventh minimum. After about 9 ps the oscillation vanishes in the noise.

A spectral analysis (Fig. 4) enlightens the origins of the different contributions to the transient signal after $t = 0$. All data points between $t = 0$ and $t = 9$ ps were subjected to a Fourier transformation without further manipulation except for a subtraction of the slowly decreasing background. The main features of the Fourier spectrum are the two peaks at 92 cm^{-1} and 88 cm^{-1} .

Even though these peaks contain only a few points, there are two good reasons to believe that this feature, which was reproducible, is not an artifact: The spectral resolution of the Fourier transform of about $3\text{--}4 \text{ cm}^{-1}$, determined by the time interval of 9 ps, is good enough to resolve this splitting of the peak. Furthermore the splitting into two contributions and the asymmetry are robust against a change of the Fourier transform limit between 8 ps and 13.5 ps.

In addition to these experimental tests the physical interpretation makes the data reasonable: The component with its maximum at 92 cm^{-1} expresses the dynamics of a wavepacket generated by stimulated emission pumping within the pump pulse itself. This should consist of the vibronic levels 0, 1 and 2,

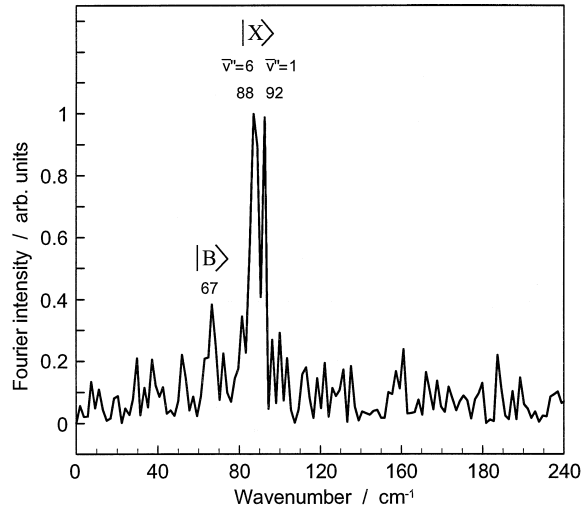


Fig. 4. Spectral analysis of the transient ion signal of Fig. 3 for positive delay times. The vibrational wavepacket in the electronic ground state $|X\rangle$ consists of a contribution around 88 cm^{-1} due to a stimulated Raman process with a pump pulse photon and a dump pulse photon ($\lambda_{\text{pump}} = 643 \text{ nm}$ and $\lambda_{\text{dump}} = 661 \text{ nm}$, respectively). The mean vibrational quantum number of this part is $\bar{v}'' = 6$. The second contribution around 92 cm^{-1} , corresponding to $\bar{v}'' = 1$, is generated by stimulated emission pumping by the pump pulse or the dump pulse itself. A small residual signal from the $|B\rangle$ state wavepacket can be recognized around 67 cm^{-1} .

whose wavenumber differences are $\Delta\bar{\nu}_{0,1} = 92 \text{ cm}^{-1}$ and $\Delta\bar{\nu}_{1,2} = 91.2 \text{ cm}^{-1}$ [22], which match very well with the position of the line. The component at lower wavenumbers, around 88 cm^{-1} , shows the motion of a wavepacket generated by a stimulated Raman process by the pump and the dump pulse from $|X\rangle(v'' = 0)$ into $|X\rangle(\bar{v}'' = 6)$. According to the anharmonicity of the potential the corresponding wavenumber splittings are $\Delta\bar{\nu}_{5,6} = 88.4 \text{ cm}^{-1}$ and $\Delta\bar{\nu}_{6,7} = 87.7 \text{ cm}^{-1}$ [22]. The linewidth of the stimulated Raman wavepacket should be larger since the convoluted spectral shape of the two photon process covers vibrational levels higher and lower than the center, contrary to the stimulated emission pumped wavepacket which cannot be extended below $v'' = 0$. The quality of the data does not allow for a positive verification of the different linewidths, but at least the result tends into the right direction. However, the mean vibrational level of $\bar{v}'' = 6$ is slightly larger than expected. In fact the displayed measurement was optimized by a delay of the dump pulse with respect of the pump pulse of 100 fs. This gives the wavepacket in the $|B\rangle$ state the time to move out-

wards which should increase or open the Franck–Condon windows to higher vibrational levels in the ground state $|X\rangle$.

The small signal around 67 cm^{-1} is a contribution from the $|B\rangle$ state wavepacket created by a one photon absorption from the pump pulse. Its existence can already be seen in the time domain signal as the weakly pronounced beating with a periodicity of 3–4 oscillation periods. The dump pulse also contributes to the stimulated emission pumping but less efficient since its maximum does not reach the $|B\rangle$ potential and therefore the two photon process is less resonance enhanced. This was verified by repeating the experiment blocking either dump or pump pulse and keeping the intensities unchanged. The small appearance of the $|B\rangle$ wavepacket again shows the strong selection of the ground state dynamics through the special choice of the ionization path.

4. Conclusions

We introduced a method to investigate vibrational wavepacket dynamics in the electronic ground state where the ground state wavepacket was generated by a stimulated Raman process and probed by time delayed resonance enhanced three photon ionization and applied it to the potassium dimer K_2 . Two contributions are clearly separated in the spectral analysis of the transient signal: Both, the pump and the dump pulse alone generate a wavepacket in the lowest vibrational states by stimulated emission pumping with two photons from either the pump or the dump pulse. The more interesting contribution to the wavepacket is due to a true stimulated Raman process by one photon from the pump pulse and one photon from the dump pulse. Its oscillation period is longer due to the anharmonicity of the ground state potential and its mean vibrational level can be shifted by changing the wavelength difference between pump and dump pulse. The intermediate resonance conditions of the probe step must be chosen carefully to suppress the detection of excited state wavepackets, namely the wavepacket in the intermediate state in the stimulated Raman process.

The vibrational wavepacket induced by stimulated Raman scattering is the promising outcome of the experiment. Its application to more complex

molecules might open ways to the real time investigation of ground state intramolecular dynamics of and also between different modes of freedom.

Acknowledgements

Financial support from the Deutsche Forschungsgemeinschaft (DFG project Ki 202/11-1/11-2) and from the Fonds der Chemischen Industrie is highly acknowledged.

References

- [1] A.H. Zewail, Faraday Discuss. Chem. Soc. 91 (1991) 207.
- [2] A.H. Zewail, J. Phys. Chem. 97 (1993) 12427.
- [3] A.H. Zewail, Femtochemistry, Vols. 1/2, World Scientific, Singapore, 1994.
- [4] J. Manz, L. Wöste (Eds.), Femtosecond Chemistry, VCH, Heidelberg, 1995.
- [5] M. Chergui (Ed.), Femtochemistry, World Scientific, Singapore, 1996.
- [6] M.J. Rosker, M. Dantus, A.H. Zewail, J. Chem. Phys. 89 (1988) 6113.
- [7] T. Baumert, B. Bühler, M. Grosser, R. Thalweiser, V. Weiss, E. Wiedenmann, G. Gerber, J. Phys. Chem. 95 (1991) 8103.
- [8] S. Rutz, K. Kobe, H. Kühling, E. Schreiber, L. Wöste, Z. Phys. D 26 (1993) 276.
- [9] C.C. Hayden, D.W. Chandler, J. Chem. Phys. 103 (1995) 10465.
- [10] T.S. Rose, M.J. Rosker, A.H. Zewail, J. Chem. Phys. 91 (1989) 7415.
- [11] G. Knopp, M. Schmitt, A. Materny, W. Kiefer, J. Phys. Chem. 101 (1997) 4852.
- [12] S. Rutz, S. Greschnik, E. Schreiber, L. Wöste, Chem. Phys. Lett. 257 (1996) 365.
- [13] S. Rutz, R. de Vivie-Riedle, E. Schreiber, Phys. Rev. A 54 (1996) 306.
- [14] V. Blanchet, C. Nicole, M.A. Bouchene, B. Girard, Phys. Rev. Lett. 78 (1997) 2716.
- [15] M.J.J. Vrakking, D.M. Villeneuve, A. Stolow, Phys. Rev. A 54 (1996) R37.
- [16] J. Heufelder, H. Ruppe, S. Rutz, E. Schreiber, L. Wöste, Chem. Phys. Lett. 269 (1997) 1.
- [17] H. Schwoerer, R. Pausch, M. Heid, V. Engel, W. Kiefer, J. Chem. Phys. 107 (1997), in press.
- [18] T. Baumert, V. Engel, C. Meier, G. Gerber, Chem. Phys. Lett. 200 (1992) 488.
- [19] S. Wolf, G. Sommerer, S. Rutz, E. Schreiber, T. Leisner, L. Wöste, R.S. Berry, Phys. Rev. Lett. 74 (1995) 4177.
- [20] M. Schmitt, G. Knopp, A. Materny, W. Kiefer, Chem. Phys. Lett. 270 (1997) 9.
- [21] J. Heinz, U. Schuehle, F. Engelke, C.D. Caldwell, J. Chem. Phys. 87 (1987) 45.
- [22] G. Herzberg, Molecular structure and molecular spectra, Vol. 1, Van Nostrand Reinhold, New York, 1950.

Selective generation and control of excited vibrational wave packets in the electronic ground state of K₂

R. Pausch, M. Heid, T. Chen, W. Kiefer,^{a)} and H. Schwoerer

Institut für Physikalische Chemie der Universität Würzburg, Am Hubland, D-97074 Würzburg, Federal Republic of Germany

(Received 4 November 1998; accepted 18 February 1999)

We investigate the generation and real-time monitoring of coherent vibrational wave packets in the electronic ground state of supersonic jet-cooled potassium dimers. vibrationally excited wave packets with mean quantum numbers $\bar{v}=6$ and $\bar{v}=11$ are generated by a stimulated Raman process which is enhanced by an electronic resonance. Two ultrashort laser pulses of different wavelengths induce the pump and the dump process. The population of the final hot ground-state wave packets is successfully controlled by a variable time delay between the pump and the dump process, which enables us to wait with the dumping for the optimal Franck-Condon overlap between the intermediate and the predicted final vibrational wave packet in the electronic ground state. © 1999 American Institute of Physics. [S0021-9606(99)00219-6]

I. INTRODUCTION

The first and important step of optimal laser control of the pathway and yield of many chemical reactions is the selective population of excited molecular vibrations of the reactant. Excited vibrational levels can act as intermediate or transition states to the desired product state if Franck-Condon windows or electronic transition probabilities to the product emerge in the excited vibrational state. Bound vibrational states above the barrier of a double-well potential of two isomers, for example, can allow the transition from one isomer to the other. Unimolecular reactions with different possible products might be conducted into a preselected reaction path by exciting a vibrational wave packet with the appropriate energy and shape. And finally, intramolecular vibrational relaxation processes can be studied in detail either state selectively or even time resolved.

Two approaches to the preparation of the desired vibrational excitation are conceivable. First, a single molecular eigenstate is populated with high energy resolution. The eigenstate has no observable time dependence and is spread over the whole coordinate space according to the wave function. Second, a coherent superposition of vibrational states to a vibrational wave packet is excited. The wave packet can be well localized at certain positions on the potential energy surface and can move and vary its shape in time. Both approaches, the energy selective and the time selective, have been treated theoretically in great detail for diatomic molecules as well as for more complex systems.^{1–3} Reviews and comprehensive presentations of recent developments in related theory and experiments are collected in Refs. 4–11.

The state selective method of Manz and Paramonov^{1,2} describes a stepwise population transfer from the reactant ground state to the target state by a series of picosecond or subpicosecond infrared (IR) pulses of simple shape. Depending on the electric field strength of the individual IR pulses,

their relative timing, and in some cases even their relative phases, almost complete selective population transfer into vibrational states as high as $v=20$ in OH has been achieved theoretically. The spectral bandwidth of the IR pulses is narrow enough to select single vibrational levels, but broad enough to complete the excitation before competing intramolecular vibrational relaxation processes take place. In their recent work,^{4,5} Manz and Paramonov extended their steady-state method and have prepared quasicoherent molecular vibrations in the dissociative continuum of the electronic ground state in the HONO₂ molecule.

The second theoretical approach, first invented by Tannor and Rice,³ uses a femtosecond pump-dump scheme. A localized vibrational wave packet is created by a vertical transition to an intermediate excited electronic state with a first ultrashort laser pulse. The wave packet starts moving along the excited potential energy surface until it passes through a Franck-Condon window with respect to the prescribed target state and is dumped there vertically by a second ultrashort laser pulse. In their first proposal of this method, the evolution time of the wave packet on the intermediate potential surface determined the choice between two dissociation exit channels in the electronic ground state of the molecule. An important requirement for the success of this method is a difference in position or orientation of the two involved potential energy surfaces with respect to the molecular coordinates. The efficiency of the pump-dump scheme, and in particular the localization of the wave packet on certain points on the potential surface, can be improved if a frequency chirp is employed to the ultrashort laser pulses.¹² Another very efficient way to excite a ground-state vibrational motion is the technique of impulsive stimulated Raman scattering,^{13,14} where a ground-state wave packet is generated while population transfer to the electronic excited surface is blocked. With short intense laser pulses, a new type of ground-state wave packet can be generated by impulsive excitation,^{15,16} which carves a coherent dynamical

^{a)}Electronic mail: wolfgang.kiefer@mail.uni-wuerzburg.de

“hole” out of the ground-state surface density. Whereas these methods involve two electronic states, the above described steady-state approach of Manz and Paramonov can take place within a single electronic state, typically the ground state.

Even though calculated optimal light fields turn out to have sophisticated envelopes and unconventional carrier frequencies, they are usually said to be theoretically robust against rough changes, and some experimental techniques have been successfully applied to the selective excitation of molecular vibrations in the electronic ground state in the frequency domain as well as in the time domain. The target in our experiment will be the generation of vibrational wave packets of prechosen mean vibrational energy in the electronic ground state of a potassium dimer and to monitor its evolution in real time. We use a stimulated Raman process with two ultrashort laser pulses of different wavelengths and control the efficiency of the dump process by introducing a time delay between the pump and the dump laser pulses. The detailed procedure will be described after mentioning some of the former experimental efforts to investigate vibrationally excited molecules in their electronic ground state.

Femtosecond time-resolved coherent anti-Stokes Raman scattering (CARS) was successfully applied to liquid samples more than a decade ago.^{17–20} THz beatings between different vibrational modes of one or two species in a mixture have been detected and the fast dephasing times have been measured.^{17,18} Different contributions to vibrational relaxation in condensed phase, resonant-isotropic, resonant-anisotropic, and nonresonant, have been separately determined by proper alignment of the relative polarizations of the three laser pulses and the signal.^{19,20} Recently, fs CARS experiments have been demonstrated on gas-phase systems.^{21,22} The influence of vibrational–rotational coupling on the coherence decay in benzene and hexatriene has been demonstrated.²¹

A very elegant way to prepare a coherent superposition of vibrational states in the electronic ground state of a neutral molecule is to start with the corresponding anion and to remove the extra electron with an fs laser pulse.²³ The excess energy of this process excites a vibrational wave packet in the electronic ground state of the neutral molecule which can be interrogated by time-delayed ionization to the cation. The equilibrium geometry of silver trimers varies with its charge from linear through obtuse isosceles to equilateral in the anionic, the neutral, and the cationic state, respectively. This geometric change, induced by the two fs laser pulses, could be nicely monitored in real time.²³

Traces of electronic ground-state wave packets have also been identified in fs pump probe experiments on alkali dimers when high laser intensities were applied.^{24,25} Two photons of the pump pulse induce an absorption and simultaneous stimulated emission and in this way couple vibrational states to a coherent superposition. However, due to the identical wavelength of the involved photons, the mean vibrational level of this ground-state wave packet cannot be controlled.

Ground-state wave packets were produced by a femtosecond control experiment of a unimolecular reaction from

the transition-state region of NaI.²⁶ A first pump laser pulse induces a transition from the electronic ground state to a reactive surface in the NaI molecule. A second laser pulse could take some fraction of the dissociative system via stimulated absorption to another potential energy surface or by stimulated emission back to the ground state. A third laser pulse is used to probe the population on the reactive surface with or without perturbation of a second laser pulse.

Selective population of rovibronic states of the electronic ground state of alkali dimers was succeeded more than a decade ago by a two-color pump–dump process.^{27,28} A first ns laser pulse couples an intermediate and the final state. A slightly time-delayed ns laser pulse subsequently excites the dimer from the initial to the intermediate state. This stimulated Raman process by adiabatic passage, STIRAP, allows complete population transfer from an initial rovibronic into a final rovibronic state. The nonintuitive sequence of the laser fields in case of STIRAP can be explained by the idea of dressing the intermediate and final states by the applied dump field. This description holds if the interaction time of the light field with the molecule is much longer than its vibrational and rotational periods. If, however, the presence of the light field is shorter than the intramolecular oscillation periods, the concept of wave packets as coherent superpositions of several eigenstates is an appropriate description.

We have chosen the potassium dimer as a model system for an fs pump–dump probe experiment because its electronic and vibrational energies allow the preparation of well-localized vibrational wave packets with reasonable femtosecond laser pulses in the visible wavelength regime. Homonuclear and heteronuclear alkali dimers and trimers have benefited from the development of fs spectroscopic methods.^{29–36} For a comprehensive review on femtosecond real-time spectroscopy of small molecules and clusters, see the book recently published by E. Schreiber.³⁷ Wave packet dynamics in different electronically excited states of Na₂ were extensively studied including detailed investigations of the multiphoton ionization pathways in the probe step.^{29,30} Spin-orbit coupled electronic states of K₂ were investigated by their influence on the wave packet’s propagation with isotopomer resolution.³¹ Interferences of wave packets in Cs₂ have been generated and detected.³² Fractional revivals of wave packets due to the beating of portions of the wave packet with different periodicities were also reported in Br₂ and NaK and nicely illustrated with the help of spectrograms.^{33,34} In a previous pump–probe experiment on potassium dimers, we have shown that the electronic transition dipole moment which is responsible for the ionization probe step varies with the position of the wave packet on its potential surface.³⁵

In the present contribution, we extend our approach to a controlled excitation and interrogation of hot vibrational wave packets in the electronic ground state X¹Σ_g⁺ of potassium dimers.³⁶ We use a pump–dump scheme with two ultrashort laser pulses of different central wavelengths (Fig. 1). The first laser pulse, the pump pulse, induces a vertical transition of the molecules and creates a vibrational wave packet in the electronic B¹Π_u state. Its mean vibrational quantum number is given by the excess energy of the photon with

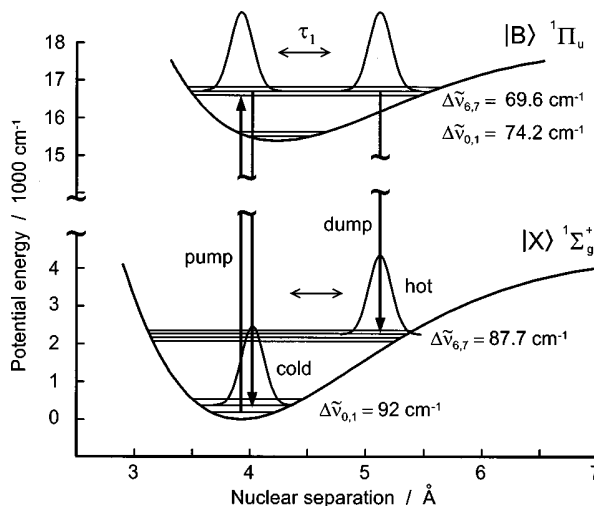


FIG. 1. Generation of the ground-state wave packets. The potassium dimers are believed to be in their electronic and vibrational ground state $X\ 1\Sigma_g^+$, $v_x=0$ before the laser pulses interact with them. The pump pulse generates a wave packet in the $B\ 1\Pi_u$ state around $\bar{v}_B=6$. The time-delayed dump pulse stimulates emission back to the X state and generates the hot ground-state wave packet around $\bar{v}_X=7$. The efficiency of this two-color pump-dump process depends on the time τ_1 between the two laser pulses. Absorption and stimulated emission within the pump pulse itself creates an additional cold X -state wave packet.

respect to the electronic transition. Due to the relative position of the equilibrium nuclear distance in the X and B potentials, the wave packet is generated at the inner branch of the B potential. The wave packet starts moving outward and oscillates in the B potential with a periodicity of about 480 fs, which is significantly longer than the laser pulse. The second laser pulse, the dump pulse, is in resonance with the transition between the intermediate state and the target vibrational states in X . The efficiency of the stimulated emission process depends on the overlap of the intermediate and final vibrational wave functions which differs along the internuclear distance coordinate. By waiting with the dump pulse for the optimal Franck–Condon window between the B -state wave packet and the target X state, we can control the population of the final quantum state. The evolution of the X -state wave packet is monitored by a time-delayed three-photon ionization process which is state-selectively enhanced by an intermediate resonant electronic state.

II. EXPERIMENT

Our experimental setup consists of three parts, a molecular beam apparatus, a three-color femtosecond laser system, and a mass selective ion detector (Fig. 2).

The molecular beam apparatus is a two-chamber vacuum system. In the oven chamber, a cartridge is filled with potassium and heated to 420°C . The temperature of the stainless steel, conical nozzle is set to 500°C to reduce the probability of clogging with potassium. The diameter of the nozzle is $100\ \mu\text{m}$. 25 mm downstream of the nozzle, a skimmer with a 1-mm opening is placed. A backing pressure of $1\text{--}5\text{ atm}$ of argon is applied to the cartridge to support the cooling of the beam and the cluster formation. The oven chamber is evacuated by a 5300 l/s oil diffusion pump to about 10^{-4} mbar .

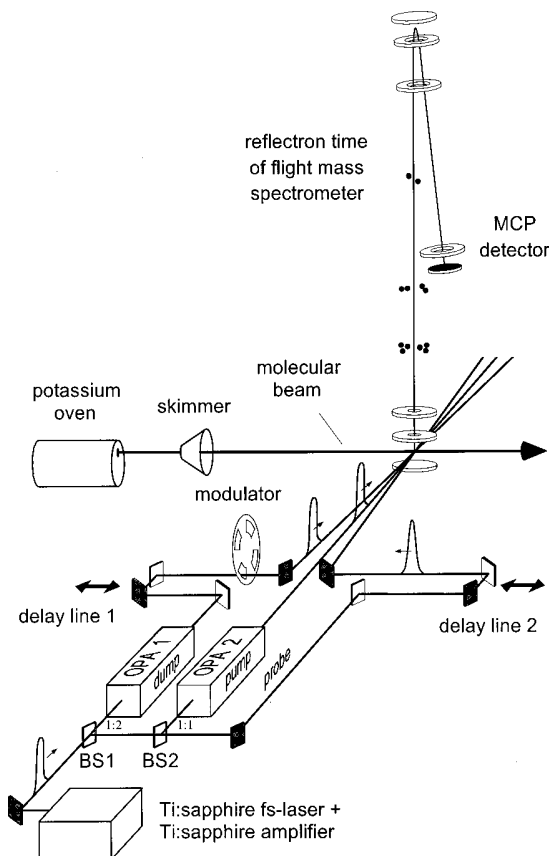


FIG. 2. Experimental setup. The potassium dimers are produced in a supersonic jet expansion through a $100\text{-}\mu\text{m}$ nozzle and a 1-mm skimmer. Pump, dump, and probe laser pulses of sub 100 fs duration and wavelengths λ_{pump} , λ_{dump} , and λ_{probe} , respectively, are generated with a regeneratively amplified Ti:sapphire laser and two optical parametric amplifiers, OPA 1 and OPA 2. Two optical delay lines control the relative timing of the pulses. The dump beam can be modulated with help of a chopper wheel. The laser pulses cross the molecular beam in the center of the acceleration state of a 1.3 m reflectron time-of-flight mass spectrometer. The microchannel plate ion detector is read out by a boxcar amplifier. The selected $^{39,39}\text{K}_2$ signal is recorded as a function of the position of delay line 2.

The heart of the molecular beam enters the experimental chamber, which is pumped by a 550 l/s turbo molecular pump down to 10^{-6} mbar . At a distance of about 150 mm from the nozzle, the laser beams cross the molecular beam.

The laser system is headed by a Ti:sapphire femtosecond laser (MIRA Coherent, Inc.) which produces pulses of a duration of 80 fs with a repetition rate of 76 MHz. Every ms, one of these pulses is coupled into an Nd:YAG-laser pumped Ti:sapphire resonator and is amplified to 1.1 mJ within 90 fs after compression (CPA-1000, Clark-MXR, Inc.). The amplified beam is split into three parts with pulse energies of 200, 450, and 450 μJ by means of two beam splitters, BS 1 and BS 2. The two more intense beams are each pumping a four-pass optical parametric amplifier, OPA 1 and OPA 2 (TOPAS, Light Conversion, Inc.). Their signal outputs are frequency doubled into the visible wavelength regime and again compressed in two prism compressors which are not shown in Fig. 2. The pulse duration was measured to be about 70 fs at the interaction point with the molecular beam.

by setting up an identical optical path outside the vacuum system. The central wavelengths can be varied independently between 500 and 730 nm. In the experiment these pulses will serve as the pump and the dump pulse. The third, slightly weaker part of the amplifier output is used as the probe pulse. Its central wavelength has been varied between 790 and 825 nm by tuning the whole Ti:sapphire laser system. All three pulses are synchronized by two optical delay lines. They are made collinear and focused onto the molecular beam by means of an $f=200$ mm lens. The energies of pump, dump, and probe pulses at the experiment were set to 100, 200, and 300 nJ, respectively, corresponding to power densities of 1–10 GW/cm².

The interaction spot of the laser pulses and the molecular beam is located in the acceleration stage of a home-built 1.3 m reflectron time-of-flight mass spectrometer with a resolution of $m/\Delta m \approx 1600$ at the mass of K₂ (see Fig. 2). The ions are detected by a microchannel plate. By means of a boxcar amplifier, the ^{39,39}K₂ ion signal is selected. After averaging typically over 500–2000 events, the ^{39,39}K₂ ion signal is recorded as a function of the delay time between the pump and the probe process. In some of the experiments, a lock-in detection scheme is applied. For reasons explained in detail in Sec. III, the dump beam was then modulated with a chopper wheel.

III. RESULTS AND DISCUSSION

The idea of the generation of ground-state wave packets by a Franck–Condon optimized two-photon process is displayed in Fig. 1. The potassium dimers are created in a supersonic jet expansion and are believed to be in their vibrational ground state of the electronic ground state X at the start of the experiment. The rotational temperature is on the order of some tens of Kelvin. The pump laser pulse, acting first on the dimers, is in resonance with the $B(\bar{v}=6) \leftarrow X(v=0)$ transition, $\lambda_{\text{pump}} = 631$ nm. Due to its bandwidth of $\Delta \tilde{\nu} \approx 200$ cm⁻¹, it creates a coherent vibrational wave packet consisting of 3–5 states. The Franck–Condon factors for these transitions are in the order of 5%.³⁸ The vibrational wave number difference between $v_B=5$ and $v_B=6$ is $\Delta \tilde{\nu}_{56} = 70.3$ cm⁻¹ and $\Delta \tilde{\nu}_{67} = 69.9$ cm⁻¹ between $v_B=6$ and $v_B=7$ (Refs. 38,39). The dynamics of this B-state wave packet and details of its detection by a one-photon ionization process are described in a former paper by us.³⁵ Since the intensity of the pump pulse is high enough to induce two-photon processes, a coherent superposition of vibrational states in the electronic ground state X can be created by absorption and stimulated emission within the pump pulse itself. This ground-state wave packet populates the lowest vibrational states $v=0,1,2$ and we therefore designate it as the cold ground-state wave packet. The vibrational spacing between ($v_X=0$) and ($v_X=1$) is $\Delta \tilde{\nu}_{01} = 92$ cm⁻¹, resulting in an oscillation period of 360 fs.

The B-state wave packet is generated at the inner branch of the potential curve. It starts evolving in time, moving outward on the potential surface. The second laser pulse, the dump pulse, induces a transition back to the electronic ground state. Its wavelength is set to $\lambda_{\text{dump}} = 661$ nm, which is in resonance with the $X(v=7) \leftarrow B(v=6)$ transition. The

mean vibrational spacing around $v_X=7$ is 87 cm⁻¹. Therefore, this so-called hot ground-state wave packet oscillates with a periodicity of 385 fs. Since the bandwidth of the two-photon transition is the convolution of the bandwidths of the two laser pulses, the hot wave packet consists of about 4 states.

Due to the different shapes of the two involved potential energy curves, the potential difference varies with the nuclear separation. Therefore, the momentum of the wave packet is conserved during the vertical transition between $\bar{v}_B=6$ and the target $\bar{v}_X=7$ only at certain nuclear separations. For the applied pump and dump wavelengths, the point of equal kinetic energies is located around 4.3 Å, which is between the starting point and the outer turning point of the B state wave packet. Consequently, the probability of a stimulated emission process should vary with the time delay τ_1 between the generation of the B-state wave packet by the pump pulse and the interaction with the dump pulse, and in particular should be large when the wave packet passes the point of equal kinetic energy.

After the interaction with the two laser pulses, the residual wave packet in the B state and the hot and cold components of the ground-state wave packet develop in time. All differ in their total energy and oscillation periods. As we are mainly interested in the hot wave packet of the electronic ground state, the interrogation procedure must select its time evolution and suppress contributions of the others. This can be achieved to some extent by a selective resonance enhancement of the ionization process, which serves as the probe at a variable time τ_2 , see Fig. 3. The ionization out of the X state is accomplished by a three-photon process; for the ionization out of B, two photons are needed. By carefully choosing the wavelength of the probe laser pulse, one can enhance the ionization probability of the hot X wave packet if its ionization path is in resonance with the (6) ¹S_g⁺ state at 25 882 cm⁻¹ after absorption of two photons at 800 nm.⁴⁰ In particular, this resonant electronic state provides a selectivity of the ionization probability with respect to the nuclear distance which is needed to follow the wave packet's motion. The ionization of the cold X wave packet is also enhanced because of several allowed states in the vicinity of (6) ¹S_g⁺, but weaker, since the potential difference does not exactly match the probe wavelength. However, the two-photon ionization path from the B-state wave packet does not reach an intermediate state and ends far in the ionization continuum. Therefore, this interrogation lacks the coordinate selectivity.

In order to further promote the detection of the hot X wave packet, in some experiments the dump pulse has been modulated. The readout of the boxcar amplifier was then locked to the modulation frequency. With this detection technique, only processes with participation of the dump laser should contribute to the signal. In particular, this is the case for the two-color pump–dump step generating the hot X wave packet and not for the one-color pump–dump process, which creates the cold X wave packet.

Figure 4 shows an example of the ion signal as a function of the time delay τ_2 between the generation of the wave packets and the probe pulse. In this case, the delay τ_1 of the dump pulse with respect to the pump pulse was set to 230 fs.

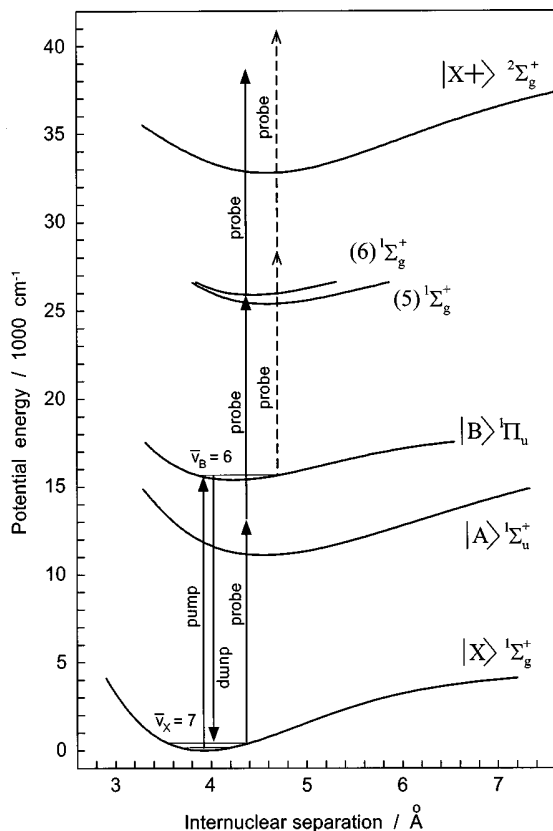


FIG. 3. Detection scheme. The hot ground-state wave packets ($X^+ \Sigma_g^+$, $\bar{v}_X = 7$) are interrogated by a three-photon ionization process which is resonance enhanced by the $(6) \Sigma_g^+$ state. Ionization of the cold X wave packet ($\bar{v}_X = 1$) is less efficient due to the not exactly fulfilled resonance condition. Detection of the $B^+ \Pi_u$ state wave packet dynamics is strongly suppressed by the lack of a coordinate selective intermediate state in the ionization path.

The signal displayed in the figure is an average over 1500 events at each time delay; the step size is 20 fs. At negative times, when the 800 nm probe pulse plays the role of the pump, two oscillations of a highly excited wave packet in the $A^+ \Sigma_u^+$ state can be seen. In the following, we will not invest-

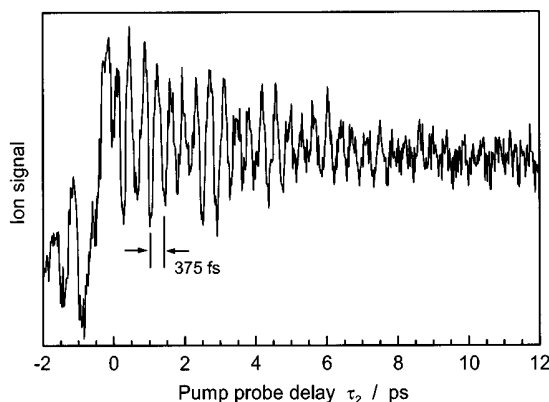


FIG. 4. $^{39,39}\text{K}_2$ ion signal as a function of pump probe delay τ_2 . The signal after $\tau_2=0$ reflects the dimer oscillation in its electronic ground state. The ground-state wave packet was generated with $\lambda_{\text{pump}}=631$ nm and $\lambda_{\text{dump}}=661$ nm and probed with $\lambda_{\text{probe}}=800$ nm. Delay time τ_1 between pump and dump process is 230 fs.

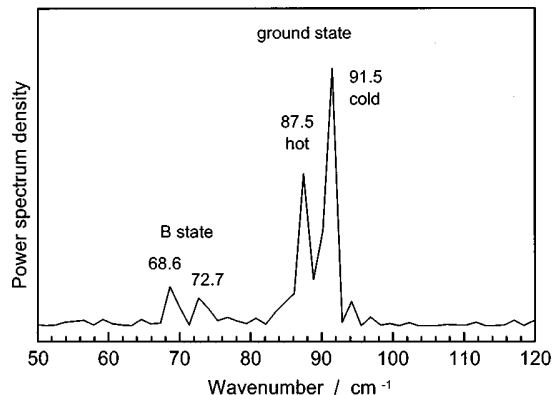


FIG. 5. Power density spectrum of the transient ion signal of Fig. 4. The spectral component at 87.5 cm^{-1} is the signature of the hot ground-state wave packet, generated by absorption of one pump laser photon and stimulated emission induced by the dump laser pulse 230 fs later. The 91.5 cm^{-1} peak reflects the cold X -state wave packet created by absorption and stimulated emission within the pump pulse itself. The two peaks at 68.6 and 72.7 cm^{-1} are the residual signals of B -state wave packets generated by the pump pulse and the high energy wing of the dump pulse, respectively.

tigate this effect in detail but rather focus on the X -state dynamics appearing after $\tau_2=0$.

At $\tau_2=0$, the ion signal raises. The exact interpretation of the first two maxima is questionable, since more than one pulse at a time interacts with the molecules during these coherence peaks. After that time, the signal oscillates with a period of about 375 fs. This ion signal oscillation is a true image of the two potassium nuclei vibrating in the electronic ground state of the dimer.

The ion signal is subjected to a fast Fourier transformation. The power density spectrum is shown in Fig. 5. Two main contributions can be identified: a ground-state wave packet appearing as a double peak around 90 cm^{-1} , and a much weaker structure around 70 cm^{-1} , the latter being a contribution of a wave packet in the B state. 91.5 cm^{-1} is the wave number difference between the vibrational states $v_X = 1$ and $v_X = 2$. Therefore, the largest peak is the signature of the wave packet created by excitation and stimulated emission within the pump pulse itself, the cold X state wave packet. Its oscillation period is 360 fs. The wave number of the second ground-state contribution of 87.5 cm^{-1} matches the wave number difference between $v_X = 6$ and $v_X = 7$, the final level of the two-color, two-photon process with pump and dump pulses. This is the image of the hot X state wave packet, the one upon which we want to focus.

The weak beating structure in the transient ion signal (Fig. 4) with minima and maxima every four to five periods originates from a residual contribution of the B -state wave packet. The Fourier component at 68.6 cm^{-1} in Fig. 5 reflects the wave packet around $\bar{v}_B = 6$. The wave packet component at 72.7 cm^{-1} is created by the high energy wing of the dump pulse. Although most of the coherent population is concentrated in this state, its signature in the spectrum is highly suppressed by the detection scheme.

The idea and goal of the experiment is to test whether the coherent population of the hot X wave packet can be controlled by changing the delay time τ_1 of the dump pro-

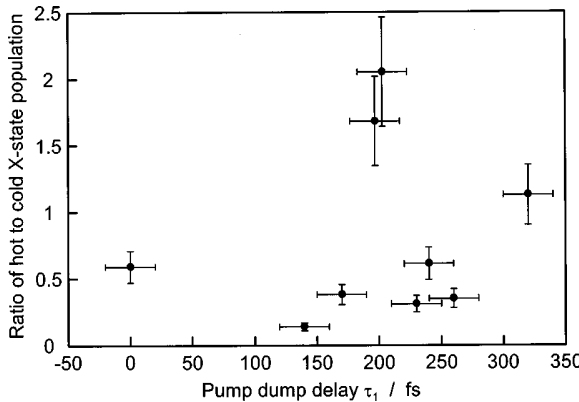


FIG. 6. Ratio of the area under the hot X wave packet signal to the area under the cold X wave packet in the power density spectra as a function of the relative population of the hot-to-cold wave packets (wavelengths as in Fig. 3: $\lambda_{\text{pump}}=631 \text{ nm}$, $\lambda_{\text{dump}}=661 \text{ nm}$, and $\lambda_{\text{probe}}=800 \text{ nm}$). The pronounced maximum around 200 fs shows that the Franck-Condon factor between the B -state wave packet and the hot X -state wave packet is peaked at the outer turning point of the B wave packet. This result confirms the possibility to control the population of vibrationally excited wave packets in the electronic ground state by variation of the pump-dump delay time during the stimulated Raman process.

cess with respect to the pump process. In other words, whether one can find the best local Franck-Condon window between the B -state wave packet and the hot X -state wave packet by adjusting τ_1 . To answer this question, we repeated the experiment for different τ_1 and calculated the power density spectrum of each of the transients. As a measure of a relative population in the hot X -state wave packet, we defined the ratio of the areas under the hot and the cold peak in the power density spectrum for every time delay τ_1 . Due to the unknown absolute ionization probabilities of the hot and the cold wave packet for the applied probe laser pulse, this number does not give the actual population ratio, but is only true within a constant factor. However, for $\tau_1 > 0$, the one-color pump-dump process into the cold wave packet is completed before the two-color process takes place. As we keep the intensities of the light fields constant for all measurements, we can use the hot-to-cold ratio as a reference value.

Figure 6 shows the ratio of the area under the hot peak and the area under the cold peak in the power density spectrum as a function of τ_1 for $\lambda_{\text{pump}}=631 \text{ nm}$ and $\lambda_{\text{dump}}=661 \text{ nm}$. At $\tau_1=0 \text{ fs}$, the two pathways into the hot wave packet with a pump and a dump photon and into the cold wave packet with two pump photons are open at the same time. Therefore, the efficiencies of both processes might influence each other, and this value is not directly comparable to the following ones. The population in the hot wave packet is small at $\tau_1=140 \text{ fs}$, rises to a maximum of about 50 fs width around 200 fs, passes through a minimum after 250 fs, and rises again at 320 fs.

The uncertainty of τ_1 is $\pm 25 \text{ fs}$. This was measured by an optical cross correlation of the pump pulse with the dump pulse just in front of the vacuum chamber, and subsequently setting delay line 1 to the desired value. The error of the hot-to-cold population ratio is more difficult to determine, mainly because the spatial overlap of the beams plays an

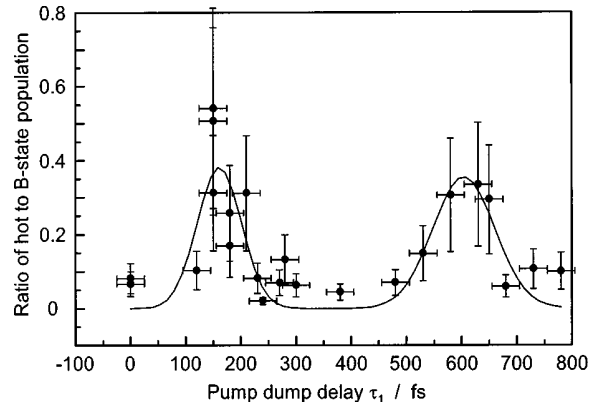


FIG. 7. Ratio of the area under the hot X wave packet signal to the area under the B -state wave packet in the power density spectra as a function of the pump-dump delay time τ_1 for a different set of wavelengths: $\lambda_{\text{pump}}=638 \text{ nm}$, $\bar{v}_B=4 \leftarrow v_X=0$; $\lambda_{\text{dump}}=685 \text{ nm}$, $\bar{v}_X=11 \leftarrow \bar{v}_B=4$; $\lambda_{\text{probe}}=805 \text{ nm}$. In this series, τ_1 was varied from 0 to 700 fs. A first maximum of the hot wave packet population appears at 220 fs, after half an oscillation of the B -state wave packet; a second maximum appears around 650 fs, after one and a half round trips in B . The solid line, added to guide the eye, is a Gaussian fit to the data with two maxima.

important role for the two-color process which generates the hot wave packet, but does not influence the one-color process responsible for the creation of the cold wave packet. Great effort was made to minimize changes in the overlap as well as in the mode structure of the laser beams and the pulse durations. From different measurements at constant τ_1 and from the sensitivity of the Fourier transform signal to the choice of the first data point, which was always set to lie in the raising edge of the transient signal, we estimate the error to be $\pm 20\%$.

The intuitive explanation of the influence of τ_1 on the population of the hot X -state wave packet is based on the motion of the B -state wave packet created by the pump pulse at time zero in the mean vibrational level $\bar{v}_B=6$ (see Fig. 1). It starts at the inner branch of the B potential and oscillates with a period of 485 fs. On its way out, the wave packet passes the point where the difference potential matches the energy of the dump pulse photons, or in other words, the momentum of the wave packet is conserved during a vertical dump process. If the dump laser pulse is fired at the corresponding delay time, the resulting population of the hot wave packet is high. The data in Fig. 6 show this time to be $\tau_1 \approx 200 \text{ fs}$. At $\tau_1 \approx 240 \text{ fs}$, when the B wave packet reaches its outer turning point, the stimulated emission process into the hot wave packet at $\bar{v}_X=7$ is small but rises again on the way back to the inner potential branch.

In Fig. 7, the result of a similar measurement with a different set of wavelengths is shown. With a pump wavelength centered at 636 nm, creating a B -state wave packet around $\bar{v}_B=4$ and a dump wavelength centered around 681 nm, the mean vibrational level of the hot ground-state wave packet is $\bar{v}_X=11$. In this case, the optimal Franck-Condon window should be at the outer turning point of the B -state wave packet. τ_1 was varied in a longer range so that the outer turning point was surpassed twice, for the first time after about half a round trip in the B state at 200 fs, for the

second time after one additional oscillation period of 450 fs at about 650 fs. The solid line represents a Gaussian fit with two maxima to summarize the information. The vertical error bars are larger for this measurement, because for this set of wavelengths the *B*-state wave packet was not suppressed by the detection scheme as well as in the former case, which introduced more uncertainty in the analysis. In particular, the hot ground-state population was normalized with the *B*-state population rather than with the cold ground-state population as above. Nevertheless, this result confirms the interpretation of the overall experiment: the generation of a vibrationally hot vibrational wave packet in the electronic ground state with the help of a resonance-enhanced stimulated Raman process can be optimized by introducing the appropriate ultrashort time delay between the pump and the dump procedure.

IV. SUMMARY

To conclude, let us collect again the essential experimental results: We start with vibrationally cold potassium dimers in their electronic ground state *X*. A first ultrashort laser pulse generates a vibrational wave packet in the electronic *B* state. This moves in time on its potential curve until its overlap with the target vibrational wave packet in *X* is large. At that time, the second ultrashort laser pulse induces stimulated emission to the final state. Its photon energy matches the potential difference at the temporary position of the wave packet.

The coherent superposition of several eigenstates to a vibrational wave packet leads to a narrow localization of the probability density with respect to the underlying individual steady-state wave functions. Hence, it introduces time as an observable. The narrow wave packet can move on the excited state potential and finds its position with the maximum overlap with the selected target of the experimentalist. At exactly that position or time, the energy is removed from the system by an ultrashort laser pulse, and the final state is achieved. This observable motion of localized wave packets on intermediate potential surfaces overcomes the concept of Franck–Condon factors as overlap integrals over the whole coordinate space, which leads to selection rules restricting transitions of the observed type. In our simple examples of this effect, we have optimized the two-photon generation of vibrational wave packets starting from $v_X=0$ to mean quantum numbers of $\bar{v}_X=7$ and $\bar{v}_X=11$. The result confirms the possibility to control the population of vibrationally excited wave packets in the electronic ground state by variation of the pump–dump delay time during the stimulated Raman process, which is, in many interesting cases, the necessary first step to control the outcome of a chemical reaction.

The freedom of choosing a vibrational target state in the electronic ground state around which the wave packet is generated is limited by the relative position of the two involved energy surfaces. This leads to the fact that the wave packet in the intermediate state can be generated with mean vibrational quantum numbers of $\bar{v}_B=1$ to $\bar{v}_B=10$. The dump process occurs near the outer turning point, so that the vibrational excited ground-state wave packet also is generated near the

outer turning point. This leads to a range of possible mean vibrational target quantum numbers of $\bar{v}_X=4$ to $\bar{v}_X=18$.

Our experiment can, in principle, be extended to larger molecules; the only restriction is that it affords relatively specific information of the intermediate state surface.

ACKNOWLEDGMENTS

The authors thank Professor V. Engel for fruitful and helpful discussions on theoretical aspects of this work. Financial support from the Deutsche Forschungsgemeinschaft (project Ki 202/11-1/11-2) is highly acknowledged. T. Chen wishes to express his thanks to the Volkswagenstiftung for a scholarship.

- ¹B. Just, J. Manz, and G. K. Paramonov, *Chem. Phys. Lett.* **193**, 429 (1991).
- ²M. V. Korolkov, J. Manz, and G. K. Paramonov, *Chem. Phys.* **217**, 341 (1997).
- ³D. J. Tannor and S. A. Rice, *J. Chem. Phys.* **83**, 5013 (1985).
- ⁴J. Manz and G. K. Paramonov, *J. Phys. Chem. A* **102**, 4271 (1998).
- ⁵M. Oppel and G. K. Paramonov, *Chem. Phys.* **232**, 111 (1998).
- ⁶A. H. Zewail, *Femtochemistry* (World Scientific, Singapore, 1994), Vols. 1 and 2.
- ⁷*Femtosecond Chemistry*, edited by J. Manz and L. Wöste (VCH, Heidelberg, 1995).
- ⁸*Femtochemistry*, edited by M. Chergui (World Scientific, Singapore, 1996).
- ⁹J. Manz, in *Femtochemistry and Femtobiology*, edited by V. Sundström (Imperial College Press, London, 1997).
- ¹⁰W. Domcke and G. Stock, *Adv. Chem. Phys.* **100**, 1 (1997).
- ¹¹A. W. Castleman, Jr., *J. Phys. Chem. A* **102**, Issue No. 23 (1998), special edition on *Femtosecond Chemistry*.
- ¹²S. Ruhman and R. Kosloff, *J. Opt. Soc. Am. B* **7**, 1748 (1990).
- ¹³R. Kosloff, A. D. Hammerich, and D. Tannor, *Phys. Rev. Lett.* **69**, 2172 (1992).
- ¹⁴B. Hartke, R. Kosloff, and S. Ruhman, *Chem. Phys. Lett.* **158**, 238 (1989).
- ¹⁵A. Bartana, U. Banin, S. Ruhman, and R. Kosloff, *Chem. Phys. Lett.* **229**, 211 (1994).
- ¹⁶U. Banin, A. Bartana, S. Ruhman, and R. Kosloff, *J. Chem. Phys.* **101**, 8461 (1994).
- ¹⁷R. Leonhardt, W. Holzapfel, W. Zinth, and W. Kaiser, *Chem. Phys. Lett.* **133**, 373 (1987).
- ¹⁸W. Zinth, R. Leonhardt, W. Holzapfel, and W. Kaiser, *IEEE J. Quantum Electron.* **24**, 455 (1988).
- ¹⁹M. Fickenscher and A. Laubereau, *J. Raman Spectrosc.* **21**, 857 (1990).
- ²⁰F. Lindnerberger, C. Rauscher, H.-G. Purucker, and A. Laubereau, *J. Raman Spectrosc.* **26**, 835 (1995).
- ²¹C. C. Hayden and D. W. Chandler, *J. Chem. Phys.* **103**, 10465 (1995).
- ²²M. Schmitt, G. Knopp, A. Materny, and W. Kiefer, *J. Phys. Chem. A* **102**, 4059 (1998).
- ²³S. Wolf, G. Sommerer, S. Rutz, E. Schreiber, T. Leisner, L. Wöste, and R. S. Berry, *Phys. Rev. Lett.* **74**, 4177 (1995).
- ²⁴T. Baumert, V. Engel, C. Meier, and G. Gerber, *Chem. Phys. Lett.* **200**, 488 (1992).
- ²⁵R. de Vivie-Riedle, K. Kobe, J. Manz, W. Meyer, B. Reischl, S. Rutz, E. Schreiber, and L. Wöste, *J. Phys. Chem.* **100**, 7789 (1996).
- ²⁶J. L. Herek, A. Materny, and A. Zewail, *Chem. Phys. Lett.* **228**, 15 (1994).
- ²⁷F. Shimizu, K. Shimizu, and H. Takuma, *Phys. Rev. A* **31**, 3132 (1985).
- ²⁸M. Becker, U. Gaubatz, and K. Bergmann, *J. Chem. Phys.* **87**, 5064 (1987).
- ²⁹T. Baumert, B. Bühl, M. Grosser, R. Thalweiser, V. Weiss, E. Wiedemann, and G. Gerber, *J. Phys. Chem.* **95**, 8103 (1991).
- ³⁰S. Rutz, S. Greschnik, E. Schreiber, and L. Wöste, *Chem. Phys. Lett.* **257**, 365 (1996).
- ³¹S. Rutz, R. de Vivie-Riedle, and E. Schreiber, *Phys. Rev. A* **54**, 306 (1996).
- ³²V. Blanchet, C. Nicole, M. A. Bouchene, and B. Girard, *Phys. Rev. Lett.* **78**, 2716 (1997).
- ³³M. J. J. Vrakking, D. M. Villeneuve, and A. Stolow, *Phys. Rev. A* **54**, R37 (1996).

J. Chem. Phys., Vol. 110, No. 19, 15 May 1999

Pausch *et al.* 9567

³⁴J. Heufelder, H. Ruppe, S. Rutz, E. Schreiber, and L. Wöste, *Chem. Phys. Lett.* **269**, 1 (1997).

³⁵H. Schwoerer, R. Pausch, M. Heid, V. Engel, and W. Kiefer, *J. Chem. Phys.* **107**, 9749 (1997).

³⁶H. Schwoerer, R. Pausch, M. Heid, and W. Kiefer, *Chem. Phys. Lett.* **285**, 240 (1998).

³⁷E. Schreiber, *Femtosecond Real-Time Spectroscopy of Small Molecules and Clusters* (Springer, Berlin, 1998).

³⁸J. Heinze, U. Schuehle, F. Engelke, and C. D. Caldwell, *J. Chem. Phys.* **87**, 45 (1987).

³⁹G. Herzberg, *Molecular Structure and Molecular Spectra* (Van Nostrand Reinhold, New York, 1950), Vol. 1.

⁴⁰J. T. Kim, C. C. Tsai, and W. C. Stwalley, *J. Mol. Spectrosc.* **171**, 200 (1995).

7.2 Wechselwirkung intensiver Laserfelder mit Materie

[8]: S. 47

Stefan Düsterer, Heinrich Schwoerer, Wolfgang Ziegler, Christian Ziener, Roland Sauerbrey;
„Optimization of EUV radiation yield from laser produced-plasma“,
Appl. Phys. B. **73**, 693-698 (2001).

[7]: S. 53

Christian Ziener, Ingo Uschmann, Heinrich Schwoerer, Christian Reich, Paul Gibbon, Thomas Feurer, Andreas Morak, Stefan Düsterer, Gregor Stobrawa, Eckard Förster, Roland Sauerbrey;
„Optimization of K_{α} bursts for photon energies between 1.7 and 7 keV produced by fs-laser produced plasmas of different scale-length“,
Phys. Rev. E **65**, 066411 (2002).

[9]: S. 61

Friederike Ewald, Heinrich Schwoerer, Roland Sauerbrey;
„ K_{α} radiation from relativistic laser-produced plasmas“,
Europhys. Lett. **60**, 710-716 (2002)

[5]: S. 68

Heinrich Schwoerer, Paul Gibbon, Stefan Düsterer, Rolf Behrens, Christian Ziener, Christian Reich, Roland Sauerbrey;
„MeV x-rays and photoneutrons from femtosecond laser produced plasmas“,
Phys. Rev. Lett. **86**, 2317-2320 (2001).

[6]: S. 72

Stefan Düsterer, Heinrich Schwoerer, Rolf Behrens, Christian Ziener, Christian Reich, Paul Gibbon, Roland Sauerbrey;
„Hard x-rays and nuclear reactions from laser produced plasmas“,
Contrib. Plasma Phys. **41**, 171-174 (2001).

S. DÜSTERER[✉]
H. SCHWOERER
W. ZIEGLER
C. ZIENER
R. SAUERBREY

Optimization of EUV radiation yield from laser-produced plasma

Institut für Optik und Quantenelektronik, Friedrich-Schiller-Universität, Max-Wien-Platz 1, 07743 Jena, Germany

Received: 16 July 2001/Revised version: 25 September 2001

Published online: 7 November 2001 • © Springer-Verlag 2001

ABSTRACT We optimize the conversion of laser energy into extreme ultraviolet (EUV) radiation by tailoring the laser parameters for a laser-produced plasma generated from 20 μm diameter water droplets. It is shown that mass-limited targets require careful adaption of laser-pulse energy and laser-pulse duration separately, rather than laser intensity, which seems to be adequate for bulk targets. The optimal pulse duration scales with the droplet radius, and the optimal pulse energy with the droplet volume. With optimized parameters, we obtain a conversion efficiency of 0.23% in 4 and 2.5% bandwidth for 13 nm radiation, the future EUV lithography light.

PACS 52.38.-r; 52.50.Jm; 85.40.Hp

1 Introduction

Computer chips will become faster and faster every year. In fact, a long-term exponential increase in operations per second has been observed since the 1970s. The underlying technological and scientific improvements cover progress in many fields, from solid-state physics and material science, improving semiconductors and photoresist, through electronics, optimizing chip design, to optics and light sources for lithographic mass production. Due to the finite velocity of signals, the final limitation of computational speed is the size of structures on the chip. Therefore the common question was, is and will be how to get the structures smaller, until they will be so small that quantum effects will limit the current concept of transistors.

One of the obvious parameters that determines the structure size is the wavelength of the light used in the lithographic process of imaging a mask onto a semiconductor wafer. The lateral and vertical resolution of structures on the wafer is governed by diffraction. Large numerical apertures of up to 0.7, sophisticated amplitude and phase masks combined with partially coherent illumination sources allow minimal lateral structure dimensions of about half of the illuminating wavelength, but not much smaller. Nowadays, excimer lasers with

wavelengths of 248 and 193 nm (KrF and ArF, respectively) are used, and optimized transmissive (lens) optics are available which allow for a minimal feature size of about 100 nm.

The step to structures well below 100 nm requires the application of light of significantly shorter wavelength: The depth of focus of the image on the wafer has to be at least 500 nm [1] in order to guarantee enough contrast of the final pattern on the wafer which is processed by etching after illumination. To overcome the contrast between a lateral resolution of 50 nm and a vertical resolution of 500 nm, one has to move to very short wavelengths and reduce the numerical aperture to a low value of about 0.1 [2].

Furthermore, the application of extreme ultraviolet (EUV) light demands the use of reflective imaging optics. It turns out that for technological reasons the wavelength is determined by the reflective optics. Multilayer mirror technology allows the production of highly reflective EUV optics ($R \approx 70\%$) only in the range of 13 nm within a spectral window of

3 Å [3]. Finally, these circumstances generate the need for a bright, powerful and efficient EUV light source at 13 nm. Beyond the strict condition of debris-free operation of such a source, the decisive parameter is the conversion efficiency.

Besides synchrotron radiation only hot plasmas from appropriate elements can act as EUV light sources. Lithium, xenon and oxygen plasmas, for example, show strong emission in the required wavelength regime. The plasma can be generated by the interaction with intense laser fields or by electrical discharges in a gaseous environment. However, neither technique has yet shown the scalability to an average output power of more than 100 W necessary for the desired throughput of a future wafer production line [1], mainly due to a relatively low efficiency for the conversion of driver energy (discharge, laser) into EUV light.

The conversion efficiency of laser light into 13 nm radiation of extended solid targets as glass or metal [4, 5] is known to be on the order of several percent. However, the unavoidable debris cannot be tolerated for an EUV lithography source, because a fair amount of the laser energy is transferred to the solid target and accelerates macroscopic particles from the surface, which quickly cover and destroy nearby optical surfaces. Still, oxidation of the mirror surface might decrease the reflectivity. The oxidation can be either due to oxygen ions expelled from the plasma or due to oxygen atoms (e.g. water

molecules in the ambient gas) adsorbed on the mirror surface which are photo-ionized by the EUV radiation and react with the surface. These are puzzling problems to be solved.

Moreover, laser plasma sources open the possibility of debris-free and long-term operation if mass-limited targets such as liquid droplets or clusters are used [6]. Several recent experiments with mass-limited water droplets have shown conversion efficiencies of only a fraction of a percent. In the experiments by the group around Hertz [7], droplet sources have been developed. Water droplets with a diameter of $10\text{ }\mu\text{m}$ were illuminated with laser pulses from a Q-switched Nd:YAG laser (700 mJ , 8 ns) [8], resulting in a conversion efficiency of only 0.01% in $4\text{ }\mu\text{m}$. However, the conversion efficiency obtained by Constantinescu et al. [9] with a similar laser (frequency-doubled Nd:YAG, 400 mJ , 10 ns) but

$20\text{ }\mu\text{m}$ droplets reached 0.1% in $4\text{ }\mu\text{m}$. Recently, Richardson et al. reported conversion efficiencies of up to 0.6% in $4\text{ }\mu\text{m}$ from larger water droplets ($60\text{ }\mu\text{m}$), again using Q-switched Nd:YAG laser [10]. According to the following discussion the different droplet sizes can account for the varying results.

We show that in the case of mass-limited targets the energy of the illuminating laser pulse and its duration are two parameters which have to be optimized independently, rather than the intensity as the quotient of energy and duration, which seems to be the appropriate parameter if extended solid targets are illuminated. Fundamental plasma-dynamics arguments support this concept:

Optimum 13 nm emission from oxygen requires ionization of all oxygen atoms in the droplet to the fifth ionization state (O^{5+} , $4d - 2p$ transition) and a plasma temperature of 30 eV . Due to the finite number of atoms in the target the energy needed can be easily calculated. Less energy would not excite all the atoms of the droplet to the required ionic state, and excess energy would be wasted in unwanted kinetic or ionic excitation.

Second, maximum absorption of laser light by the plasma requires plasma densities close to the critical density for the laser wavelength. Since the plasma expands very quickly, laser pulses that are both too short and too long play against optimum energy transfer from the laser pulse into the plasma.

Starting from this hypothesis, we report on a series of experiments measuring the conversion efficiency from laser light into 13 nm radiation with $20\text{ }\mu\text{m}$ water droplets and a solid glass target, also containing oxygen (SiO_2). We vary laser-pulse duration and laser-pulse energies, while keeping all other parameters constant. It will be shown that the discovered results may be explained quantitatively with plasma-dynamics models.

2 Experiment

In the experiments reported here the EUV radiation is emitted by a plasma, generated by an intense laser pulse (Fig. 1). 13 nm ($\hbar = 95\text{ eV}$) radiation results from the $4d - 2p$ transition of lithium-like oxygen (O^{5+}). Two different targets, each containing oxygen, are used: 2-mm-thick glass (SiO_2) and $20\text{-}\mu\text{m}$ -diameter liquid droplets. The droplets are produced by a $10\text{ }\mu\text{m}$ glass capillary nozzle, working with a backing pressure of 45 atm. The capillary is modulated with a repetition rate of 1 MHz by a piezo crystal to ensure a re-

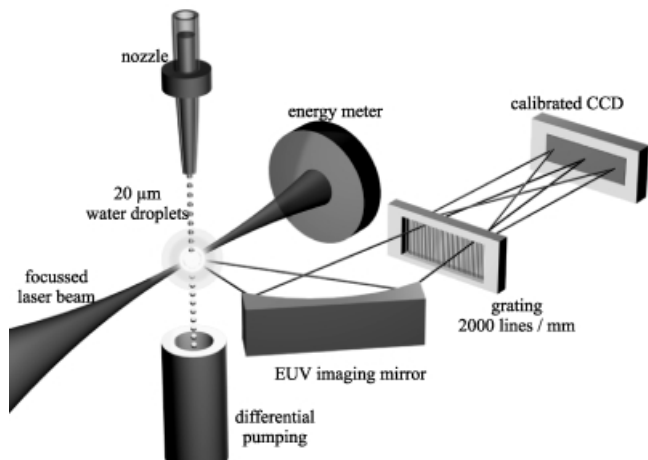


FIGURE 1 Experimental setup for 13 nm production. The EUV spectrum and the transmission of the laser were measured for each shot. The laser-pulse energy was varied from 20 to 200 mJ and the pulse duration from 200 fs to 6 ns

producible formation of a chain of $20\text{ }\mu\text{m}$ droplets [7]. The droplets are synchronized with the laser pulse. The stability and size of the droplets is measured by illuminating the droplets with a stroboscope synchronized with the laser pulses and observing them with a microscope. They do not significantly change their position in the stroboscopic image during a measurement cycle.

Since EUV radiation is strongly absorbed in air, the pressure in the interaction chamber has to be below 10^{-3} mbar to ensure less than 1% absorption of the radiation on the way to the detector. The water droplets that are not hit by the laser have to be removed from the interaction chamber by a differential pumping system. 10 mm below the nozzle the droplets enter a $200\text{-}\mu\text{m}$ -diameter capillary which is connected to an additional vacuum system that extracts the water droplets from the main chamber. To avoid that water accidentally hitting the differential pumping capillary, thus freezing and blocking the differential pumping, the capillary is heated to about $100\text{ }^{\circ}\text{C}$.

Despite this differential pumping scheme, some water molecules evaporate into the vacuum. The chamber pressure rises from $< 10^{-6}$ to $5 \times 10^{-4}\text{ mbar}$ when the water supply is turned on. Therefore 1.5×10^{14} water molecules cm^{-3} are present in the vacuum chamber. The number of water molecules in the ambient gas might be strongly reduced by using bigger pumps.

The EUV radiation is detected by a transmission-grating spectrometer equipped with a backside-illuminated CCD (Andor, 16-bit resolution) and a $2000\text{ lines mm}^{-1}$ grating. The target is imaged 1:1 onto the CCD by use of a toroidal Nickel mirror, collecting $5.9 \times 10^{-4}\text{ sr}$ of the EUV light. The grating is mounted between the mirror and the CCD and allows single-shot spectra to be taken in the 6 to 20 nm spectral range. The visible laser light is blocked by a free-standing, 200-nm -thick Zr foil positioned in front of the imaging mirror. It was experimentally verified that the Zr foil blocks the entire visible radiation but transmits 52% at 13 nm . A detailed description of the spectrometer can be found in [11].

Right before the measurements, the spectrometer-detector combination was absolutely calibrated for 10 to 15 nm radiation by the Physikalisch-Technische Bundesanstalt at BESSY II in Berlin. Therefore we report absolute EUV photon numbers and conversion efficiencies. The calculation of photon numbers assumes isotropic EUV emission. The validity of this assumption was experimentally verified. For that purpose we built a small spectrometer consisting of a 800 nm Zr foil to block the visible light and a Mo-Si multilayer mirror tuned for 13.0 nm. The 13 nm photons reflecting from the multilayer mirror are detected by a photodiode. This setup can be turned around the plasma in 5 steps in an angular region of 50° around our imaging spectrometer. The EUV emission was found to be isotropic in the measured region. In addition, measurements by Constantinescu et al. [9] support the assumption of isotropic EUV emission from droplet targets.

All measurements are performed with the Jena Multi-TeraWatt chirped pulse amplification Ti:sapphire laser. This laser provides a variable pulse duration from 6 ns down to 60 fs with up to 300 mJ per pulse at a repetition rate of 10 Hz at a center wavelength of 795 nm. The shortest laser pulses applied to the targets are about 200 fs in duration. This is due to nonlinear interactions in two glass windows which separate the EUV vacuum chamber from the laser vacuum system to prevent possible contamination of the laser system by water vapor. Pulse durations from 200 fs to 10 ps are achieved by changing the grating separation in the pulse compressor unit. The detuning of the compressor introduces a chirp to the pulse. However, the spectral width of only 17 nm (2% bandwidth at 795 nm) is not big enough to introduce any wavelength-dependent effects in the generation of a hot plasma. A pulse duration of 120 ps is achieved by bypassing the compressor unit and using the uncompressed laser pulse. The 6 ns pulse duration is generated by removing the fs oscillator from the amplifier system and running the regenerative amplifier in Q-switched mode. These modifications allowed us to measure the EUV yield dependence over almost five orders of magnitude in pulse duration with a single laser system leaving all other parameters such as focussing, laser wavelength and detection constant.

The laser is focused by a $f/2$ parabolic mirror to a $20 \mu\text{m}$ spot, the same size as the droplets, to heat the entire droplet as homogeneously as possible. The incident angle on solid and liquid targets is 0°, resulting in s-polarized laser light. The solid targets are moved after each shot to provide the same conditions for each laser pulse.

3 Results and discussion

First we report the laser-EUV conversion efficiency in absolute units from a SiO_2 bulk target with variation of either laser-pulse energy or laser-pulse duration. Figure 2 shows the conversion efficiency as a function of laser-pulse energy for two different pulse durations, namely 6 ns and 120 ps. For long laser pulses we observe a maximum in the conversion efficiency by varying the energy of the laser pulse (squares in Fig. 2), similar to results reported by Schriever et al. [12]. A maximum can be explained [13] by assuming Planckian emission for the plasma, resulting in a conversion efficiency $T^{-9/4}[\exp(\hbar c/k_B T) - 1]^{-1}$ and a tem-

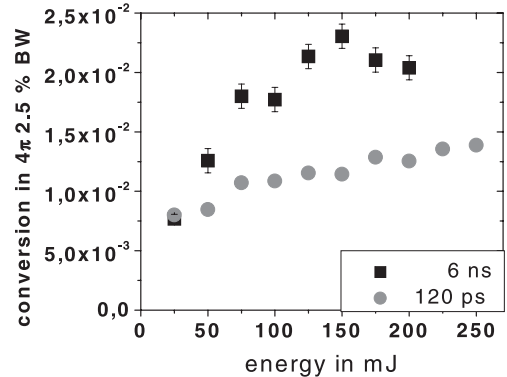


FIGURE 2 13 nm conversion efficiency for different laser energies measured for two different pulse durations. The target is a bulk glass slice

perature scaling of $k_B T \propto I_{\text{laser}}^{4/9}$, which has been experimentally verified for ns pulses [14]. Using these two equations, a maximum in the conversion efficiency is predicted. Unfortunately there are too many unknown parameters involved to calculate absolute numbers. As shown in Fig. 2, we find the maximum of 2.3% into 4π per 2.5% bandwidth at an energy of 150 mJ, corresponding to an intensity of $I_{\text{laser}} = 8 \times 10^{12} \text{ Wcm}^{-2}$. However, this simple model seems to be valid only for long laser pulses in the ns regime. It predicts a decrease in conversion efficiency for higher laser intensities. However, the measurement for a pulse duration of 120 ps shows a rising conversion efficiency in an intensity interval from $I_{\text{laser}} = 7 \times 10^{14} \text{ Wcm}^{-2}$ ($E = 20 \text{ mJ}$) to $I_{\text{laser}} = 7 \times 10^{15} \text{ Wcm}^{-2}$ ($E = 200 \text{ mJ}$) (see Fig. 2).

Figure 3 shows the conversion efficiency in absolute units as a function of laser-pulse duration from 200 fs to 6 ns. The conversion efficiency increases logarithmically over almost five orders of magnitude. Similar measurements, over a smaller pulse duration range, detecting keV radiation from laser generated plasmas also show a rise of efficiency with increasing pulse duration [15–17].

The situation changes fundamentally when targets of limited mass and volume are excited. We detect the EUV conversion efficiency from 20-μm-diameter water droplets again as a function of laser-pulse energy and laser-pulse duration. The EUV radiation again results from the same line in O^{5+} . In

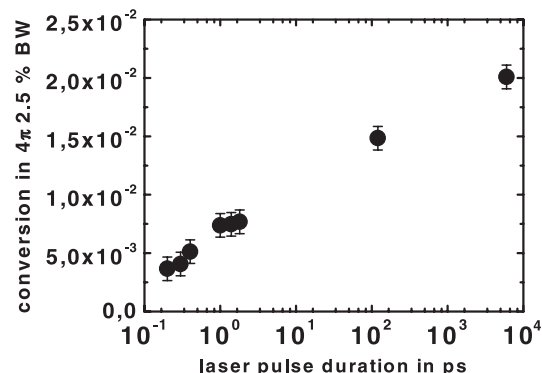


FIGURE 3 Dependence of 13 nm conversion efficiency for different laser-pulse durations but constant laser energy (250 mJ). The target is a bulk glass slice

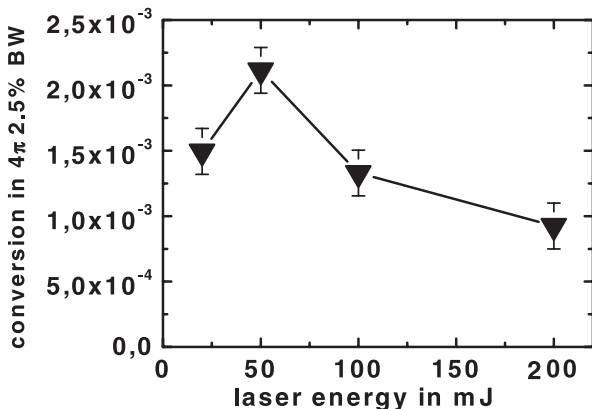


FIGURE 4 13 nm conversion efficiency for $20\text{ }\mu\text{m}$ water droplets (mass-limited target) measured for different laser energies at a pulse duration of 120 ps

Fig. 4 the conversion efficiency as a function of the laser-pulse energy is plotted for a pulse duration of 120 ps. The maximum is found at 50 mJ. For all measured pulse durations we find a similar behavior, even though the pulse duration differs by almost five orders of magnitude.

The energy responsible for optimal EUV output from a finite water droplet is essentially independent of the pulse duration. The reason is simple: for droplets the number of atoms in the interaction region of the laser is fixed in contrast to the bulk target. By assuming an equilibrium situation, we can calculate the laser energy necessary for a given droplet size to provide optimum conditions for each atom to efficiently emit 13 nm radiation: for a given water droplet diameter of $20\text{ }\mu\text{m}$, the number of molecules is 1.4×10^{14} . To ionize and excite each of the oxygen atoms in the desired ionic state 0.4 keV are needed for one atom. Furthermore, the created plasma has to be heated. Simulations, using a collisional radiative steady-state model, tell us that the optimum temperature to achieve the highest population density of the $\text{O}^{5+}(4d)$ level is around 30 eV. This is in good agreement with the simple assumption of a blackbody emitter, which predicts an optimum temperature of $k_B T = \hbar \omega_{\text{max}} / 2.8 = 34\text{ eV}$ for an emission maximum at 13 nm ($\hbar \omega_{\text{max}} = 95\text{ eV}$). Analysis of the line intensities within the detected spectral range reveals a plasma temperature between 26 and 32 eV for the optimum laser parameters of 120 ps and 50 mJ, which agrees well with the theoretical prediction. Multiplication of the temperature with the number of degrees of freedom results in 0.5 keV per molecule for the plasma heating. Therefore ionization and heating of the whole droplet to the optimum situation for 13 nm emission require about 20 mJ.

Since the absorption is always less than 100%, 20 mJ leads to a lower limit. The absorption varies between 70 and 30% for 100 ps pulses, depending on the intensity [17], and is even less for shorter pulses for the same energy [18]. Therefore, a laser-pulse energy of 30–70 mJ is needed to achieve an absorption of 20 mJ. Less energy than 30–70 mJ does not heat the plasma enough and the fraction of O^{5+} and O^{6+} , needed for 13 nm is reduced. Energy is consumed to generate O^{4+} but the ion will not contribute to the 13 nm radiation and the conversion efficiency decreases. On the other hand, for more energy per pulse the plasma is heated to higher temperatures,

giving rise to helium- and hydrogen-like oxygen, radiating soft X-rays. The conversion efficiency decreases again since energy is spent in heating that does not contribute to the 13 nm radiation.

In the region of interest, absorption of laser light by the plasma is mainly due to collisions. However, collisional absorption decreases with decreasing pulse duration (for constant energy). From this result it becomes obvious that the pulse duration is an important parameter to investigate because of its influence on the conversion efficiency (see Fig. 5). Our measurements of the conversion efficiency as function of the laser-pulse duration indicate a distinct maximum at 120 ps. The maximum of the conversion efficiency at 120 ps can be seen for each measured energy. For pulse energies not leading to optimum plasma conditions, the peak is not as distinct as for the optimum energy of 50 mJ. For short pulses up to 10 ps the conversion is a factor of three lower than for 120 ps. For longer pulses up to 6 ns again the EUV yield decreases by a factor of two. With optimized pulse duration and energy per pulse, we measure a conversion efficiency of 0.23% in 4 and 2.5% bandwidth.

The main concern with regard to long (ns) pulse durations is the expansion of the water droplet plasma during the pulse. The first part of the pulse creates and heats the plasma in the droplet. As the hot plasma starts to expand, its density decreases. The expansion velocity of the droplet may be approximated by the thermal expansion velocity, v_{exp} . For a plasma of temperature $T = 30\text{ eV}$, we find $v_{\text{exp}} = 0.4 \times 10^7\text{ cm s}^{-1}$ [19]. The model does not include instabilities and shock fronts; therefore the velocity can be taken as a lower limit. Experiments with intensities around 10^{14} W cm^{-2} show expansion velocities up to $2 \times 10^7\text{ cm s}^{-1}$ [20]. Assuming a homogeneous expansion after an expansion time, t_{crit} , of 0.2 to 2 ns, the electron density falls below the critical density of $n_{\text{crit}}(800\text{nm}) = 1.7 \times 10^{21}\text{ cm}^{-3}$ for the wavelength of the Ti:sapphire. Below n_{crit} the absorption decreases rapidly. When the expansion time t_{crit} is shorter than the laser-pulse duration itself, the trailing part of the pulse cannot be absorbed efficiently. Therefore, t_{crit} gives the longest pulse duration that can heat the plasma efficiently.

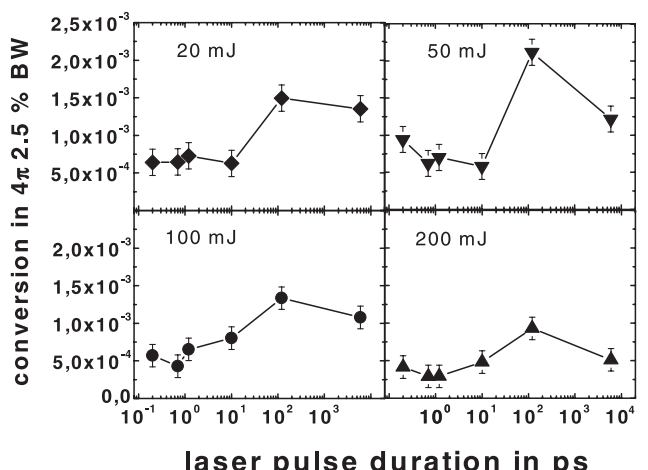


FIGURE 5 13 nm conversion efficiency for varying laser-pulse durations for the water droplet target. The conversion efficiency is plotted for different laser-pulse energies

By measuring the transmission of the laser pulse through the droplet (see below) we could experimentally verify the expansion. In addition, absorption of the EUV radiation by the expanded plasma takes place and decreases the efficiency even further. Following a similar approach Parra et al. [21] found a good agreement between the calculation and their experiment using smaller droplets (4 to 10 μm).

On the other hand, if the pulse duration becomes shorter, absorption by collisional heating becomes less and less efficient. Again the EUV conversion efficiency decreases with respect to the optimum plasma conditions. Following these considerations the best conversion efficiency is expected to be in the 0.2 to 2 ns range, in agreement with our experiments.

Summarizing the results from Fig. 4 and 5, it turns out that for mass-limited targets the optimum conversion efficiency into EUV radiation is attained if the laser-pulse energy and laser-pulse duration are separately adapted to the target. This behaviour is in contrast to that for bulk targets, where the intensity is the crucial parameter.

The best conversion efficiency for water droplets is about one order of magnitude less than the best value measured for the glass target, whereas there is only a factor 3.5 difference when we look at the conversion efficiency for glass at 120 ps and 50 mJ – the best parameters for water. The difference between mass-limited and bulk targets may be attributed to the much faster expansion of the droplet: the droplet plasma expands isotropically in three dimensions. Since the laser focus is adapted to the size of the liquid water droplets of 20 μm , matter disappears quickly from the interaction zone with the laser light, which is less important for an extended planar target, where the expansion is essentially one-dimensional. To support this picture, simulations with the MEDUSA code [22] have been performed. They show significant differences for planar-extended and spherical targets. Starting with the same plasma temperature for both targets, the spherical plasma cools faster. In addition, the position of the critical density moves slower in the spherical case. This results in a steeper plasma gradient with less particles in the region of highest absorption. For planar bulk targets more particles stay on the laser axis (weaker gradient) and can be heated more efficiently, without cooling as fast as the spherical plasma. In addition, the bulk target can always deliver fresh matter, which can be heated by the trailing edge of even a laser pulse that is several nanoseconds long. The simulation results can account for the difference of a factor of 3.5 between the two target types.

When the droplet chain was not synchronized to the laser, some of the laser pulses hit a droplet completely and others only partially or not at all. We monitored the transmission of the laser beam and simultaneously detected the EUV conversion efficiency (see Fig. 1). In Fig. 6 the EUV signal is plotted versus the transmission for two different pulse durations, 6 ns (diamonds) and 120 ps (triangles). All other transmission measurements for shorter pulse durations lay on the 120 ps curve. In the case of short pulses a high conversion efficiency can only be achieved for transmissions below 20%. The EUV signal for a 6 ns pulse duration has a significantly different behaviour: the transmission does not show small values (< 30%) at all; most of the measurements lie above 50% transmission,

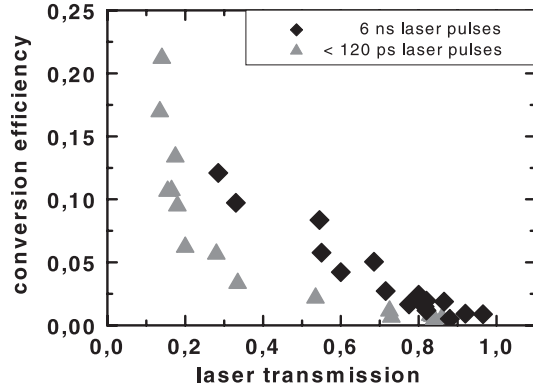


FIGURE 6 13 nm conversion efficiency as a function of the transmission of the laser energy through the droplet for two different laser-pulse durations (< 120 ps: triangles; 6 ns: diamonds) is shown

and the maximum conversion efficiency is about a factor of two smaller than that in the short-pulse situation. This is again an indication that the droplet expands during the long laser pulse so far that the trailing part of the pulse cannot be absorbed. However, with the short pulse we obtain high EUV output if and only if we hit the droplet completely. For ns pulses the EUV yield falls linearly with the transmission. Obviously an only partially hit droplet can expand during the long laser pulse into the laser focus, where it can absorb some more energy. In consequence, the conversion efficiency for long pulses stays far below the value for short, well-adapted pulses.

4 Conclusion

We have shown that there are significant differences between extended solid targets and mass-limited droplets in the conversion efficiency dependence on the laser energy and the laser-pulse duration. For the glass target the conversion efficiency increases continuously with the laser-pulse duration, whereas a maximum was found for droplets around 100 ps, which can be explained by plasma-expansion dynamics. We also found a maximum conversion efficiency for a certain laser-pulse energy for the droplet target because of the limited number of atoms in the interaction region. With optimized pulse duration and energy per pulse we obtained a conversion efficiency of 0.23% in 4 and 2.5% bandwidth. For the glass target a maximum in the conversion efficiency was only found for the ns pulse, not for shorter ones.

It was shown that for mass-limited targets such as water droplets it is important to carefully adapt the laser energy and the laser-pulse duration separately, rather than the laser intensity, which seems to be adequate for bulk targets. In general, the pulse duration scales with the droplet radius, and the pulse energy with the droplet volume. In agreement with all the other published results, the EUV conversion efficiency of droplets is significantly lower than for extended solid targets, which seems to be the price paid for debris-free operation of the EUV source. The described phenomena are based on plasma physics and not on atomic physics. Therefore, they are expected to be valid for other mass-limited target materials as well.

ACKNOWLEDGEMENTS The authors thank G. Ulm and his group at BESSY II for their support during the calibration of our spectrometer and F. Ronneberger for his assistance in running the laser system. We also acknowledge L. Veisz and D. Salzmann for their support with the simulation programs. The work was financed by the Bundesministerium für Bildung und Forschung, projects 13N7782 and 13N7925.

REFERENCES

- 1 International technology roadmap for semiconductors; available at <http://public.itrs.net/>
- 2 S.A. Lerner: Opt. Eng. **39**, 792 (2000)
- 3 R.H. Stuhlen, D.W. Sweeney: IEEE J. Quantum Electron. **QE-35**, 694 (1999)
- 4 R.C. Spitzer et al.: J. Appl. Phys. **79**, 2251 (1996)
- 5 P. Dunne et al.: Appl. Phys. Lett. **76**, 34 (2000)
- 6 M. Richardson: Opt. Commun. **145**, 109 (1998)
- 7 L. Rymell, H.M. Hertz: Opt. Commun. **103**, 105 (1993)
- 8 L. Malmqvist, L. Rymell, H.M. Hertz: OASA TOPS Extreme Ultraviolet Lithogr. **4**, 72 (1996)
- 9 R.C. Constantinescu et al.: Proc. SPIE **4146**, 101 (2000)
- 10 G. Schriever, M. Richardson, E. Turcu: Conference on Lasers and Electro-Optics, OSA: Technical Digest, (2000) pp. 393–394
- 11 J. Jasny et al.: Rev. Sci. Instrum. **65**, 1631 (1994)
- 12 G. Schriever et al.: Appl. Opt. **37**, 1243 (1998)
- 13 G. Schriever et al.: J. Appl. Phys. **83**, 4566 (1998)
- 14 H. Puel: Z. Naturforsch. **25a**, 1807 (1970)
- 15 D. Altenbernd et al.: J. Phys. B **30**, 3969 (1997)
- 16 J.N. Broughton, R. Fedosjevs: J. Appl. Phys. **74**, 3712 (1993)
- 17 C. Garban-Labaune: Phys. Rev. Lett. **48**, 1018 (1982)
- 18 D.F. Price et al.: Phys. Rev. Lett. **75**, 252 (1995)
- 19 D. Attwood: *Soft X-rays and extreme ultraviolet radiation* (Cambridge University Press, Cambridge 1999)
- 20 R. Benattar, C. Popovics: J. Appl. Phys. **54**, 609 (1983)
- 21 E. Parra et al.: Phys. Rev. E **62**, R5931 (2000)
- 22 J.P. Christiansen et al.: Comput. Phys. Commun. **7**, 271 (1974)

Optimization of $K\alpha$ bursts for photon energies between 1.7 and 7 keV produced by femtosecond-laser-produced plasmas of different scale length

Ch. Ziener,* I. Uschmann, G. Stobrawa, Ch. Reich, P. Gibbon,[†] T. Feurer,[‡] A. Morak, S. Düsterer, H. Schwoerer, E. Förster, and R. Sauerbrey

Institut für Optik und Quantenelektronik, Friedrich-Schiller-Universität Jena, Max-Wien-Platz 1, 07743 Jena, Germany

(Received 12 January 2001; revised manuscript received 20 March 2001; published 26 June 2002)

The conversion efficiency of a 90 fs high-power laser pulse focused onto a solid target into x-ray $K\alpha$ line emission was measured. By using three different elements as target material (Si, Ti, and Co), interesting candidates for fast x-ray diffraction applications were selected. The $K\alpha$ output was measured with toroidally bent crystal monochromators combined with a GaAsP Schottky diode. Optimization was performed for different laser intensities as well as for different density scale lengths of a preformed plasma. These different scale lengths were realized by prepulses of different intensities and delay times with respect to the main pulse. Whereas the $K\alpha$ yield varied by a factor of 1.8 for different laser intensities, the variation of the density scale length could provide a gain factor up to 4.6 for the $K\alpha$ output.

DOI: 10.1103/PhysRevE.65.066411

PACS number(s): 52.38.-r, 52.25.Os, 52.70.La, 41.50.+h

I. INTRODUCTION

X-ray bursts from subpicosecond-laser plasmas were discussed many years ago as a probe source to study fast processes in matter [1,2]. It has been successfully demonstrated that $K\alpha$ bursts of femtosecond-laser plasmas can be used in fast x-ray diffraction experiments to study the temporal response of x-ray diffraction from crystals [3–6]. For investigations of fast temporal processes like chemical reactions, it is essential to develop an efficient, bright x-ray source in the usual photon energy region used for structural analysis between 4 and 20 keV. This is particularly important for extending this method to a higher sensitivity and to other samples like molecules and clusters. In contrast to lasers with pulse durations of several hundred picoseconds or even nanoseconds, the focused laser intensities of current short-pulse lasers can easily reach values above 5.0×10^{17} W/cm² [7]. Such intensities are many orders of magnitude above the plasma formation threshold of a solid, and thus a plasma is created in front of the solid target. The thickness of the created plasma layer is of the order of the penetration depth of the laser radiation in the target material, which ranges from a few tens up to a few hundreds of nanometers. Since a typical plasma expansion velocity is 0.1 nm/fs, no significant hydrodynamic motion occurs during the laser pulse for pulse durations shorter than 100 fs. This means that the laser interacts with a plasma of almost solid density and the plasma density gradient is much smaller than the laser wavelength. There are different absorption mechanisms for these very high intensities. While for lower intensities the laser pulse is coupled

into the plasma mainly by collisional absorption (inverse bremsstrahlung), for the short-pulse laser interaction at higher intensities ($>10^{16}$ W/cm²) collective processes like resonance absorption or vacuum heating become more important [8–10]. A detailed theoretical analysis of the different absorption mechanism is given by Gibbon and Förster [11]. The kind of mechanism that dominates and how efficiently the laser pulse is coupled into the plasma depend mainly on the electron density gradient in front of the solid target, the so-called density scale length:

$$L = \left[\frac{1}{n_e} \left(\frac{dn_e}{dx} \right) \right]^{-1}. \quad (1)$$

More generally used is the reduced scale length $L_\lambda = L/\lambda_L$, with λ_L being the laser wavelength.

A significant amount of the absorbed laser energy can be converted to accelerated electrons with energies of up to 1 MeV [12]. These electrons lose their energy in the solid target, producing bremsstrahlung and characteristic line radiation. The conversion of laser light into x-ray line radiation ($K\alpha$) produced by hot electrons depends on the interaction of the subpicosecond laser pulse with the solid target. Such behavior has been studied experimentally for medium intensities of 4.0×10^{16} W/cm², showing that the absorption of the laser pulse, the production of the hot electrons as well as the production of the silicon $K\alpha$ line depend on the plasma scale length created by a prepulse [13]. Other influences for the conversion of a 100 fs laser pulse into $K\alpha$ radiation between 4 and 50 keV have been studied via detailed theoretical analysis by Reich *et al.* [14]. They conclude that the conversion efficiency depends on the laser intensity, i.e., there is an optimal hot electron temperature for creating efficient $K\alpha$ radiation and at the same time avoiding strong reabsorption of the radiation in the target. This analysis was performed for a fixed scale length L of $L/\lambda_L = 0.3$, $\lambda = 800$ nm.

The x-ray lines investigated in the present work were selected under the following considerations as candidates for time-resolved x-ray diffraction or other applications. The Si

*Present address: Central Laser Facility, Rutherford Appleton Laboratory, Chilton Didcot, OX11 0QX, United Kingdom. Email address: c.ziener@rl.ac.uk

[†]Present address: Forschungszentrum Jülich GmbH, Zentralinstitut für Angewandte Mathematik (ZAM), D-52425 Jülich, Germany.

[‡]Present address: Department of Chemistry, The Massachusetts Institute of Technology, Cambridge, MA 02139-4208.

$K\alpha$ line which has the longest wavelength undergoes high absorption and therefore has a small penetration depth of about $1 \mu\text{m}$ compared to $K\alpha$ lines with shorter wavelengths. This property is essential to match the small interaction depth (skin or absorption depth) of the pumping laser with the x-ray penetration depth, when, for instance, a crystalline sample is heated by a laser. Furthermore, such soft x-ray lines are standard sources for x-ray-induced photoelectron spectroscopy of surfaces. On the other hand, the Si $K\alpha$ line can only be used for a few selected crystalline materials, because the double lattice plane distance has to be greater than the wavelength in order to fulfill the Bragg condition. Therefore x-ray lines at shorter wavelengths are essential for time-resolved diffraction. To work with almost all crystalline samples a $K\alpha$ line from heavier elements like titanium or cobalt has to be used.

For the optimization of the electron energy it is important to consider that the K -shell cross section of electrons is maximal if the electron energy is about three times the binding energy of the K -shell electron. These binding energies are 1.74, 4.51, and 6.93 keV for the case of Si, Ti, and Co, respectively. This means that most of the hot electrons produced by the laser should have their energy in the range 6–28 keV. The fluorescence yield, which gives the ratio between fluorescence radiation and Auger decay processes, strongly increases with atomic number Z ($Z=14, 0.0504$; $Z=21, 0.225$; $Z=27, 0.388$) and should yield a similar $K\alpha$ conversion, despite the fact that a much higher energy is needed for K -shell excitation of high- Z elements.

In this paper we have measured the emitted photon numbers of the three $K\alpha$ lines mentioned above. The plasma scale length was modified by a laser prepulse at various delay times relative to the laser main pulse. For the Si $K\alpha$ line the conversion was measured for different main pulse intensities as well as different prepulse intensities as a function of the delay between prepulse and main pulse. For the Ti $K\alpha$ and the Co $K\alpha$ lines the intensity of the main pulse was varied, keeping the prepulse intensity fixed at its highest value.

II. EXPERIMENTAL SETUP

A schematic drawing of the main parts of the experimental setup (the prepulse unit together with the focusing and the x-ray optics) is shown in Fig. 1.

The experiment was performed with the Jena multiterawatt Ti:sapphire laser. This chirped-pulse-amplification laser system consists of an oscillator, a stretcher, a regenerative amplifier, two additional multipass amplifiers, and a vacuum compressor. The maximum energy is 1.3 J before the compressor. This leads to about 1 J after the compressor with a pulse duration of 80 fs at a repetition rate of 10 Hz. After the vacuum compressor the laser beam is guided to the target chamber inside a vacuum beamline. In the vacuum chamber the beam is focused by an off-axis parabolic mirror onto various solid targets. In our experiment we used a maximum energy of 240 mJ with a pulse duration (full width at half maximum) of 90 fs. The temporal structure of the laser pulse was measured by a third-order multishot autocorrelator with

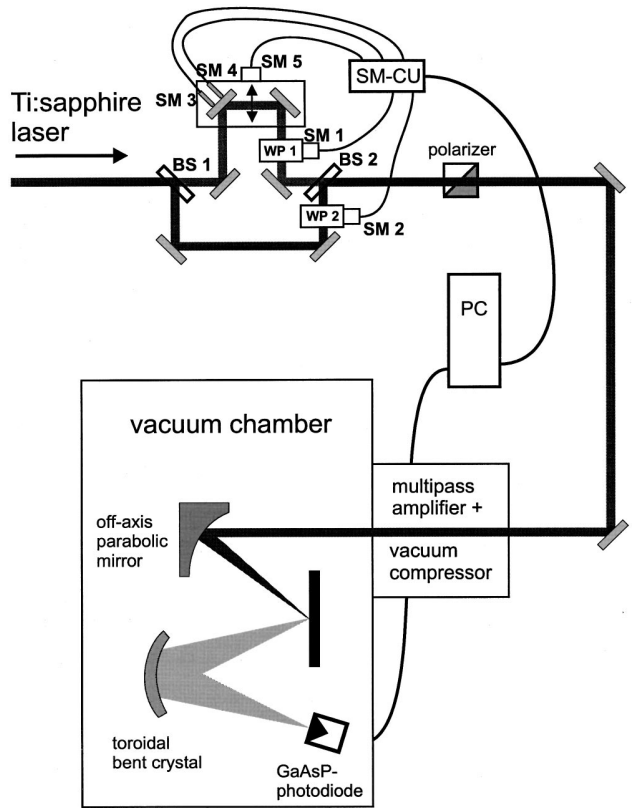


FIG. 1. Experimental setup for the measurement of the $K\alpha$ radiation, showing the unit for the generation of a defined prepulse and the focusing arrangement in the target chamber with the x-ray optics and the detector.

a dynamic range of four orders of magnitude. There are two prepulses at 4 ps and 600 fs before the main pulse, having an intensity contrast ratio of 2×10^{-4} and 5×10^{-3} , respectively. No other prepulses with a contrast ratio bigger than 10^{-4} were detected within 200 ps before the main pulse. The contrast ratio in the time domain 2 ns and more before the main pulse was measured using a fast photodiode with filters. Parasitic prepulses were measured to be less than 5×10^{-6} times the energy of the main pulse. The energy within the focal spot was measured in two steps. First the focused beam was sent through a pinhole with a diameter of $50 \mu\text{m}$ and the transmitted energy was measured. Following that a region of size $100 \times 100 \mu\text{m}^2$ around the focus was imaged onto a 16-bit charge-coupled device camera. 35% of the energy incident on the parabolic mirror was within a spot of $10 \times 12 \mu\text{m}^2$, giving an intensity of $5.0 \times 10^{17} \text{ W/cm}^2$ for a laser energy of 240 mJ.

In order to investigate the interaction of the high-intensity laser pulses with a plasma of a certain scale length, one needs an additional laser pulse to create the preplasma. For this purpose we implemented a prepulse device in our laser amplifier chain. Details of the setup are described elsewhere [15]. The prepulse device is located between the regenerative and the first multipass amplifier. The beam leaving the regenerative amplifier is split into two beams at the beam splitter

TABLE I. Important parameters of the $K\alpha$ measurement for target materials with different atomic numbers Z : crystal reflection of the toroidally bent crystals, the Bragg angle, and the integrated reflectivity.

Z	Photon energy (keV)	Crystal reflection	Bragg angle	Integrated reflectivity (μ rad)
14	1.740	Quartz (10 $\bar{1}$ 0)	56.9°	55.0
22	4.505	Silicon (311)	57.0°	28.9
27	6.930	Quartz (4040)	57.2°	11.2

(BS1) so that 90% of the energy is reflected as the main beam. Both beams are then sent through rotatable half-wave plates (WP1 and WP2) and superimposed on a second beam splitter (BS2), which is identical to the first one. The maximum energy of the prepulse is about 2% of the maximum energy of the main pulse. The plane of polarization of both beams after the first beam splitter can be adjusted by turning the respective half-wave plate by means of stepping motors (SM1 and SM2). A polarizer after the prepulse unit transmits only the part of the beam with horizontal polarization. In this way the main pulse as well as the prepulse can be attenuated by more than one order of magnitude. The energies of both pulses can be varied independently. The prepulse is sent through an optical delay line giving a temporal distance between prepulse and main pulse in the range of -350 to 100 ps with an accuracy of 6 fs. This accuracy is determined by the step size of stepping motor SM5 which drives the translation stage. A negative delay means that the prepulse arrives on target before the main pulse. To get a good spatial overlap of both focused laser beams one mirror in the optical delay line can be turned around the horizontal and vertical axes by means of two stepping motors (SM3 and SM4). The spatial overlap is automatically corrected over the whole range of the translation stage with an accuracy better than $1.5 \mu\text{m}$ if the laser beam is focused by an off-axis parabolic mirror with a focal length of 102 mm. All stepping motors are controlled by a computer by means of a stepping motor control unit (SM-CU). The programs are written in LABVIEW (National Instruments).

The $K\alpha$ radiation was selected and refocused by the Bragg reflection off toroidally bent crystals [16]. The crystals have a horizontal bending radius of 150 mm and a vertical bending radius of 106.4 mm. For silicon $K\alpha$ radiation a quartz crystal with (10 $\bar{1}$ 0) orientation was used. The same crystal but in a fourth-order reflection was used to measure cobalt $K\alpha$ radiation. For the titanium $K\alpha$ radiation a Si crystal with (311) orientation was used. For all cases the Bragg angle was between 56.8° and 57.4° . Considering the focal length in the horizontal and vertical directions and the Bragg angle, almost no astigmatism occurs for the Bragg angles used [17]. The focus size of the $K\alpha$ source produced by the bent crystals is therefore about $100 \mu\text{m}$. The x-ray detector consisted of a GaAsP Schottky photodiode protected with a $7 \mu\text{m}$ Be window [18]. The x-ray source and the photodiode were placed on the Rowland circle of the crystals. The spectral range covered by the crystal is then of the order of the $K\alpha$ linewidth. To calculate the number of photons emitted by

the source from the number of photons detected one can use the following equation [16]:

$$N_S = N_{\text{det}} \frac{4\pi}{\Omega} \frac{\Delta\lambda/\lambda}{R_i \cot \Theta_B}. \quad (2)$$

The solid angle covered by the bent crystal is Ω and $\Delta\lambda/\lambda$ is the relative $K\alpha$ linewidth. The integrated reflectivity R_i of the various bent crystals was measured with synchrotron radiation and with an x-ray tube. Table I shows the data for the crystals used in our experiment. The responsiveness of the photodiode was compared with the known quantum efficiency of a Na(Tl) J Scintillator.

Polished massive targets were used which could be moved from shot to shot to use fresh material for each shot. The incident angle of the p -polarized laser pulse was 45° . The observation angle of the crystals was about 40° .

III. RESULTS

The experimental data are presented in the following way. All measured results present the $K\alpha$ signal per laser shot as a function of the delay time between the pre- and the main laser pulse. For better statistics all measurements were repeated five times. The minimum and the maximum were removed from the analysis and the remaining three values were used to determine the mean value. The error bars in the figures are the mean error.

It is possible to determine the absolute photon number or conversion efficiency with the help of Eq. (2). The error in determining the absolute photon number is rather large (about 20%), and thus we did not do it for each experiment. Since we wanted to show the dependence of the $K\alpha$ signal on the main pulse delay, we preferred to show the diode signal with the errors explained above. In the discussion we calculated the absolute photon numbers in the case of the best conversion efficiency.

A. Prepulse intensity for the Si $K\alpha$ line

For the highest achievable main laser intensity of $5.0 \times 10^{17} \text{ W/cm}^2$ the Si $K\alpha$ line radiation was measured for four different prepulse intensities between 2.5×10^{14} and $1.0 \times 10^{16} \text{ W/cm}^2$ (Fig. 2). At the lowest prepulse intensity of $2.5 \times 10^{14} \text{ W/cm}^2$ a small maximal gain of 1.16 was measured at a time delay of -70 ps as well as at -175 ps. We define gain as the efficiency of $K\alpha$ production with a prepulse divided by the efficiency without a prepulse. Al-

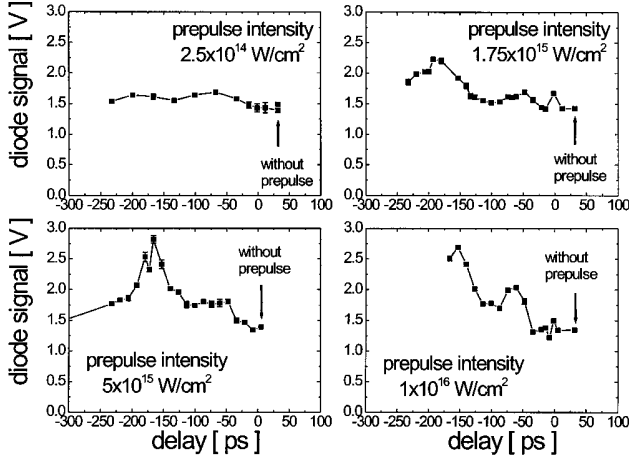


FIG. 2. $K\alpha$ signal as a function of the prepulse delay for various prepulse intensities and a main pulse intensity of $5.0 \times 10^{17} \text{ W/cm}^2$ for silicon as target material.

though the reproducibility of the measurement was very good (the error bars are smaller than the data points in the figure) this gain might not be significant. However, for higher prepulse intensities the two significant maxima are considerably enhanced. The enhancement is greater for the maximum at -175 ps than for the maximum at -70 ps . A maximum gain of 2 was measured for prepulse intensities of 5.0×10^{15} and $1.0 \times 10^{16} \text{ W/cm}^2$. Given the fact that for a decreasing prepulse intensity the output of the Si $K\alpha$ radiation could not be enhanced, the measurements for the other $K\alpha$ lines at higher photon energies were performed only for the highest prepulse intensity of $1.0 \times 10^{16} \text{ W/cm}^2$.

B. Main pulse intensity

1. Silicon $K\alpha$ (1.740 keV)

The intensity of the main pulse was varied between 1.5×10^{17} and $5.0 \times 10^{17} \text{ W/cm}^2$ by changing the laser energy. The $K\alpha$ photon numbers observed without prepulse at these different laser intensities increase by a factor of 3.7 (Fig. 3). This means that the conversion efficiency of laser energy into $K\alpha$ energy does not vary significantly. Varying the prepulse results in different changes of the $K\alpha$ line output at different main pulse intensities. For the lowest intensity of $1.5 \times 10^{17} \text{ W/cm}^2$ a slight enhancement of the Si $K\alpha$ radiation was observed if the prepulse arrives at the same time as the main pulse. This can be explained by a significant Si $K\alpha$ production of the prepulse. For a prepulse intensity of $1.0 \times 10^{16} \text{ W/cm}^2$ the fraction of laser energy of the prepulse is 7%. Increasing the delay at the lowest main pulse intensity results in a reduction of the $K\alpha$ line output down to 25% of the output without prepulse at -220 ps delay time. By contrast, a clear enhancement of the $K\alpha$ line emission was measured for larger main pulse intensities. The highest gain of about 2 was determined for the main intensity of $5.0 \times 10^{17} \text{ W/cm}^2$ at -150 ps delay time. For these parameters a maximum absolute conversion of laser energy into $K\alpha$ line radiation energy of 1.5×10^{-5} was measured. It is interesting

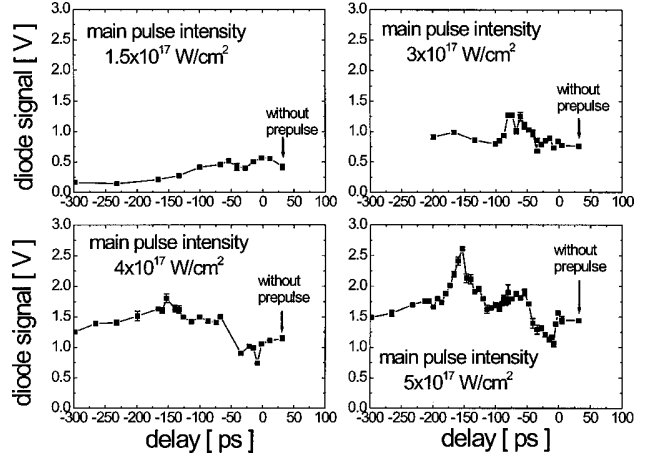


FIG. 3. $K\alpha$ signal as a function of the prepulse delay for various main pulse intensities and a prepulse intensity of $1.0 \times 10^{16} \text{ W/cm}^2$ for silicon as target material.

to see the two clear maxima at a main pulse intensity of $5.0 \times 10^{17} \text{ W/cm}^2$. There is also a clear minimum of the $K\alpha$ signal for delays around -50 ps .

2. Titanium $K\alpha$ (4.505 keV)

The main intensity was varied in the same way as for the Si $K\alpha$ measurement. Comparing the $K\alpha$ photon number observed without prepulse for laser intensities increasing by a factor of 3.3, one can see that the x-ray line output increases by a factor of 6 (see Fig. 4). Notably, for the two highest intensities the conversion efficiency of laser energy into $K\alpha$ energy increases from 5.2×10^{-6} to 8.2×10^{-6} . Again, the influence of the prepulse with an intensity of $1.0 \times 10^{16} \text{ W/cm}^2$ is much more significant for higher main pulse intensities. While no positive gain can be seen for the lowest main pulse intensity of $1.5 \times 10^{17} \text{ W/cm}^2$, a significant enhancement up to 1.9 is visible for the higher intensities. Depending on the delay between the prepulse and the

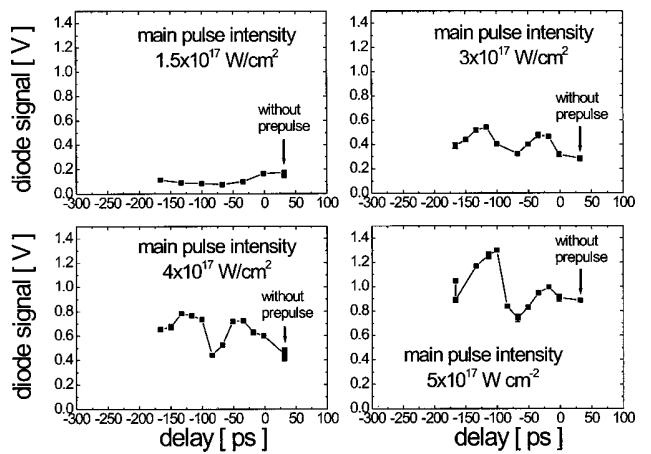


FIG. 4. $K\alpha$ signal as a function of the prepulse delay for various main pulse intensities and a prepulse intensity of $1.0 \times 10^{16} \text{ W/cm}^2$ for titanium as target material.

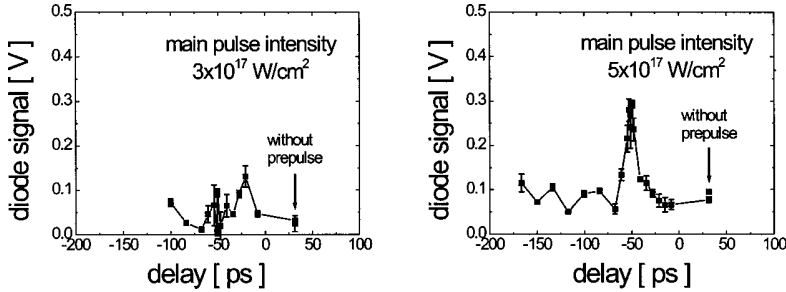


FIG. 5. $K\alpha$ signal as a function of the prepulse delay for various main pulse intensities and a prepulse intensity of $1.0 \times 10^{16} \text{ W/cm}^2$ for cobalt as target material.

main pulse, the $K\alpha$ signal shows two maxima at around -30 and -120 ps and a minimum at around -75 ps. Comparing the conversion of laser energy into $K\alpha$ energy, a maximum absolute conversion of 1.2×10^{-5} was measured for the highest main pulse intensity of $5.0 \times 10^{17} \text{ W/cm}^2$ and a prepulse delay of -100 ps.

3. Cobalt $K\alpha$ (6.930 keV)

For the Co $K\alpha$ line measurement two main pulse intensities were used with 3.0×10^{17} and $5.0 \times 10^{17} \text{ W/cm}^2$. The $K\alpha$ photon number increases by a factor of 2.9 while the laser intensity was increased only by a factor of 1.7, if no prepulse was used. Because the bremsstrahlung yield increases with Z^2 (Z being the atomic number of the element), the $K\alpha$ signal of the diode was superimposed on a continuum of x rays. To remove the influence of the bremsstrahlung background the signal was measured twice, first at the Bragg position of the $K\alpha$ line and second nearby the peak when only bremsstrahlung was reflected onto the diode. The bremsstrahlung signal comprised up to 50% of the total signal. The difference of the two signals, which is the $K\alpha$ signal, is presented in Fig. 5. A significant gain of 3.44 was measured for the higher intensity of $5.0 \times 10^{17} \text{ W/cm}^2$ at a delay time of -50 ps. Furthermore, a gain of 4.64 was determined for the intensity of $3.0 \times 10^{17} \text{ W/cm}^2$ at -25 ps delay. The maximum absolute conversion is then 0.74×10^{-5} at $5.0 \times 10^{17} \text{ W/cm}^2$ and a delay of -50 ps.

C. Discussion

It was shown in Ref. [13] that it is possible to increase the efficiency of the $K\alpha$ production of a silicon target by using an artificial prepulse some picoseconds before the main laser pulse. For longer prepulse delays the efficiency drops steadily. This behavior was explained by the dependence of resonance absorption on the electron density scale length.

Our experiments, however, show a completely different dependence of the $K\alpha$ yield on the prepulse delay. For the smallest main pulse intensity of $1.5 \times 10^{17} \text{ W/cm}^2$ there is no enhancement with an additional prepulse. For an explanation we need to know the exact temporal structure of our laser pulse and the resulting plasma scale lengths to undertake simulations of the plasma expansion and subsequent $K\alpha$ production.

We did such simulations in several steps. First, a one-dimensional particle-in-cell (PIC) code was used to determine the electron energy spectrum. As input for the PIC calculations the scale length of the electron density was ap-

proximated with an exponential decay or was calculated directly with the hydrodynamic code MEDUSA [19]. By means of a Monte Carlo transport code [20] the electron trajectories inside the target were calculated. These simulations were made by taking into consideration the $K\alpha$ ionization cross sections [21] as well as fluorescence yield, relative line intensities, and self-absorption lengths for $K\alpha$ radiation [22].

The results of the simulations are shown in Fig. 6. Parameters used were a laser energy of 240 mJ, an intensity of $5.0 \times 10^{17} \text{ W/cm}^2$, pulse length of 60 fs, and p polarization. The angle of incidence was 45° . The program package allows for the calculation of absolute photon numbers; therefore the calculated efficiency plotted in Fig. 6 is shown as $K\alpha$ photons per steradian.

One can clearly see that for all target materials the efficiency of the $K\alpha$ production is a maximum for a reduced scale length of about 0.2. A remarkable fact is that the $K\alpha$ efficiency is highest for cobalt, although the number of electrons with sufficient energy to create K -shell holes decreases with increasing $K\alpha$ energy. The increase in efficiency is due to the higher reabsorption of the $K\alpha$ radiation for smaller $K\alpha$ energies. For an intensity of $5.0 \times 10^{17} \text{ W/cm}^2$ the $K\alpha$ production is therefore least efficient for titanium and not for cobalt as expected from the pure $K\alpha$ generation. The discrepancy with our measurements will be explained in the next section.

For an estimation of the scale lengths during our experiments the inherent prepulses of our laser system are important. By means of the hydrodynamic code MEDUSA, the reduced electron density scale length was calculated after the

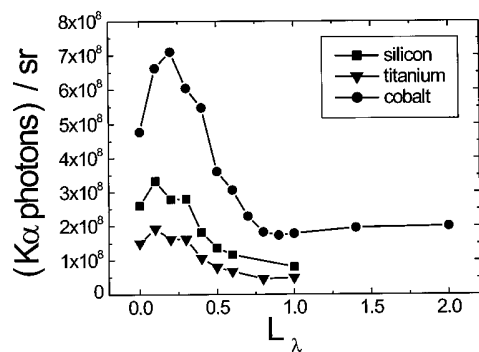


FIG. 6. Calculated absolute photon numbers as a function of the reduced electron density scale length for the three investigated target materials. Parameters are a laser energy of 240 mJ, an intensity of $5.0 \times 10^{17} \text{ W/cm}^2$, a pulse length of 60 fs, an angle of incidence of 45° , and p polarization.

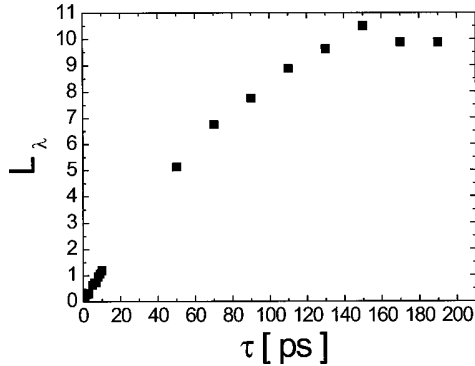


FIG. 7. Reduced electron density scale lengths for large prepulse delays, calculated with MEDUSA.

interaction of two prepulses with 1.0×10^{14} and $2.5 \times 10^{15} \text{ W/cm}^2$ and delays of -4.1 and -0.6 ps , respectively, with a solid target. The scale lengths are 0.15 for silicon, 0.11 for titanium, and 0.1 for cobalt. Compared with Fig. 6 it is evident that the prepulse structure of our laser pulse is in fact already optimal for efficient $K\alpha$ production. This one-dimensional hydrodynamic code can be used despite the relatively small focal spot diameter ($10 \mu\text{m}$), because the expansion of the plasma is for these short times much smaller than the lateral plasma diameter.

However, the increase in $K\alpha$ yield for prepulse delays of several tens of picoseconds cannot be explained by the creation of an optimal scale length for resonance absorption as shown in Fig. 7. For prepulse delays of several tens of picoseconds the scale length is more than a factor of 10 larger than the optimum predicted in Fig. 6. Due to the three-dimensional expansion of the plasma, the actual scale length might be smaller by a factor of 3, but even then the scale length would be much too large for prepulse delays in excess of 100 ps .

One possible explanation for the increase in $K\alpha$ yield for large prepulse delays is relativistic self-focusing [23], for which there is a well-known critical power P_{cr} , given by [24]

$$P_{\text{cr}} \sim 17(\omega_L/\omega_p)^2 \text{ GW}, \quad (3)$$

with ω_L the laser and ω_p the plasma frequency. That is, for a laser power of about 2.5 TW, relativistic self-focusing should be possible for electron densities 100 times smaller than the critical density, which for Ti:sapphire lasers is about $2 \times 10^{21} \text{ cm}^{-3}$.

The “self-focusing length” z_c is the distance over which the laser beam will reduce its diameter to about the laser wavelength [25,26]:

$$z_c = \frac{z_R}{(P_L/P_{\text{cr}} - 1)^{1/2}}, \quad (4)$$

with z_R being the Rayleigh length of the focused laser beam. Obviously, z_c depends on the electron density through P_{cr} . It

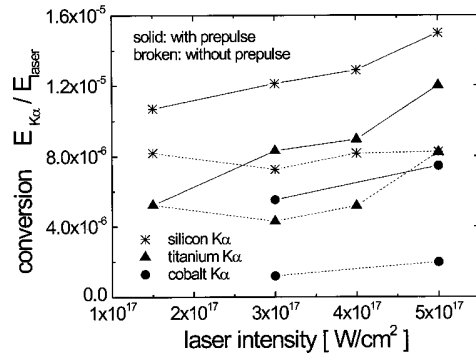


FIG. 8. Conversion efficiencies as a function of the main pulse intensity for silicon, titanium, and cobalt.

decreases with increasing electron density. In our experiments the extension of the preplasma should be large enough to enable relativistic self-focusing as demonstrated previously by Borghesi *et al.* [27]. In this paper it was shown experimentally and in simulations that, for plasma densities, scale lengths, and laser power very similar to those used in our experiment, relativistic self-focusing takes place over distances of several tens of wavelengths. There are a number of experiments in which the electron density of an expanding plasma was measured some hundreds of picoseconds [28,29] or several nanoseconds [30] after the heating prepulse. In [29] Fuchs *et al.* measured that for a prepulse intensity of $5 \times 10^{12} \text{ W/cm}^2$ the preplasma with a density above 10^{20} cm^{-3} was extended over more than $300 \mu\text{m}$ after 500 ps. These measurements show that in our case the preplasma should be extended over at least some tens of micrometers, thus allowing for relativistic self-focusing.

In the case of relativistic self-focusing the laser intensity can be amplified by at least an order of magnitude [31]. Therefore the resulting ponderomotive steepening of the electron density profile [32] would be much higher than in the “normal” case and the coupling of the laser light into the plasma is enhanced at the critical density. Also possible is acceleration of additional electrons within the relativistic

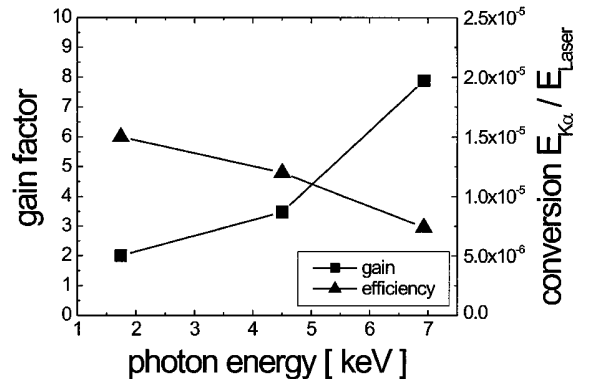


FIG. 9. Potential increase of the $K\alpha$ yield due to an artificial prepulse and optimized laser intensity and the maximum absolute conversion efficiency from laser-into- $K\alpha$ energy for different $K\alpha$ lines (target materials).

channel in the underdense plasma [33], which would also be capable of producing $K\alpha$ radiation.

IV. CONCLUSION

We investigated the efficiency of the production of $K\alpha$ radiation as a function of prepulse delay and main pulse intensity for three different target materials or $K\alpha$ energies.

If the main pulse laser intensity was increased without using a prepulse the conversion $E_{K\alpha}/E_{\text{laser}}$ did increase for titanium and cobalt but not for silicon (Fig. 8). This agrees qualitatively with the results of Eder *et al.* [34] and with the model proposed by Reich *et al.* [14], who both found an optimal intensity for $K\alpha$ production. In our experiment the optimal intensity is probably reached for silicon, not for titanium and cobalt. The reason that the intensity proposed in [14] is smaller than the one measured by us can be explained by the intensity distribution in the present experiment. Only 50% of the laser energy is focused within the focal spot, the remaining part is focused to a lower intensity but over a larger area, producing lower-energy electrons. This might also explain the fact that the conversion efficiency is highest

for silicon and not for cobalt as predicted by the simulations in the previous section.

Comparing the gain curves and the conversion efficiencies produced with a prepulse for the three different $K\alpha$ lines, a clear enhancement is visible for all elements investigated. The maximum gain was determined for Co with 4.6, for Ti with 1.9, and for Si with 1.8. At the laser intensities used the maximum gain seems to be more significant for higher photon energies. Considering both effects, the higher conversion efficiency induced by the optimized main pulse laser intensity and the gain due to the scale length variation, a maximum gain of 7.8 was measured for Co $K\alpha$. Comparing the maximal conversion $E_{K\alpha}/E_{\text{laser}}$ for the different $K\alpha$ energies, its value decreases for higher-Z elements by a factor of 2 (Fig. 9). Comparing the gain curves of the different $K\alpha$ energies, the time delay for the maximum gain is shifted toward shorter delays between prepulse and main pulse for elements with a larger Z. In summary, for higher-Z elements the conversion decreases but the optimization by main pulse intensity and scale length variation becomes much more important (Fig. 9).

- [1] M. M. Murnane, H. C. Kapteyn, M. D. Rosen, and R. W. Falcone, *Science* **251**, 531 (1991).
- [2] C. P. J. Barty, J. Che, T. Guo, B. Kohler, C. Le Blanc, M. Messina, F. Ráski, C. Rose-Petruck, J. A. Squier, K. Wilson, V. V. Yakovlev, and K. Yamakawa, *Proc. Photochem.* **30**, 531 (1995).
- [3] C. Rischel, A. Rousse, I. Uschmann, P.-A. Albouy, J.-P. Geindre, P. Audebert, J.-C. Gauthier, E. Förster, J.-L. Martin, and A. Antonetti, *Nature (London)* **390**, 490 (1997).
- [4] C. Rose-Petruck, R. Jimenez, T. Guo, A. Cavalleri, C. W. Siders, F. Raksi, J. A. Squier, B. C. Walker, K. R. Wilson, and C. P. J. Barty, *Nature (London)* **398**, 310 (1998).
- [5] C. W. Siders, K. Sokolowski-Tinten, Cs. Toth, T. Guo, M. Kammler, M. Horn van Hoegen, K. R. Wilson, D. von der Linde, and C. P. J. Barty, *Science* **286**, 1340 (1999).
- [6] I. Uschmann, E. Förster, P. Gibbon, C. Reich, T. Feurer, A. Morak, R. Sauerbrey, A. Rousse, P. Audebert, J.-P. Geindre, and J.-C. Gauthier (unpublished).
- [7] S. Backus, C. G. Durfee III, M. M. Murnane, and H. C. Kapteyn, *Rev. Sci. Instrum.* **69**, 1207 (1998).
- [8] F. Brunel, *Phys. Rev. Lett.* **59**, 52 (1987).
- [9] P. Gibbon and A. R. Bell, *Phys. Rev. Lett.* **68**, 1535 (1992).
- [10] U. Teubner, J. Bergmann, B. van Wonterghem, F. P. Schäfer, and R. Sauerbrey, *Phys. Rev. Lett.* **70**, 794 (1993).
- [11] P. Gibbon and E. Förster, *Plasma Phys. Controlled Fusion* **38**, 769 (1996).
- [12] J. D. Kmetec, C. L. Gordon, J. J. Macklin, B. E. Lemoff, S. G. Brown, and S. E. Harris, *Phys. Rev. Lett.* **68**, 1527 (1992).
- [13] S. Bastiani, A. Rousse, J. P. Geindre, P. Audebert, C. Quoil, G. Hamiaux, A. Antonetti, and J. C. Gauthier, *Phys. Rev. E* **56**, 7179 (1997).
- [14] C. Reich, P. Gibbon, I. Uschmann, and E. Förster, *Phys. Rev. Lett.* **84**, 4846 (2000).
- [15] C. Ziener, G. Stobrawa, H. Schwoerer, I. Uschmann, and R. Sauerbrey, *Rev. Sci. Instrum.* **71**, 3313 (2000).
- [16] T. Missalla, I. Uschmann, E. Förster, G. Jenke, and D. von der Linde, *Rev. Sci. Instrum.* **70**, 1288 (1999).
- [17] E. Förster, K. Gabel, and I. Uschmann, *Laser Part. Beams* **9**, 135 (1991).
- [18] M. Krumrey, E. Tegeler, J. Barth, M. Krisch, F. Schafers, and R. Wolf, *Appl. Opt.* **27**, 4336 (1988).
- [19] J. P. Christiansen, D. E. T. F. Ashby, and K. V. Roberts, *Comput. Phys. Commun.* **7**, 271 (1974).
- [20] D. C. Joy, *Monte Carlo Modeling for Electron Microscopy and Microanalysis* (Oxford University Press, Oxford, 1995).
- [21] E. Casnati, A. Tartari, and C. Baraldi, *J. Phys. B* **15**, 155 (1982).
- [22] G. Zschornack, *Atomdaten für die Röntgenspektralanalyse* (Deutscher Verlag für Grundstoffindustrie, Leipzig, 1989).
- [23] A. B. Borisov, A. V. Borovskiy, V. V. Korobkin, A. M. Prokhorov, O. B. Shiryaev, X. M. Shi, T. S. Luk, A. McPhereson, J. C. Solem, K. Boyer, and C. K. Rhodes, *Phys. Rev. Lett.* **68**, 2309 (1992).
- [24] E. Esarey, P. Sprangle, J. Krall, and A. Ting, *IEEE J. Quantum Electron.* **33**, 1879 (1997).
- [25] Y. R. Shen, *The Principles of Nonlinear Optics* (Wiley, New York, 1984).
- [26] C. J. McKinstrie and D. A. Russell, *Phys. Rev. Lett.* **61**, 2929 (1988).
- [27] M. Borghesi, A. J. MacKinnon, L. Barringer, R. Gaillard, L. A. Gissi, C. Meyer, O. Willi, A. Pukhov, and J. Meyer-ter-Vehn, *Phys. Rev. Lett.* **78**, 879 (1997).
- [28] A. J. MacKinnon, M. Borghesi, S. Hatchett, M. H. Key, P. K. Patel, H. Campbell, A. Schiavi, R. Snavely, S. C. Wilks, and O. Willi, *Phys. Rev. Lett.* **86**, 1769 (2001).
- [29] J. Fuchs, G. Malka, J. C. Adam, F. Amiranoff, S. D. Baton,

- N. Blanchot, A. Heron, G. Laval, J. L. Miquel, P. Mora, H. Pepin, and C. Rousseaux, Phys. Rev. Lett. **80**, 1658 (1998).
- [30] A. Giulietti, A. Macchi, E. Schifano, V. Biancalana, C. Danson, D. Giulietti, L. A. Gizzi, and O. Willi, Phys. Rev. E **59**, 1038 (1999).
- [31] A. Pukhov and J. Meyer-ter-Vehn, Phys. Rev. Lett. **76**, 3975 (1996).
- [32] W. L. Kruer, *The Physics of Laser Plasma Interactions* (Addison-Wesley, New York, 1988).
- [33] C. Gahn, G. D. Tsakiris, A. Pukhov, J. Meyer-ter-Vehn, G. Pretzler, P. Thirolf, D. Habs, and K. J. Witte, Phys. Rev. Lett. **83**, 4772 (1999).
- [34] D. C. Eder, G. Pretzler, E. Fill, K. Eidmann, and A. Saemann, Appl. Phys. B: Lasers Opt. **70**, 211 (2000).

K_{α} -radiation from relativistic laser-produced plasmas

F. EWALD(*), H. SCHWOERER and R. SAUERBREY

*Institut für Optik und Quantenelektronik, Friedrich-Schiller-Universität
Max-Wien-Platz 1, 07743 Jena, Germany*

(received 19 July 2002; accepted in final form 24 September 2002)

PACS. 52.38.Ph – X-ray, γ -ray and particle generation.

PACS. 52.27.Ny – Relativistic plasmas.

Abstract. – We present systematic investigations on the generation of titanium K_{α} -radiation ($E = 4.5$ keV) from plasmas produced with ultrashort, high-intensity laser pulses. A maximum K_{α} -yield appears at a laser intensity of about $3 \cdot 10^{17} \text{ W/cm}^2$, corresponding to a plasma electron temperature of a few times the K_{α} photon energy. We observe a second increase in the K_{α} -emission yield at intensities higher than a few times 10^{18} W/cm^2 , due to the increase in the K -shell ionization cross-section for relativistic electrons. The intensity dependence of the K_{α} -yield is modeled by an analytical expression, only including cross-section, pathlength and electron energy distribution.

Introduction. – Plasmas which are generated by the interaction of ultrashort and ultraintense laser pulses with solid matter are efficient sources of relativistic electrons and of X-ray radiation with exceptional brightness. The primary process which leads to X-ray generation is the acceleration of plasma electrons in the ponderomotive potential of the intense light field. At intensities of $\geq 10^{19} \text{ W/cm}^2$ which are now accessible by state-of-the-art tabletop laser systems, the characteristic temperature of the electron distribution is in the order of several MeV [1, 2]. The duration of this electron pulse is in the order of the laser pulse duration, *i.e.* typically less than 100 fs. These laser-accelerated electrons penetrate the solid target material where they generate bremsstrahlung with photon energies up to many MeV as well as line radiation from atoms. Inner shell recombination takes place on a time scale of femtoseconds or even attoseconds. Consequently, the duration of inner shell radiation, namely K_{α} -radiation, is limited by the laser pulse duration and propagation effects [3]. Due to the small source size of about $50 \mu\text{m}$ in diameter [4] these laser-produced K_{α} -sources can be as bright as the largest undulators at photon energies of several keV despite the isotropic emission. This qualifies them as light sources for femtosecond time-resolved X-ray diffraction experiments and for first experiments towards nonlinear X-ray optics.

Measurements of K_{α} -radiation from ps-laser-produced plasmas were presented as early as 1979 by Hares *et al.* [5], and an efficient K_{α} X-ray source from fs-laser-produced plasmas is described by Rousse *et al.* [6]. A systematic investigation of the intensity dependence of the K_{α} -yield has recently been performed by Eder *et al.* [4]. It turned out that the yield peaks at a cer-

(*) E-mail: ewald@ioq.uni-jena.de

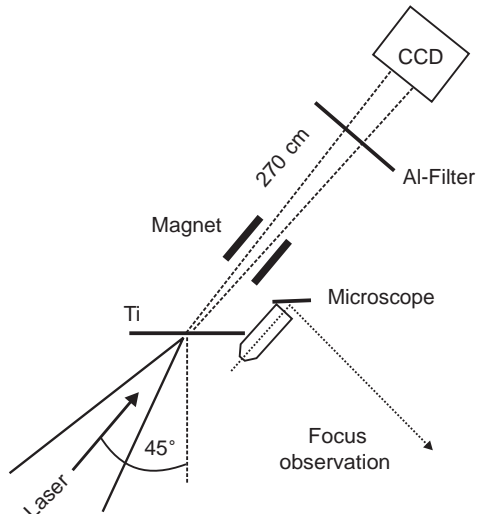


Fig. 1

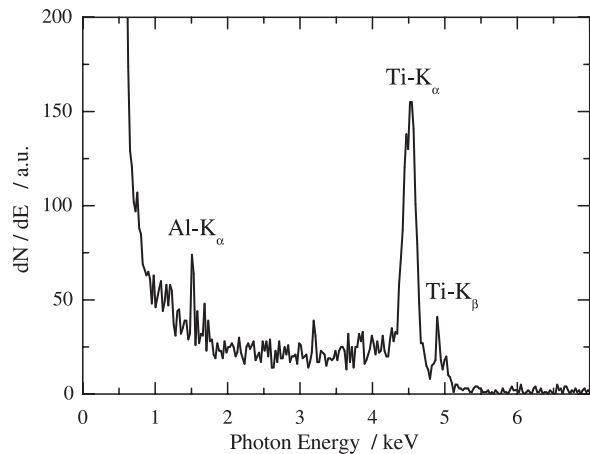


Fig. 2

Fig. 1 – Experimental setup: A 12 μm thick titanium foil is irradiated by the intense laser pulse under an angle of incidence of 45°. The intensity is determined by measuring the beam size on the target by means of a microscope. The K_{α} -yield is measured with a CCD camera in the single-photon counting mode, located 270 cm apart from the target. The camera is protected from charged particles by a magnet and from visible light by a thin metal filter.

Fig. 2 – Spectrum of the laser-produced K -shell emission of titanium. The background signal on the low-energy side of the K_{α} -line originates from multipixel events on the CCD camera and is taken into account in the analysis.

tain laser intensity, corresponding to an optimum electron temperature. From classical cross-section arguments it follows that this optimum electron temperature should be a few times the K_{α} absorption edge. Even though no absolute laser intensities are given in ref. [4], the experimental data support this simple model. Reich *et al.* [7] calculate the yield of short-pulse laser-generated K_{α} -pulses by means of Monte Carlo and particle-in-cell simulations. They explain the existence of an optimum laser intensity for the K_{α} -yield as equilibrium between K_{α} -production and reabsorption in bulk targets. This approach does not include electron energies above $U_0 = E_0/E_K \approx 20$ in the calculation of the K_{α} -yield (with E_0 the incident electron energy, E_K the ionization energy of the K -shell, $E_K = 4.96 \text{ keV}$ for titanium), since faster electrons deposit their energy deeper in the target than the absorption length of K_{α} -radiation.

However, it is known since the early seventies that the cross-section for K -shell ionization by electrons increases at relativistic electron energies [8, 9]. Since cross-section data for many medium- Z elements are well known between ionization energy and hundreds of MeV [10], the dependence of the laser-produced K_{α} -yield on the laser intensity may be a test of the electron energy distribution in the relativistic laser-produced plasma.

In this work we investigate the generation of titanium K_{α} -radiation from a relativistic laser-produced plasma. The radiation yield is measured as it depends on the laser intensity. An analytical expression is presented, which models the experimental results with regard to the interaction of relativistic electrons with the solid target.

Experiment. – For these measurements the 10 Hz Ti:sapphire laser system in Jena was operated with 300 mJ pulses of 80 fs duration at a center wavelength of 800 nm. The laser beam was focused with a $f/2$ parabola onto a 12 μm thick titanium foil with an angle of incidence of 45° and parallel polarization (fig. 1). One prepulse at 600 fs with a contrast ratio of $5 \cdot 10^{-4}$ with

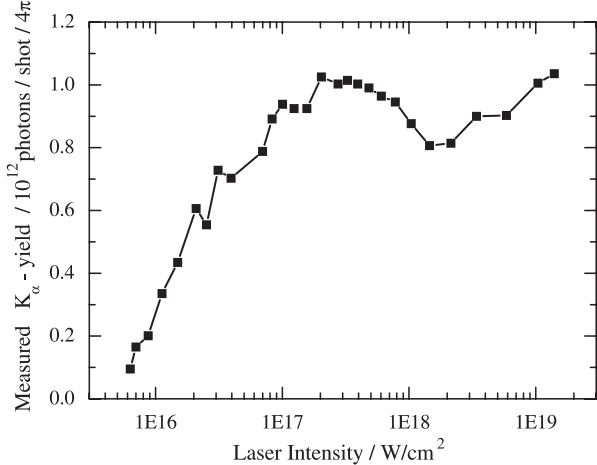


Fig. 3

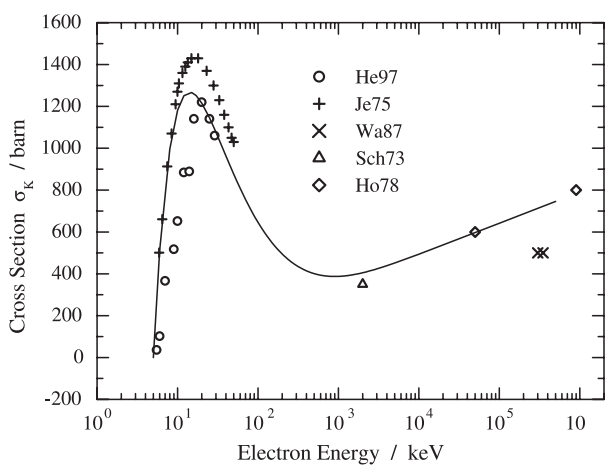


Fig. 4

Fig. 3 – Experimental Ti K_{α} -yield from a laser-generated plasma as it depends on the laser intensity.

Fig. 4 – Cross-section σ_K for the K -shell ionization of titanium by electron impact. The data points are experimental values from different sources, collected in [10]. The solid line represents the theoretical cross-section given by eq. (3).

respect to the main laser pulse is known. No further prepulses at other times are measurable within a relative intensity of 10^{-5} . The laser intensity on the target was changed by moving the foil along the beam direction, while the beam size on the target could be controlled by means of a microscope combined with a CCD camera. Thus the intensity could be varied between $2 \cdot 10^{16} \text{ W/cm}^2$ and $2 \cdot 10^{19} \text{ W/cm}^2$ by adjusting the focal beam size and keeping the total amount of energy constant. The highest intensity reached was $2 \cdot 10^{19} \text{ W/cm}^2$, within the $1/e$ -area ($7 \mu\text{m}^2$) of the best focus. The error of the measured laser intensity was within 15% for the best focus, *i.e.* the highest intensity; for lower intensities the error increased up to 50% because the beam profile becomes slightly worse at far distances from the focus position.

The X-ray radiation was detected with appropriate energy resolution using a CCD camera in the single photon counting mode. The CCD array consists of 256×1024 pixels. Each of these pixels represents a small Si-detector with its signal being proportional to the deposited photon energy. If at maximum one photon per pixel is detected, a histogram of the energy deposited in all pixels represents the incident spectrum. To avoid any pile-up problems due to summation of the energy of more than one photon within one pixel, we reduced the flux to less than about one photon per 10 pixels. Therefore the camera was located 270 cm apart from the X-ray source and aluminium filters were used to protect the CCD from low-energy bremsstrahlung and from visible light. Strong magnets prevented charged particles from hitting the detector (fig. 1). After subtraction of a bremsstrahlung background, one obtains single-shot spectra as shown in fig. 2 with the well-resolved K_{α} - and K_{β} -lines at 4510 eV and 4930 eV, respectively. The line at 1487 eV is due to aluminium K_{α} -radiation, generated in the Al-filter by bremsstrahlung photons. The absolute Ti K_{α} -emission yield was derived by integrating the number of K_{α} -photons registered by the CCD and calculating the total yield per laser shot in 4π , considering filter transmission and quantum efficiency of the CCD. The quantum yield of the CCD was measured separately with titanium K_{α} -fluorescence excited by a conventional tungsten X-ray tube.

Results. – Figure 3 shows the K_{α} -emission from a laser-produced titanium plasma as it depends on the laser intensity. The K_{α} -yield is plotted in number of photons per laser shot into

full solid angle. Beginning with low intensities, the K_{α} -emission increases steadily with laser intensity and shows a maximum at $3 \cdot 10^{17} \text{ W/cm}^2$. The maximum K_{α} -yield is 10^{12} photons per shot. With still rising laser intensity the K_{α} -signal decreases again and reaches a minimum at about 10^{18} W/cm^2 . This behaviour is already known and has been presented for laser-produced Cu- K_{α} -radiation, but without an absolute intensity scaling [4]. At intensities above 10^{18} W/cm^2 however, a second increase up to the maximum yield of K_{α} -photons of, again, 10^{12} photons per laser shot at $2 \cdot 10^{19} \text{ W/cm}^2$ is found, which has not been observed earlier.

The experimental accuracy is mainly determined by the error of the CCD sensitivity and the shot-to-shot variations in laser intensity. The statistical and absolute errors in the K_{α} -yield are determined to be $< 10\%$ and 50% , respectively.

For different emission angles, the intensity dependence has been measured and no anisotropy in the K_{α} -signal was observed. Between all four directions examined, target normal (0°), specular (-45° with respect to target normal), in laser direction (225°) and 135° , no significant deviations either in the qualitative behaviour of the characteristic intensity dependence, or in the absolute K_{α} -yield was found.

Interpretation and modeling of K_{α} -production. – We calculate the K_{α} -yield involving a relativistic energy distribution $f(U_0, T)$ of the electrons and the relativistically correct K -ionization cross-section σ_K for electron impact. Additionally, we take into account the energy-dependent path length of the electrons in a target of finite thickness. The number of K_{α} -photons produced in a titanium foil with a density of atoms n_{Ti} and the fluorescence quantum yield η of the K -transition is given by

$$d^2N_{\alpha} = \eta n_{\text{Ti}} N_e f(U_0, T) \sigma_K(U_0) dx dU_0. \quad (1)$$

N_e is the number of laser-accelerated electrons incident on the target. Their energy distribution $f(U_0, T)$ is assumed to be a 3-dimensional relativistically correct normalized distribution function. With the relativistic energy $\varepsilon(\mathbf{p})$ and a normalization factor N , it follows from $f(\mathbf{p}) = N \cdot \exp[-\varepsilon(\mathbf{p})/T]$:

$$f(U_0, T) dU_0 = \frac{e^{-1/\alpha T}}{TK_2(1/\alpha T)} e^{-U_0/T} (1 + \alpha U_0) \sqrt{(1 + \alpha U_0)^2 - 1} dU_0, \quad (2)$$

wherein $K_2(1/\alpha T)$ is the modified Bessel function of second order, $T = k_B T_e / E_K$ (T_e the electron temperature) and $\alpha = E_K / m_0 c^2$. In the low-temperature limit, for $T \ll m_0 c^2$ this distribution becomes the classically correct Maxwellian velocity distribution. $f(U_0, T) dU_0$ may also be derived in the general framework of relativistic thermodynamics [11]. This distribution function assumes that electrons enter the target isotropically, which is an adequate assumption for weakly relativistic electrons up to a few MeV as has been verified by experiments [2]. As K -ionization cross-section σ_K we use a semiempirical expression derived by Quarles *et al.* [12], based on the Bethe theory of ionization [13] corrected for relativistic electron energies:

$$\sigma_K(U_0) = 828 \cdot 10^{-16} \frac{R}{E_K^2} \frac{\ln U_0}{U_0} \text{ cm}^2 \text{ eV}^2. \quad (3)$$

Figure 4 shows a collection of measured K -ionization cross-section data compared to eq. (3). The cross-section yields its maximum at about four times the ionization edge ($U_0 \approx 4$). In a nonrelativistic treatment the cross-section would decrease for higher electron energies. The relativistic correction factor R in eq. (3) behaves as $R \approx 1$ for small U_0 and $\alpha \ll 1$ and as $R \sim U_0$ for $U_0 \gg 1$. It therefore reproduces the logarithmic increase of the cross-section for relativistic electrons.

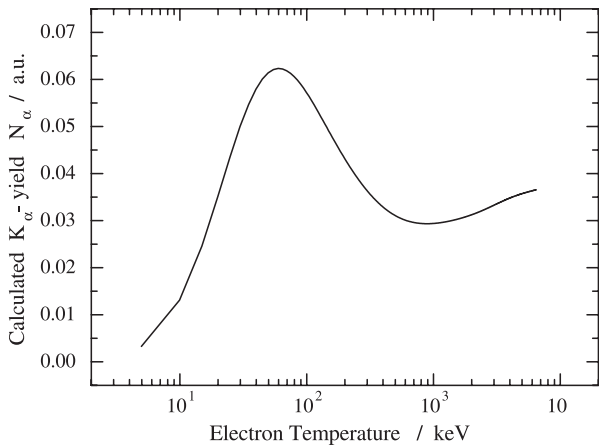


Fig. 5

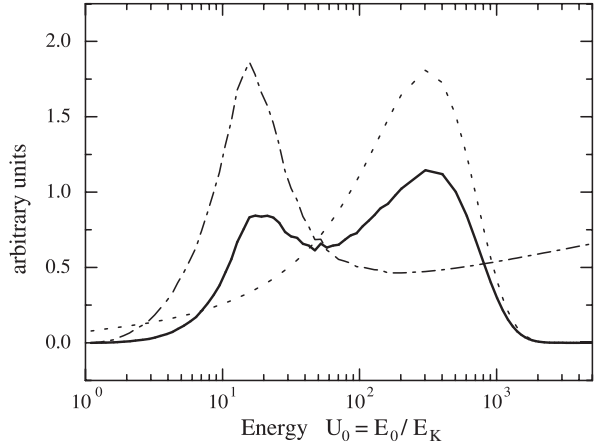


Fig. 6

Fig. 5 – Calculated Ti K_{α} -yield from the laser-irradiated titanium foil as a function of electron temperature T , determined for the relativistic electron energy distribution function $f(U_0, T)$ in eq. (2).

Fig. 6 – Comparison of $f(U_0)$ (dotted line), $I(U_0)$ (dash-dotted line), and $f(U_0) \cdot I(U_0)$ (solid line) as defined in eqs. (5) and (2) for a relativistic electron temperature $T = 1$ MeV.

The path length dx in eq. (1) which the hot electrons with energy U_0 may cover inside the target depends on their incident energy and on the target thickness d . For low-energy electrons which are completely stopped inside the $12\text{ }\mu\text{m}$ target dx represents the Bethe range r_B . This length is defined by the stopping power S of the continuous slowing-down approximation [13]:

$$r_B = \int_1^{U_0} \frac{E_K}{\rho \cdot S} dU \quad \text{with} \quad S = -\frac{E_K}{\rho} \frac{dU}{dx}. \quad (4)$$

As their energy increases, the electrons may escape from the target with a rest energy U_B , which increases with the incident energy U_0 . The travelled path length of the electrons and the rest energy U_B were determined by Monte Carlo simulation. As the electrons loose energy while scattered in the target, the ionization cross-section $\sigma_K(U_0)$ changes during the stopping process (see fig. 4) and has therefore to be integrated over the energy loss dU . For high-energy electrons with $E_0 > 700$ keV, *i.e.* $U_0 > 140$, the energy loss inside the target material is so small that the cross-section $\sigma_K(U_0)$ can be considered to be constant between U_0 and U_B , and the path length dx reduces to the target thickness $d = 12\text{ }\mu\text{m}$. In principle, the space charge built up in the foil due to the escaping electrons could lead to an oscillating motion of some electrons and thus to an increased K_{α} -yield due to returning electrons. This effect is, however, estimated to be small since the return time of the electrons is considerably larger than the laser pulse duration. These considerations lead to the following equation for the K_{α} -production in the titanium foil:

$$N_{\alpha}(T) = n_{\text{Ti}} \eta N_e \int_1^{\infty} f(U_0, T) I(U_0) dU_0, \quad (5)$$

with

$$I(U_0) = \begin{cases} \int_{U_B}^{U_0} \frac{\sigma_K(U)}{\rho \cdot S(U)} \cdot E_K dU, & U_0 \leq 140 \\ d \cdot \sigma_K(U_0), & U_0 > 140 \end{cases}. \quad (6)$$

Solving this integral leads to the number of K_{α} -photons as a function of the electron temperature as plotted in fig. 5. The qualitative behaviour of the calculated K_{α} -yield obviously

shows the same characteristics as the experimental results in fig. 3: after reaching a maximum at an electron temperature of 60 keV the K_{α} -yield drops at higher temperatures before it rises again above $T = 900$ keV. Figure 6 shows the cross-section weighted by the path length $I(U_0)$, the energy distribution $f(U_0, T)$ for the relativistic temperature $T = 1$ MeV and the product $f(U_0, T)I(U_0)$, which is the argument in the yield integral equation (5). Notice the logarithmic energy scale. From $f \cdot I$ it is obvious that mainly electrons with energies E_0 in the range of 500 keV to 5 MeV contribute to the K_{α} -yield at relativistic temperatures. With increasing temperature the share of relativistic electrons in the K_{α} -production grows further. The increasing yield which has been measured for intensities above 10^{18} W/cm² is therefore due to the growing ionization cross-section at relativistic electron energies. This result is in good agreement with the fact that at laser intensities above 10^{18} W/cm² plasma electrons are accelerated to relativistic energies by the ponderomotive potential of the intense laser field [14].

Nevertheless, comparing quantitatively the intensity scale of the experimental data at the maximum and minimum (fig. 3) and the electron temperatures of the model (fig. 5) a discrepancy with previous experimental data is conspicuous [15]. Following the ponderomotive scaling $T \sim (I\lambda^2)^{1/2}$ [14], intensities of $3 \cdot 10^{17}$ W/cm² (corresponding to the maximum of the K_{α} -yield presented here) and $2 \cdot 10^{18}$ W/cm² (at the minimum) should cause hot electron temperatures of about 35 keV and 200 keV, respectively. The calculated K_{α} -yield, however, reaches its maximum at an electron temperature $T = 60$ keV and the minimum at $T = 900$ keV. In the same way vacuum heating ($T \sim (I\lambda^2)$) [16] and resonance absorption scalings ($T \sim (I\lambda^2)^{1/3}$) [17, 18] do not correspond satisfactorily to our experimental data.

Since there is no doubt in the correctness of the K -ionization cross-section σ_K and the interaction length dx between electrons and target, the only free parameter in the integral eq. (5) is the energy distribution $f(U_0, T)$ and its normalization. In the model we assume a relativistic energy distribution, which requires a thermal equilibrium and a constant number of accelerated electrons over the whole intensity regime. However, to date no detailed knowledge about the actual shape of the hot electron distribution in laser-produced plasmas exists. For example, the number of accelerated electrons may well depend on the laser intensity, as the small 600 fs prepulse generates a preplasma whose scale length increases with intensity. To describe phenomenologically electron spectra from laser-produced plasmas a biexponential distribution function $f'(U_0, T_1, T_2) = Ae^{-U_0/T_1} + Be^{-U_0/T_2}$ is frequently assumed [19]. We solved the yield integral eq. (5) for a biexponential distribution taking the ratios A/B and T_1/T_2 from experimental data at a laser intensity of $5 \cdot 10^{18}$ W/cm² on a 12 μm tantalum target. These values and the total absorbed energy were assumed to be constant over the entire intensity range from 10^{16} W/cm² to 10^{19} W/cm². The calculated K_{α} -yield exhibits a maximum at about 200 keV and does not rise at relativistic temperatures. In contrast with this result different 1-dimensional, single-exponential distribution functions were tested, and all of them produced the same qualitative behaviour as shown in fig. 5 with the K_{α} -yield increasing at relativistic temperatures.

These results support the choice of the relativistic energy distribution (eq. (2)), which does not overestimate the contribution of low-energy electrons at high temperatures, as the biexponential distribution does. On the other hand, the discrepancy between the experimental data and the model, even with the relativistic distribution function, points to the fact that the shape and the nature of the electron distribution function of plasmas produced by high-intensity lasers is still unknown.

Conclusions. – We have experimentally determined the yield of Ti K_{α} -radiation from a relativistic laser-produced titanium plasma. The yield exhibits a pronounced maximum at a laser intensity of $3 \cdot 10^{17}$ W/cm², corresponding to a plasma electron temperature of about

five times the titanium K -shell ionization energy. Above laser intensities of 10^{18} W/cm^2 the K_α -yield increases due to the influence of the logarithmically increasing cross-section at relativistic electron energies. This can be deduced from our analytical model including a relativistic electron energy distribution and the cross-section for K -shell ionization.

Since the number of fast electrons still increases with laser intensity, a further increase of the K_α -yield above the reached maximum of 10^{12} photons/shot/ 4π appears to be possible at higher laser intensities. Furthermore, at high intensities mostly the high-energy electrons contribute to the K_α -radiation as we have shown before. These electrons are not significantly deflected inside the titanium foil, from which it follows that the emission volume of K_α -radiation due to relativistic electrons should be in the order of the focus size.

* * *

The authors gratefully acknowledge informative discussions with I. USCHMANN, P. GIBBON, and C. REICH who also performed the Monte Carlo calculation of U_B .

REFERENCES

- [1] KEY M. H. *et al.*, *Phys. Plasmas*, **5** (1998) 1966.
- [2] SCHWOERER H. *et al.*, *Phys. Rev. Lett.*, **86** (2001) 2317.
- [3] FEURER T. *et al.*, *Phys. Rev. E*, **65** (2001) 016412.
- [4] EDER D. *et al.*, *Appl. Phys. B*, **70** (1999) 211.
- [5] HARES J. D. *et al.*, *Phys. Rev. Lett.*, **42** (1979) 1216.
- [6] ROUSSE A. *et al.*, *Phys. Rev. E*, **50** (1994) 2200.
- [7] REICH C. *et al.*, *Phys. Rev. Lett.*, **84** (2000) 4846.
- [8] DANGERFIELD G. R. and SPICER B. M., *J. Phys. B*, **8** (1975) 1744.
- [9] QUARLES C. A., *Phys. Lett. A*, **39** (1972) 375.
- [10] LIU M. *et al.*, *At. Data Nucl. Data Tables*, **76** (2000) 213.
- [11] NEUGEBAUER G., *Relativistische Thermodynamik* (Akademie Verlag, Berlin) 1980.
- [12] QUARLES C. A., *Phys. Rev. A*, **13** (1976) 1278.
- [13] BETHE H., *Ann. Phys. (Leipzig)*, **5** (1930) 325.
- [14] WILKS S. C. *et al.*, *Phys. Rev. Lett.*, **69** (1992) 1383.
- [15] GIBBON P. and FÖRSTER E., *Plasma Phys. Control. Fusion*, **38** (1996) 769.
- [16] BRUNEL F., *Phys. Rev. Lett.*, **59** (1987) 52.
- [17] FORSLUND D. W. and KINDEL J. M. and LEE K., *Phys. Rev. Lett.*, **39** (1977) 284.
- [18] GIBBON P. and BELL A. R., *Phys. Rev. Lett.*, **68** (1992) 1535.
- [19] BEZZERIDES B., GITOMER S. and FORSLUND D., *Phys. Rev. Lett.*, **44** (1980) 651.

MeV X Rays and Photoneutrons from Femtosecond Laser-Produced Plasmas

H. Schwoerer,¹ P. Gibbon,¹ S. Düsterer,¹ R. Behrens,^{1,2} C. Ziener,¹ C. Reich,¹ and R. Sauerbrey¹

¹Institut für Optik und Quantenelektronik, Friedrich-Schiller-Universität, Max-Wien-Platz 1, 07743 Jena, Germany

²Physikalisch-Technische Bundesanstalt, Bundesallee 100, 38116 Braunschweig, Germany

(Received 17 July 2000)

We demonstrate a novel method to monitor the total angular distribution of the spectrum of hard x-ray emission from a plasma generated with femtosecond laser pulses with an intensity of $5 \times 10^{18} \text{ W/cm}^2$ on a solid target. Measured and calculated angular distributions of x rays show a pronounced anisotropy for MeV photon energies. We complemented the spectral information by demonstrating a (γ, n) nuclear reaction with a tabletop laser system.

DOI: 10.1103/PhysRevLett.86.2317

PACS numbers: 52.27.Ny, 52.38.-r, 52.70.La

The interaction of an ultraintense femtosecond laser pulse with matter acts as a source of hot electrons, ions, and neutrons, as well as x rays of unique properties [1–5]: The duration of emission of both fast particles and short wavelength radiation is expected to be ultrashort, the area of the source is in the range of the laser focal spot size, and the emission becomes nonisotropic once the laser intensity exceeds 10^{18} W/cm^2 , the intensity at which the generated hot electrons become relativistic [6,7]. These properties describe a source of excellent brightness, which may be used in subpicosecond time resolved diffraction experiments, imaging in ultrashort wavelength lithography, or to deliver ultrahigh radiation intensities for linear or even nonlinear x-ray-atom and x-ray-nuclei interactions.

One future application of ultrashort bunches of hot particles is the ignition of fusion in a precompressed pellet target [8]. This explains the tremendous theoretical and experimental efforts toward the generation of collimated particle beams with a well-known spectral shape. An even more visionary application of the emissions from femtosecond laser-produced plasmas is the transmutation of elements by proton interaction or neutron capture, such as deactivation of long-lived fission fragments or activation of short-lived isotopes used in radiological diagnostics and radiotherapy [9].

Beside these applications in spectroscopy and technology there is particular interest in analyzing the fundamental mechanisms responsible for the irreversible acceleration of electrons in fs laser-produced plasmas up to energies of many MeV and the subsequent photon generation [10,11]. Collective absorption processes, such as Brunel absorption and resonance absorption, become dominant for intensities above $I = 10^{16} \text{ W/cm}^2$. In a long scale preplasma, Raman instabilities, plasma wake-field acceleration, and relativistic self-focusing of the laser pulse also lead to suprathermal electron velocities [12].

Previous measurements of the hot electron temperature T_e in short pulse interactions indicate that one of several scaling laws may apply depending on the incidence angle and the density scale length [7]. For normally incident light, the “ponderomotive” scaling [13]

$$k_B T_e \simeq 0.511 \text{ MeV} [(1 + I\lambda^2/1.37 \times 10^{18} \text{ W cm}^{-2} \mu\text{m}^2)^{1/2} - 1] \quad (1)$$

has been verified for electrons directed along the target normal, exiting the rear side [1]. Obliquely incident light gives rise to a scaling $k_B T_e \propto (I\lambda^2)^{1/3}$ associated with resonance absorption [14]. Shorter pulses and/or steeper gradients result in a similar scaling, but numerically lower values for T_e [10]. However, the total yield of electrons, photons, or secondary created particles depends on various experimental parameters such as target element, target surface properties, density scale length of plasma generated by laser prepulses, and, finally, laser polarization and direction of emission.

We demonstrate a novel method to simultaneously monitor spectrum and angular distribution over 2π of hard x-ray emission in absolute photon numbers from a femtosecond laser-produced plasma, generated with a laser intensity of $5 \times 10^{18} \text{ W/cm}^2$ on the solid target. As a first application of these laser-produced MeV x rays, we released neutrons via a ${}^9\text{Be}(\gamma, n)2\alpha$ reaction, demonstrating for the first time laser fission with a tabletop laser system.

The experiments described here were performed with the multi-TW Ti:sapphire laser system in Jena. The laser generates pulses of 60 fs duration, center wavelength of 800 nm, an energy of 250 mJ, and a repetition rate of 10 Hz. Two prepulses at 600 fs and 4 ps before the main laser pulse are known with relative intensities of 5×10^{-4} and 10^{-4} with respect to the main pulse. The range from 4 to 300 ps and from 2 ns on are prepulse free to a contrast ratio better than 10^5 . The pulses are focused with a $f/2$ parabola to $(4 \times 7) \mu\text{m}^2$, containing 50% of the energy. Incident angle on target is 45° , polarization parallel. The peak intensity on target is $5 \times 10^{18} \text{ W/cm}^2$. The target is a 1.0 mm thick smoothed tantalum sheet ($Z = 73$). The target was moved between laser shots. For each run the radiation is accumulated over 20 000 shots.

The hard x-ray spectrum is measured with 12 spectrometers based on thermoluminescence detectors (TLD) [15,16]

(Fig. 1). Our spectrometers allow the absolute measurement of the photon fluence for photon energies between 10 keV and 2 MeV with a relative resolution of 20%. It was carefully verified that no scattered x rays excite the TLDs. No evidence of electrons penetrating through a 2 cm thick polymethylmethacrylate (PMMA) cover into the TLD stacks was found [17]. Contributions to the x-ray spectrum by bremsstrahlung generated in the PMMA were determined to be less than 15% by comparing the results from several TLDs equipped with front filters with either low or high Z materials, giving different radiation conversion coefficients.

Figure 2 displays two x-ray spectra detected by TLD spectrometers in the direction of specular reflection (solid circles) and in the forward direction with respect to the incident laser pulse (open squares). The absolute photon yield is given in number of photons per laser shot, keV, and sr. From the exponential decrease of the x-ray spectrum at high energies (solid line), we calculate a hot electron temperature T_e supposing bremsstrahlung from electrons with a Maxwellian energy distribution. Deconvolution of the TLD readings using a SAND II algorithm [15] yields $T_e \approx 700$ keV in the specular direction and $T_e \approx 300$ keV for the forward laser direction on the back side of the tantalum. The electron temperature is consistent with the ponderomotive scaling (see above), which predicts an electron temperature of 420 keV for a laser intensity of $5 \times 10^{18} \text{ W/cm}^2$.

The photon flux scales nearly quadratically with the laser pulse energy: a 250 J shot in Livermore generated about 2×10^8 photons/(keV sr) at photon energy of 2 MeV which is 10^6 times more than 200 photons/(keV sr) with our 250 mJ pulse [18]. And

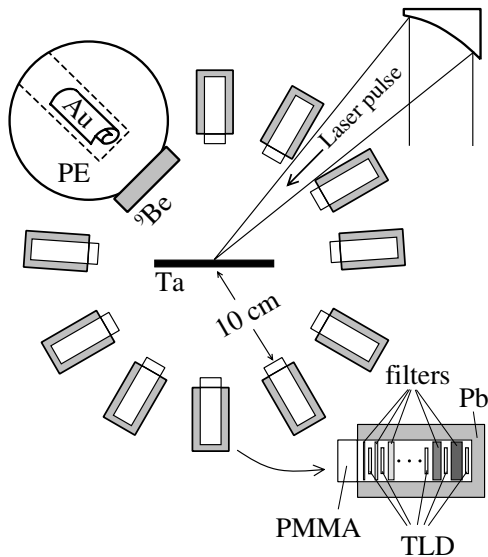


FIG. 1. Experimental setup for x-ray and photoneutron measurements. The inset shows the alternating arrangement of filters and TLDs in the x-ray spectrometers.

with a 25 J laser pulse 5×10^5 photons/(keV sr) at 2 MeV were counted in an experiment at the Rutherford Appleton Laboratory, which is again almost quadratic in energy [6].

Spectra similar to Fig. 2 were recorded in twelve directions within the plane of incident laser and target normal. Figure 3 shows the angular distribution of the x-ray temperatures retrieved from the high energy slope of the TLD spectrometer data (solid circles). The laser pulse impinges p polarized under 45° with respect to target normal. The maximum of about 500 keV is seen between the specular reflection and target front normal (330°), whereas in forward direction (215°) the temperature is only 200 keV.

Figure 4 displays the number of photons per keV, sr, and shot on a logarithmic scale as a function of the angle for three different photon energies: 488, 1160, and 1950 keV. Again, for energies above 500 keV the angular distribution is peaked on the front side of the target close to the specular direction.

The angle θ_e with which electrons are ejected from the target surface while the laser is incident can be found by momentum and energy conservation—analogously to free electrons ejected by a lateral ponderomotive force in an underdense plasma [19]. For the target geometry of Fig. 3, this is given by

$$\theta_e = 2\pi - \arctan\left\{\frac{U \sin\theta}{\sqrt{2U + U^2 \cos^2\theta}}\right\}, \quad (2)$$

where $U = \gamma - 1 = E/mc^2$ is the normalized final kinetic energy of the electron and θ the incident angle. In the absence of scattering and self-induced fields, this result is independent of the acceleration mechanism. Similar expressions for oblique-incidence laser-solid geometry have been quoted by others [20]. The expression in Eq. (2) essentially says that the emission angle of electrons increases with kinetic energy, from $\theta_e = 0$ for $E \rightarrow 0$ up to $\theta_e = 2\pi - \theta$, the specular direction for $E \gg mc^2$.

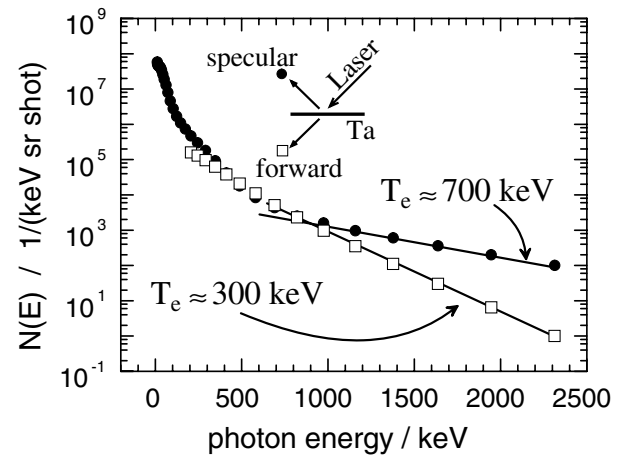


FIG. 2. Two characteristic x-ray spectra for different directions of emission, showing the deviation in hot electron temperatures.

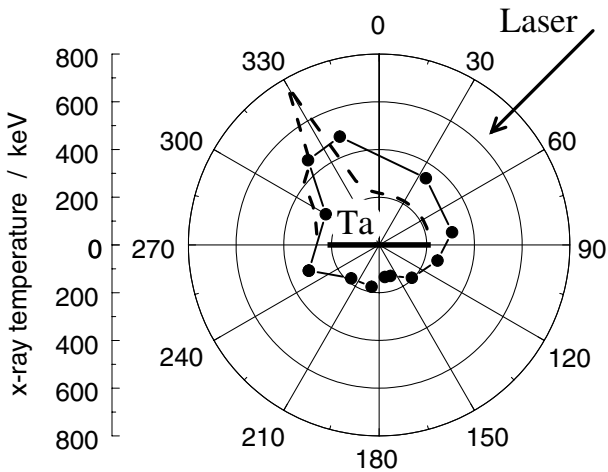


FIG. 3. Angular dependence of the hot x-ray temperature. The circles are derived from the measured x-ray spectra. The dashed line shows the photon temperature due to a Maxwellian electron distribution of electrons ejected from the target surface (see text).

The angular distribution of the x rays points to some interesting features. Bremsstrahlung from weakly relativistic electrons ($E_\gamma < 0.5$ MeV) shows no significant deviation from isotropic emission. This may be attributed to multiple scattering of fast electrons in the target and the dipolar emission character of the bremsstrahlung. Therefore no direction is favored. This behavior changes distinctly for x-ray energies greater than the electron rest mass ($E_\gamma > 0.5$ MeV). Bremsstrahlung emission of electrons in this energy range is strongly peaked in the propagation direction of the electrons. This suggests that the detected angular distribution of MeV radiation resembles the distribution of the highly relativistic electrons. For the three energies in Fig. 4, Eq. (2) predicts emission angles of 325° (1950 keV), 329° (1160 keV), and 336° (488 keV), respectively, consistent with the observed x-ray emission peak of

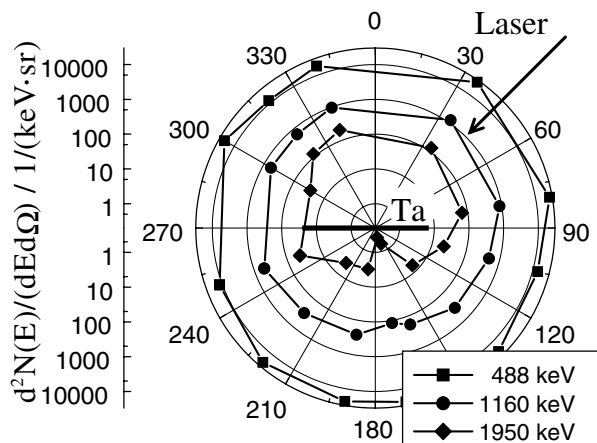


FIG. 4. Angular distribution of the photon flux for three different photon energies. The logarithmic scaled plot shows a significant asymmetry for $E_\gamma > 500$ keV.

(330 ± 10)° for energies beyond 1 MeV. Our data therefore imply a jet of highly energetic electrons close to, but not exactly in, the specular reflection direction of the laser.

To analyze the data in Fig. 3 more fully, we suppose that a number of electrons are ejected from the target surface with a Maxwellian energy distribution $f(U) = T_e^{-1} \exp -U/T_e$. Combined with Eq. (2), this leads to an angular distribution $f(\theta_e)$ of emitted electrons, peaked near $\theta_e(T_e)$. To get the observed x-ray emission at a given detection angle, we sum the bremsstrahlung emission in the preplasma due to *all* electrons, weighted by $f(\theta_e)$ and taking into account the relativistic photon emission distribution [21]. The result is shown as the dashed line in Fig. 3 for an initial *electron* temperature of 300 keV. The broadening around the peak temperature exhibited by the experimental curve may be due either to an isotropic contribution from electrons in the target bulk, or to elastic scattering of electrons in the preplasma.

Assuming a 10% energy transfer from the laser pulse to suprathermal electrons, one finds that the plasma density in front of the target required to generate the measured x-ray yield in the specular direction is a few 10^{20} cm⁻³, for a plasma volume of $(10 \mu\text{m})^3$ given by the laser focus \times the preplasma expansion within 100 ps. 10^{20} cm⁻³ is a realistic preplasma density generated with the unavoidable prepulse of multi-TW Ti:sapphire laser systems.

Electrons which are not reflected penetrate into the Ta bulk and generate bremsstrahlung. Some of these may also be scattered back out again (Molière scattering), particularly if they enter at the bulk with a finite angle [22]. The angular distribution of the bulk bremsstrahlung was calculated using a Monte Carlo model [23]. It contributes to the measured signal as an almost isotropic part.

In an experiment at the Rutherford Appleton Laboratory, Santala *et al.* observed anisotropic x-ray emission on the rear side of a thick tantalum target for photon energies above 10 MeV. The emission angle shifts from target normal (180° in the geometry of Fig. 3) to laser direction (225°) with increasing plasma scale length [7].

Kodama *et al.* [24] reported jets that give rise to x-ray emission in a substantial preformed plasma. They interpret their results using numerical simulations such that strong magnetic fields in connection with the specularly reflected laser light produce the electron jets. In our present experiments and complementary particle-in-cell simulations, a magnetic field is not required for directed electron emission and the direction of the electron emission is different from the specular direction.

Photonuclear reactions are widely used to characterize multi-MeV bremsstrahlung from conventional electron accelerators [25]. Very recently, (γ, n) reactions of several elements were successfully applied by both the Livermore and Rutherford Appleton Laboratories to characterize the bremsstrahlung spectrum of 1 PW and 100 TW laser-produced plasmas [16,18,26]. The applied intensities exceeded our values by factors of 100 and 10, the

deposited energies and the size of the laser system by 1000 and 100, respectively. However, the repetition rate is lower by a factor of 10 000 compared to our tabletop laser system.

Photons with energy above 1.67 MeV can disintegrate beryllium via a ${}^9\text{Be}(\gamma, n)2\alpha$ reaction. We placed a beryllium disk (12 mm thick, 70 mm diam) 4.5 cm away from the laser plasma in the specular direction of the incident laser, covering a solid angle of 1.3 sr (Fig. 1). The Be disk was wrapped in 60 μm thick aluminum foil and mounted on the surface of a polyethylene sphere (Bonner sphere) of 12.5 cm diameter [27]. About 40% of the neutrons generated in the Be disk enter the Bonner sphere and are thermalized by inelastic scattering with hydrogen and carbon. The neutron thermalization efficiency of the Bonner sphere was absolutely calibrated for the relevant neutron energies. A gold disk (${}^{197}\text{Au}$, 16 g) was placed in the center of the Bonner sphere, capturing thermal neutrons ${}^{197}\text{Au} + n \rightarrow {}^{198}\text{Au}$ with a cross section of 99 b. ${}^{198}\text{Au}$ undergoes a beta decay with a lifetime of 2.7 d into ${}^{198}\text{Hg}$ promptly followed by emission of a 411.8 keV γ . The γ spectrum was collected by a Ge detector located 1 km below Earth for reduction of Au excitation by cosmic neutrons and low γ background [28].

In addition we placed several CR39 plastic nuclear track detectors around the tantalum target to monitor ions with energies $E > 100$ keV. None of the detectors showed protons with energies high enough to penetrate 60 μm of aluminum foil, which, in particular, excludes contribution from the ${}^9\text{Be}(p, n){}^9\text{B}$ reaction to the neutron generation.

After 20 000 laser shots the activity of the ${}^{198}\text{Au}$ due to thermalized photoneutrons exceeded the natural background activation of gold by a factor of 2.5. This corresponds to about 100 photoneutrons per shot from the (γ, n) disintegration. *Fusion* neutrons were recently generated in two experiments elsewhere. Pretzler *et al.* generated 140 *fusion* neutrons per shot irradiating deuterated polyethylene target by a 2 TW laser [4]. Ditmire *et al.* counted 10^4 neutrons from deuterium *fusion* with a 100 mJ laser pulse into large D clusters [29].

From the number of neutrons generated in the beryllium disk one can infer the total number N_p of photons with energies larger than 1.67 MeV emitted from the relativistic plasma: Using an averaged photoneutron cross section of 0.5 mb above 1.67 MeV, we calculate $N_p = 3 \times 10^4$ (sr^{-1}), which corresponds well to the integrated photon yield of $N_{\text{TLD}} \approx 10^5$ (sr^{-1}) in the hot electron wing above 1.67 MeV which was achieved in the TLD measurement in the specular direction.

In conclusion, we measured for the first time the complete angular distribution of the hard x-ray spectrum of a relativistic, laser-produced plasma, generated on a tantalum surface with a light intensity of $5 \times 10^{18} \text{ W/cm}^2$. We explained the strongly anisotropic x-ray emission charac-

teristics at relativistic photon energies by the bremsstrahlung generation of hot electrons ejected from the target surface and electrons penetrating into the bulk. Utilizing the detailed knowledge of the x-ray spectra we induced the photonuclear reaction ${}^9\text{Be} + \gamma \rightarrow 2\alpha + n$ by MeV photons from the laser-produced Ta plasma and demonstrated the neutron capture reaction ${}^{197}\text{Au} + n \rightarrow {}^{198}\text{Au}^*$ with our compact laser neutron source.

The authors thank H. Langhoff and R. Nolte for stimulating discussions and gratefully acknowledge technical assistance by F. Ronneberger. The work was funded by the Deutsche Forschungsgemeinschaft (Schw 766/2-2 and Gi 300/1-1).

- [1] G. Malka and J. L. Miquel, Phys. Rev. Lett. **77**, 75 (1996).
- [2] K. Krushelnick *et al.*, Phys. Rev. Lett. **83**, 737 (1999).
- [3] E. L. Clark *et al.*, Phys. Rev. Lett. **84**, 670 (2000).
- [4] G. Pretzler *et al.*, Phys. Rev. E **58**, 1165 (1998).
- [5] M. D. Perry *et al.*, Rev. Sci. Instrum. **70**, 265 (1999).
- [6] P. A. Norreys *et al.*, Phys. Plasmas **6**, 2150 (1999).
- [7] M. I. K. Santala *et al.*, Phys. Rev. Lett. **84**, 1459 (2000).
- [8] M. Tabak *et al.*, Phys. Plasmas **1**, 1626 (1994).
- [9] H. Arnould *et al.*, Phys. Lett. B **458**, 167 (1999).
- [10] P. Gibbon and E. Förster, Plasma Phys. Controlled Fusion **38**, 769 (1996).
- [11] F. Brunel, Phys. Rev. Lett. **59**, 52 (1987); P. Mulser *et al.*, Laser Phys. **10**, 231 (2000).
- [12] C. D. Decker *et al.*, Phys. Rev. E **50**, R3338 (1994); T. Tajima *et al.*, Phys. Rev. Lett. **43**, 267 (1979); A. Pukhov and J. Meyer-ter-Vehn, Phys. Plasmas **5**, 1880 (1998).
- [13] S. C. Wilks *et al.*, Phys. Rev. Lett. **69**, 1383 (1992).
- [14] F. N. Beg *et al.*, Phys. Plasmas **4**, 447 (1997).
- [15] R. Nolte *et al.*, Radiat. Prot. Dosim. **84**, 367 (1999).
- [16] M. H. Key *et al.*, Phys. Plasmas **5**, 1966 (1998).
- [17] M. Schnürer *et al.*, Phys. Rev. E **61**, 4394 (2000).
- [18] T. E. Cowan *et al.*, Phys. Rev. Lett. **84**, 903 (2000).
- [19] C. I. Moore *et al.*, Phys. Rev. Lett. **74**, 2439 (1995).
- [20] Y. Sentoku *et al.*, Phys. Plasmas **6**, 2855 (1999); H. Ruhl *et al.*, Phys. Rev. Lett. **82**, 743 (1999); A. A. Andreev *et al.*, JETP **89**, 632 (1999); Z.-M. Sheng *et al.*, Phys. Rev. Lett. **85**, 5340 (2000).
- [21] B. K. Agarwal, *X-Ray Spectroscopy* (Springer, Heidelberg, 1991).
- [22] H. Frank, Z. Naturforsch. **14A**, 247 (1959).
- [23] D. C. Joy, *Monte Carlo Modelling for Electron Microscopy and Microanalysis* (Oxford University Press, Oxford, 1995).
- [24] R. Kodama *et al.*, Phys. Rev. Lett. **84**, 674 (2000).
- [25] J. J. Carroll *et al.*, Rev. Sci. Instrum. **64**, 2298 (1993).
- [26] K. W. D. Ledingham *et al.*, Phys. Rev. Lett. **84**, 899 (2000).
- [27] B. Wiegel *et al.*, Physikalisch-Technische Bundesanstalt Report No. PTB-N-21, 1994.
- [28] S. Neumaier *et al.*, Appl. Radiat. Isot. **53**, 173 (2000).
- [29] T. Ditmire *et al.*, Phys. Plasmas **7**, 1993 (2000).

Contrib. Plasma Phys. **41** (2001) 2-3, 171–174

Hard x-rays and nuclear reactions from laser produced plasmas

S. DÜSTERER^a, H. SCHWOERER^a, R. BEHRENS^{a,b}, C. ZIENER^a, C. REICH^a, P. GIBBON^a, R. SAUERBREY^a

^aInstitut für Optik und Quantenelektronik, Friedrich-Schiller-Universität, Max-Wien-Platz 1, D-07743 Jena, Germany

^bPhysikalisch-Technische Bundesanstalt, Bundesallee 100, 38116 Braunschweig, Germany
e-mail:schwoerer@qe.physik.uni-jena.de

Abstract

We report on a fully angular resolved spectrum of hard x-rays emitted from a laser produced plasma, which is generated by a laser intensity of $5 \times 10^{18} \text{ W/cm}^2$ on a tantalum surface. MeV x-rays were utilized to generate photoneutrons via photofission of beryllium.

1 Introduction

In the last decade it has become possible to generate focused laser light intensities exceeding 10^{18} W/cm^2 within a few tens of femtoseconds. This enormous peak intensity focussed onto a solid target creates relativistically moving electrons in a hot and dense plasma spot which radiates in the entire spectral range up to several MeV. Electrons and ions are emitted with rather high energies and even nuclear reactions (e.g. fusion, photofission) can take place [1, 2, 3, 4, 5, 6, 7]. We show measurements of the spectral composition and the angular distribution of the emitted hard x-rays (10 keV to 2 MeV). The absolutely calibrated x-ray spectrometers used allow us to measure absolute photon numbers in 16 channels. We report for the first time about laser nuclear fission with a table top laser system.

2 Experimental setup and x-ray measurements

The experiments described here were performed with the multi Terawatt Ti:Sapphire laser system in Jena. The laser generated pulses of 60 fs duration, center wavelength of 800 nm, an energy of 250 mJ and a repetition rate of 10 Hz. The pulses were focused with a f/2 parabolic mirror to $4 \times 7 \mu\text{m}^2$, containing 50% of the energy. The laser impinged under 45° onto the 1.0 mm thick smoothed tantalum ($Z=73$) target. A peak intensity of $5 \times 10^{18} \text{ W/cm}^2$ was reached. The hard x-ray spectrum was measured using 12 spectrometers based on thermoluminescence detector (TLD) stacks[8] (see Fig.1). These spectrometers allowed the absolute measurement of the photon fluence for photon energies between 10 keV and 2 MeV with a spectral resolution of 20%. It was carefully verified that no scattered x-rays and no electrons excite the TLDs. Fig. 2 displays two x-ray spectra, detected by TLD spectrometers in the direction of specular reflection (solid circles) and in forward direction (open squares) with respect to the incident laser pulse. The absolute photon yield is given in number of photons per laser shot, keV and sr. From the exponential decrease of the x-ray spectrum at high photon energies (solid line), we calculated a hot electron temperature T_e supposing Bremsstrahlung is generated by electrons with a Maxwellian energy distribution.

Deconvolution of the TLD readings using a SAND II algorithm[8] yields $T_e = 700$ keV in specular direction and $T_e = 300$ keV for the forward laser direction on the back side of the tantalum. Spectra similar to Fig. 2 were recorded in twelve directions within the plane of incident laser and target normal. Fig. 3 shows the angular distribution of the electron temperatures.

3 Discussion of the results and theoretical considerations

The transverse electric field of the laser pulse forces the electrons to a wiggling motion. Therefore the electrons gain the so called quiver energy. PIC simulations show that this quiver energy equals - derived for perpendicular incidence - the hot electron temperature $k_B T_e$

$$k_B T_e \sim m_e c^2 \left(\sqrt{1 + 7.28 \times 10^{19} (I\lambda^2)} - 1 \right) \quad (1)$$

For 45° angle of incidence and p-polarized light a similar scaling law ($k_B T_e \propto (I\lambda^2)^{1/3}$) is in good agreement with several experiments[9]. Equation (1) predicts an electron temperature of 420 keV for a laser intensity of $5 \times 10^{18} \text{ W/cm}^2$ which is consistent with our measurement, where the hot electron temperature varies between 200 keV and 700 keV (see Fig. 3).

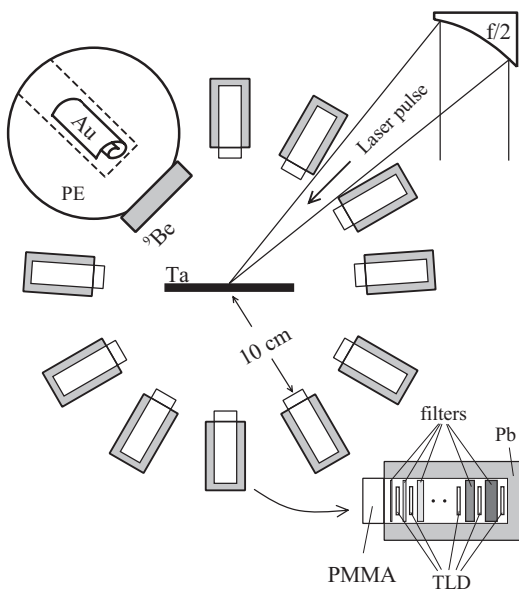


Fig. 1: Experimental setup for x-ray and photon detection. The inset shows the alternating arrangement of filters and TLDs in the x-ray spectrometers.

However, the total yield of electrons, photons or secondary particles created depends on various experimental parameters such as target element, target surface properties, density scale-length of plasma generated by laser prepulses and finally laser polarization and direction of emission. The angular distribution of the x-rays points to some interesting features. Bremsstrahlung from weakly relativistic electrons ($E_\gamma \leq 0.5$ MeV) shows no significant deviation from isotropic emission. This behavior changes distinctly for x-ray energies greater than the electron rest mass ($E_\gamma > 0.5$ MeV). Bremsstrahlung emission of electrons in this energy range is peaked in the propagation direction of the electrons. This suggests that the detected angular distribution of MeV radiation resembles the distribution of the highly relativistic electrons. Our data therefore

imply the existence a jet of highly energetic electrons close to the specular reflection direction of the laser. Similar effects - but for other conditions and due to different mechanisms - were seen by other groups using laser powers as low as 0.5 TW (50mJ, 120fs) [10] and as powerful as 100TW (50J, 500fs)[11]. As experimentally verified by ref.[1] and [10] we assume 0.5-1% energy transfer from the laser pulse to suprathermal electrons. Yu et al.[12] performed PIC simulations with parameters similar to

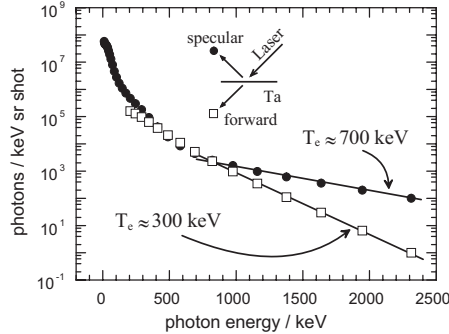


Fig. 2: Spectrum of hard x-rays; specular direction (circles) and behind the target (squares)

our experiment, but with perpendicular incidence. They found more than half of the suprathermal electrons that are created in the interaction were accelerated in back direction by the reflected laser light. Assuming a similar fraction of electrons was accelerated in the specular direction for our geometry and taking into account the measured T_e , one finds that the plasma density in front of the target, required to generate the measured x-ray yield in the specular direction is $n_i \approx (10^{20} - 10^{21}) \text{ cm}^{-3}$, for a plasma volume of $(10 \mu\text{m}^3)$ (laser focus \times the preplasma expansion within a few ps). This is a realistic preplasma density generated by the unavoidable prepulse of TW Ti:sapphire laser systems.

4 Application of the MeV x-rays: photoneutrons

We used the MeV x-rays to initiate photonuclear reactions. Neutrons were produced by a (γ, n) -reaction in Beryllium via ${}^9\text{Be} + \gamma \rightarrow \alpha + \alpha + n$. The Beryllium was split by γ (i.e. hard x-rays from the laser produced plasma) exceeding the threshold energy of 1.67 MeV. We placed a Beryllium disk (12 mm thick, 70 mm diameter) 4.5 cm away from the laser plasma in specular direction of the incident laser (Fig. 1). The Be disk was mounted on the surface of a polyethylene sphere of 12.5 cm diameter. About 40% of the neutrons generated in the Be disk entered the Bonner sphere and were thermalized by inelastic scattering with hydrogen and carbon nuclei. The neutron thermalization efficiency of the Bonner sphere was absolutely calibrated for the relevant neutron energies. A gold disk (${}^{197}\text{Au}$, 16 g) was placed

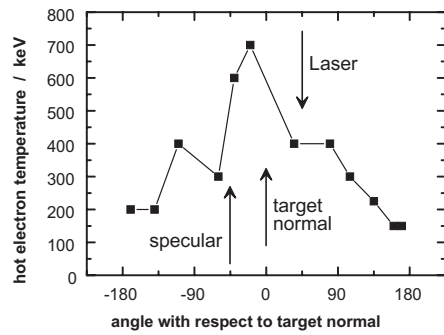


Fig. 3: The angular distribution of hot electron temperature is distinctly peaked between specular direction and target normal

in the center of the Bonner sphere, capturing thermal neutrons $^{197}\text{Au} + n \rightarrow ^{198}\text{Au}$ with a cross-section of 99 barn. ^{198}Au decays by emission of a 411.8 keV γ with a half-life of 2.7 d. The γ -spectrum was collected by a Ge-detector. After 20,000 laser shots the activity of the ^{198}Au due to thermalized photoneutrons exceeded the natural background activation of gold by a factor of 2.5. This corresponds to about 100 photoneutrons per shot after correction for solid angles, thermalization probability in the Bonner sphere, capturing cross-section of Au and Ge-detector response. To our knowledge this was the first observation of a (γ ,n)-disintegration with a laboratory size laser system. From the number of neutrons generated in the Beryllium disk, one can infer the total number N_P of photons with energies larger than 1.67 MeV emitted from the relativistic plasma: Using an averaged photoneutron cross-section of 0.5 mbarn above 1.67 MeV, we calculated $N_P = 2.5 \times 10^4$ (sr^{-1}), which corresponds well to the integrated photon yield of $N_{\text{TLD}} = 1 \times 10^5$ in the hot electron wing above 1.67 MeV achieved in the TLD measurement in specular direction. In our measurement the neutron yield was used to cross-check the TLD readings, whereas in interactions with more energetic laser pulses (resulting in a higher photon flux) and higher intensities (increased hot electron temperature) the photon fluxes above 2 MeV will dramatically increase. Since the detection range of the TLDs ends at about 2 MeV one has to think of a different method. Photonuclear reactions with well-defined thresholds and well-known reaction cross-sections are an interesting substitute.

5 Conclusion

In conclusion we have performed the first measurement of the angular distribution in the plane of incidence of the hard x-ray spectrum. The x-rays were emitted by a relativistic, laser produced plasma, generated with a laser intensity of $5 \times 10^{18} \text{ W/cm}^2$. We showed the strongly anisotropic x-ray emission characteristics at relativistic photon energies by Bremsstrahlung generation of hot electrons reflected on the target surface. Utilizing the detailed knowledge of the x-ray spectra we induced the photonuclear reaction $^{9}\text{Be} + \gamma \rightarrow \alpha + \alpha + n$ by MeV photons from the laser produced tantalum plasma and demonstrated the neutron capture reaction $^{197}\text{Au} + n \rightarrow ^{198}\text{Au}$ with our compact laser neutron source.

References

- [1] FEURER, T. ET AL., Phys. Rev. E **56**(1997)4608
- [2] KRUSHELNICK, E. ET AL., Phys. Rev. Lett. **83**(1999)737
- [3] DITMIRE, T. ET AL., **7**(2000)1993
- [4] KMETEC J.D. ET AL., Phys. Rev. Lett., **68**(1996)1527
- [5] LEDINGHAM, K.W.D. ET. AL., Phys. Rev. Lett. **84**(2000)899
- [6] COWAN, T.E. ET. AL., Phys. Rev. Lett., **84**(2000)903
- [7] KEY, M.H.ET. AL., Phys. Plasmas, **5**(1998)1966
- [8] NOLTE, R. ET AL., Rad. Prot. Dos., **84**(1999)367
- [9] GIBBON, P., FÖRSTER, E., Plasma Phys. Control. Fusion, **38**(1996)769
- [10] BASTIANI, S. ET AL., Phys. Rev. E, **56**(1997)7179
- [11] KODAMA, R. ET AL., Phys. Rev. Lett., **84**(2000)674
- [12] YU, W. ET AL., Phys. Rev. Lett., **85**(2000)570

7.3 Apparatives

[4]: S. 77

Christian Ziener, Gregor Stobrawa, Heinrich Schwoerer, Ingo Uschmann, Roland Sauerbrey;
„A novel device for the generation of controlled prepulses in a Ti:Sapphire amplifier chain“,
Rev. Sci. Instr. **71**, 3313-3316 (2000).

[10]: S. 81

Rolf Behrens, Heinrich Schwoerer, Stefan Düsterer, Roland Sauerbrey, Stefan Karsch, Georg
Pretzler;
„A TLD based few-channel spectrometer for simultaneous detection of electrons and photons
from relativistic laser-produced plasmas“,
zur Veröffentlichung angenommen von Review of Scientific Instruments.

Novel device for the generation of controlled prepulses in a Ti:sapphire laser amplifier chain

Ch. Ziener,^{a)} G. Stobrawa, H. Schwoerer, I. Uschmann, and R. Sauerbrey
*Institut für Optik und Quantenelektronik, Friedrich-Schiller-Universität Jena, Max-Wien-Platz 1,
D-07743 Jena, Germany*

(Received 20 April 2000; accepted for publication 22 May 2000)

For the generation of a well defined prepulse in high intensity laser plasma interactions, we implemented a newly developed prepulse device into a multiterawatt titanium:sapphire amplifier system. The temporal delay between the prepulse and main pulse is variable between -350 ps and $+100$ ps. If the laser pulse is focused on a target, the spatial overlap of the two pulses in the focal point is corrected automatically over the entire range. It is possible to attenuate the main pulse as well as the prepulse independently of each other by more than one order of magnitude. We investigated the dependence of the $K\alpha$ emission of the laser produced plasma of a silicon target on the delay between the prepulse and main pulse. An increase of the yield of the $K\alpha$ emission by a factor of 2 for a temporal delay of several tens of picoseconds between the prepulse and main pulse was measured. © 2000 American Institute of Physics. [S0034-6748(00)01009-1]

I. INTRODUCTION

With the evolution of chirped pulse amplification (CPA)¹ and its application to Ti:sapphire lasers^{2,3} tabletop laser systems are now able to achieve intensities of more than 10^{19} W cm⁻² on target.⁴ So it becomes possible in many laboratories to investigate the interaction between such intense laser pulses with matter. These laser produced plasmas are of increasing interest as sources of x rays,⁵⁻⁸ electrons,⁹⁻¹¹ and neutrons.^{12,13}

In most cases, the interaction of the laser pulse with the plasma depends very strongly on a number of parameters, the most important ones are electron and ion density, the corresponding density gradients, the temperature, and the degrees of ionization in addition to the target material.

In the case of a temporally very clean pulse, i.e., a pulse with a very good contrast ratio (ratio between the peak intensity and the intensity at a certain time before the main laser pulse, typically some ps–ns), the laser pulse interacts with a plasma of high density (about solid density).¹⁴⁻¹⁶ However, for many experiments the interaction of the laser pulse with a plasma which shows a specific gradient of the electron density is desirable.

The prepulses necessary for the generation of such a preplasma were generated in the past in different ways. The amplified spontaneous emission (ASE) of the amplifier system was used as a prepulse¹⁷⁻¹⁹ as well as prepulses with a duration ranging from nanoseconds to subpicoseconds. The latter were achieved by inserting a drilled mirror²⁰ or guiding segments of the beam through an optical delay line.^{21,22}

Those techniques suffer from several basic disadvantages. The energy of the ASE within a laser amplifier chain may be varied only in narrow limits. Also, the temporal distance between the ASE and the main pulse is difficult to

control. Consequently, neither energy nor time dependencies can be investigated in a useful manner.

If parts of the laser beam are coupled into a delay unit through a hole in one mirror or by obscuring a part of the beam, diffraction patterns on subsequent optics are produced. At intensities of more than 100 GW cm⁻² even in the non-focused beam the intensity enhancement caused by the diffraction patterns is often sufficient to destroy optical elements. To get the desired very high intensities on target one needs to focus the laser beam to a very narrow spot of only a few microns in diameter. Sufficient spatial overlap of the foci of the prepulse and main pulse over the entire range of the delay between both pulses is essential for successful experiments. A possibility discussed in Ref. 20 is the enlargement of the focal point of the prepulse. However, that results in a decrease in the maximal possible prepulse intensity. Our fully automated device for the generation of a prepulse in a multi-TW Ti:sapphire amplifier chain presented here allows the generation of tight foci for pre- and main pulses with excellent spatial overlap even on a sub-10 μm scale, a large dynamical range for both pre- and main pulse intensities, and does not generate undesired intensity peaks in the laser system.

II. DESIGN OF THE PREPULSE UNIT

The prepulse device is implemented in a CPA Ti:sapphire system which consists of an oscillator, stretcher, a regenerative amplifier, two additional multipass amplifiers, and a vacuum compressor and is capable of delivering about 1 J in 80 fs with a repetition rate of 10 Hz.

Figure 1 shows the design of the prepulse device which is located between the regenerative and the first multipass amplifier. The main advantage in this case is the relatively low intensity of the laser beam at this position in the amplifier chain.

^{a)}Electronic mail: ziener@qe.physik.uni-jena.de

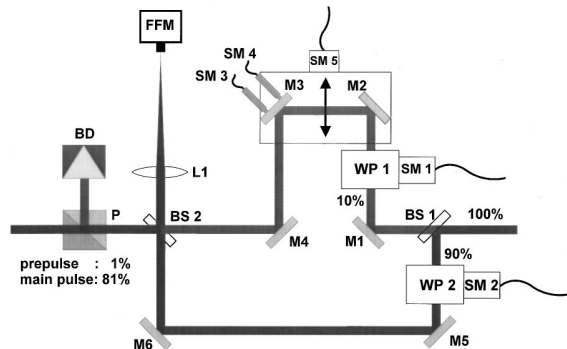


FIG. 1. Design of the prepulse unit.

The beam coming from the regenerative amplifier which has an energy of about 2 mJ, a pulse duration of 150 ps, and horizontal polarization is split into two beams with an intensity ratio of 9:1 at beam splitter BS1 so that 90% of the energy is reflected as the main beam. This beam is then sent through the rotating half wave plate (WP2), passes the mirrors (M5 and M6), beamsplitter BS2, which is identical to BS1, and the polarizer (P).

The plane of polarization of the main beam when it hits the polarizer can be adjusted by turning WP2 by means of the stepping motor (SM2). The polarizer transmits only the part of the beam with horizontal polarization, which is then amplified in the two succeeding multipass amplifiers to a energy of up to 1.3 J.

The polarization of the prepulse, transmitted by BS1, can also be turned with the help of half wave plate WP1 (stepping motor SM1).

Mirrors M2 and M3 are on a translation stage driven by stepping motor SM5. Mirror M3 itself can be turned around the horizontal and vertical axes by means of stepping motors SM3 and SM4. The temporal distance between the prepulse and main pulse can be adjusted in the range of -350 ps to +100 ps with an accuracy of 6 fs given by the step size of the translation stage stepping motor. Negative delay means that the prepulse hits the target before the main pulse.

The direction of both pulses can be routinely checked by the far field monitor (FFM). Polarizer P is also used for cleaning the prepulse in terms of polarization.

All stepping motors are controlled by a computer. The programs are written in LABVIEW.

III. CHARACTERISTICS OF THE PREPULSE UNIT

In order to characterize the prepulse unit the stability and pulse duration after transmission through the device, the dynamic attenuation range, and the stability of the spatial overlap between pre- and main pulses were investigated. Figure 2 shows the spectrum of the front-end oscillator of our Ti:sapphire laser after transmission through a true-zero-order half wave plate and the polarizer. The parameter is the orientation of the half wave plate. Obviously the spectrum does not change over three orders of magnitude of attenuation. The bandwidth of the system consisting of the half wave plate and polarizer is therefore large enough to attenuate the laser pulse by three orders of magnitude without modification of

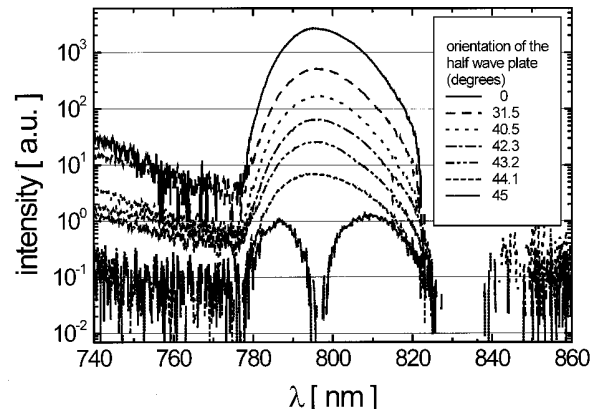


FIG. 2. Spectrum of the front-end oscillator after transmission through a half wave plate and a polarizer. The parameter is the orientation of the half wave plate. Background is not subtracted. The spectrum of the laser remains unchanged for an attenuation of 3 orders of magnitude.

the spectrum. That was also verified by pulse duration measurements of the amplified and recompressed pulse with a third order autocorrelator, and they show no increase in the pulse length or change in temporal pulse shape.

Figure 3 shows the energy of the amplified pulses. It can be seen that the main pulse, which has an energy of more than 300 mJ, may be attenuated by 1 order of magnitude and the prepulse by 1.5 orders of magnitude by rotating half wave plates WP2 and WP1, respectively. The change in the maximum attenuation factors for both pulses is due to the not completely saturated amplification in the multipass amplifiers which follow the prepulse device. Good spatial overlap of the foci of prepulse and main pulse is very important for all experiments especially for tight focusing. It has to be constant over the entire possible range of the prepulse delay (a more than 5 cm travel of the translation stage).

In order to check the spatial overlap the following experimental setup was used (see Fig. 1): A HeNe laser was coupled into the delay line through the first beamsplitter (BS1). After the second beamsplitter (BS2) the laser was focused by a lens (focal length 220 mm) onto a screen. The position of the focus on the screen only depends on the di-

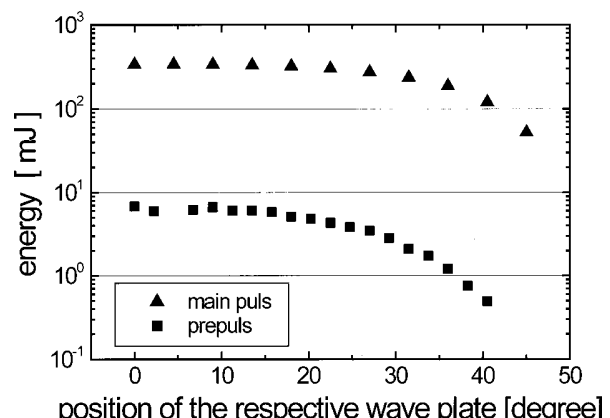


FIG. 3. Energy of the amplified prepulse and main pulse depending on the position of the respective half wave plate. Prepulse energies were measured with a third order autocorrelator and main pulse energies with an energy meter.

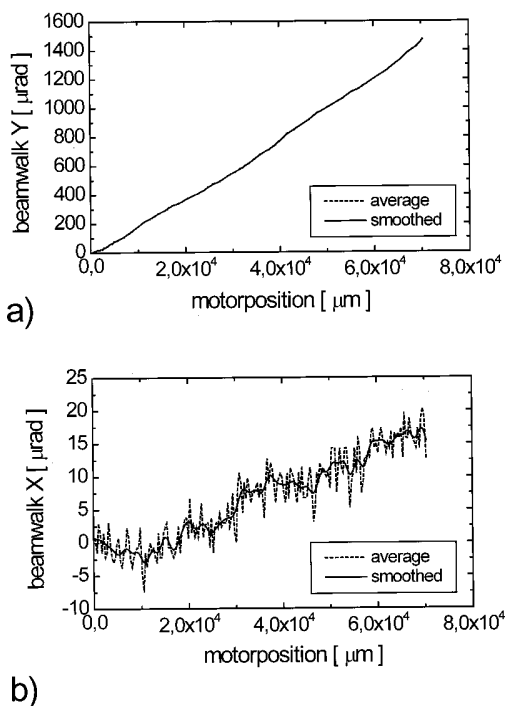


FIG. 4. Measured beamwalk of the HeNe laser beam (a) in the x direction and (b) in the y direction if the translation stage has been moved over the entire range. Measured data are an average over two measurements. The smoothed data are the resulting correction file for the automatic correction.

rection of the laser beam and does not change with a parallel shift of the beam. The focal point was captured with a charge coupled device (CCD) camera, and the picture was grabbed and analyzed with image processing software which was also written in LABVIEW.

The position of the focal point in the case of position 0 of SM5 was the reference. At every position of the translation stage, the focus was adjusted to the reference by means of stepping motors SM3 and SM4. The position of each motor (SM3, SM4, and SM5) was written into a file.

Figure 4 shows the measured deviations in μrad . Note the different scales of the two axes. The large deviation in the vertical direction is mostly due to elastic deformation of the whole prepulse unit as discussed below. The measurement was repeated several times and the results were averaged. Since the high-frequency parts of the measured fluctuations [see Fig. 4(b)] are mainly due to noise of the HeNe laser and the image processing, the correction file was made by smoothing the raw data.

The beam direction is now corrected as follows: The software automatically extracts the positions of SM3 and SM4 belonging to the respective position of stepping motor SM5 from the correction file and adjusts mirrors M3 and M4.

Figure 5 shows a test of the correction file. In this case, the translation stage was moved over 60 mm in increments of 0.3 mm and the respective position of the HeNe focus was measured. The variation of the beam orientation is about 20 μrad in the x direction and about 30 μrad in the y direction. The correction of the beam position is actually even more precise than shown in Fig. 5. The amplified Ti:sapphire laser was focused into the target chamber by an off-axis

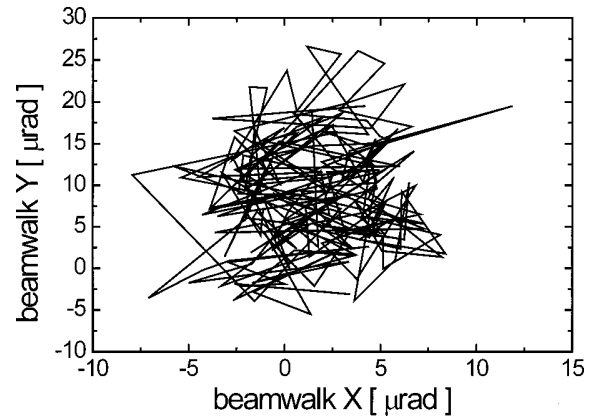


FIG. 5. Test of the correction file with the HeNe laser. Each point represents the deviation of the laser beam in the x and y directions for one particular delay. The tested distance of the translation stage was 60 mm (60 000 steps) with an interval of 0.3 mm (300 steps).

parabolic mirror with a focal length of 102 mm. The focal point had a full width at half maximum (FWHM) of 7 μm . The position of the foci of the prepulse and main pulse differed less than 1.5 μm over the entire range of the translation stage. That means the two beams are parallel to each other in both the x as well as the y direction with an accuracy of better than 15 μrad .

The following example may serve as an illustration of the accuracy of the beam alignment. During our measurements with the parabolic mirror we used a small piece of aluminum as a beam stop. The weight of the block was sufficient to bend the whole prepulse unit and change the position of the focus by more than 5 μm , which means a misalignment of about 50 μrad . We now use only a piece of black paper to block the beam.

IV. PREPULSE DEPENDENCE OF THE $K\alpha$ EMISSION OF SILICON TARGETS

As the first application of the described prepulse unit we investigated the dependence of the $K\alpha$ emission of a laser produced plasma of a silicon target on the temporal distance between the prepulse and main pulse. The experimental setup used was the following: The laser beam was focused onto the polished silicon target by an off-axis paraboloid ($f=163$ mm, 30°). The focal point was 9 $\mu\text{m} \times 55 \mu\text{m}$ in size. The intensity of the main pulse on the target was $(8 \pm 2) \times 10^{16} \text{ W cm}^{-2}$. Electrons in the plasma, accelerated by the laser field, generate $K\alpha$ radiation in the cold silicon bulk. The $K\alpha$ radiation is monochromatically focused onto a x-ray sensitive photodiode by a toroidal bent crystal (quartz 100).²³ The diode is protected against low energy radiation by a 7 μm thick beryllium window. The background was measured when the bent crystal was turned out of the Bragg angle by several degrees. The radiation measured under these conditions originates from hard x rays or fast electrons and did not exceed 25% of the diode signal in the Bragg peak.

Figure 6 shows the measured Si $K\alpha$ emission depending on the prepulse delay. The background was measured in each case and subtracted. Every single point represents an average over four laser shots, error bars are the mean error.

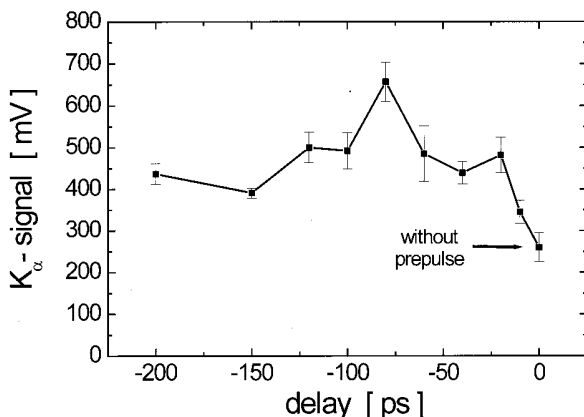


FIG. 6. K_{α} emission of the silicon target for a main pulse intensity of $(8 \pm 2) \times 10^{16} \text{ W cm}^{-2}$ and a prepulse intensity of $(8 \pm 2) \times 10^{14} \text{ W cm}^{-2}$, respectively. The point at zero delay is the value without any prepulse. The line is only a aid to the eye.

It is evident that for a prepulse delay of approximately 80 ps the efficiency of the K_{α} emission exceeds the value without prepulse by a factor of 2 (the value at zero delay was measured with the prepulse blocked). The plasma that is created by the prepulse expands and cools down. Because the absorption of the laser pulse in the plasma depends strongly on several plasma conditions (most notably the electron density gradient) there is an optimal temporal delay between the prepulse and the main pulse for efficient K_{α} production.

V. DISCUSSION

We developed a unit which introduces a well defined prepulse in a multi-TW Ti:sapphire laser amplifier system. It was shown that both the prepulse as well as the main pulse can be attenuated in energy by more than 1 order of magnitude without influencing the pulse length or the temporal pulse structure. By automatic correction of the direction of the prepulse it is possible to overlap the foci of both pulses over the entire range of the possible prepulse delay.

In the first application the K_{α} emission of a silicon target could be increased by more than a factor of 2 compared

to the K_{α} emission without a prepulse. Further experiments and numerical simulations are planned to investigate the dependence of the K_{α} production from prepulse and main pulse intensity and the photon energy of the K_{α} emission (target material).

ACKNOWLEDGMENTS

The authors gratefully acknowledge technical assistance by F. Ronneberger and W. Ziegler.

- ¹D. Strickland and G. Mourou, Opt. Commun. **55**, 447 (1985).
- ²M. D. Perry and G. Mourou, Science **264**, 917 (1994).
- ³K. Yamakawa, M. Aoyama, S. Matsuoka, H. Takuma, D. N. Fittinghoff, and C. P. Barty, IEEE J. Sel. Top. Quantum Electron. **4**, 385 (1998).
- ⁴A. Antonetti et al., Appl. Phys. (N.Y.) **65**, 197 (1997).
- ⁵J. D. Kmetec, C. L. Gordon, J. J. Macklin, B. E. Lemoff, G. S. Brown, and S. E. Harris, Phys. Rev. Lett. **68**, 1527 (1992).
- ⁶A. Rousse, P. Audebert, J. P. Geindre, F. Fallières, J. C. Gauthier, A. Myslrowski, G. Grillon, and A. Antonetti, Phys. Rev. E **50**, 2200 (1994).
- ⁷C. Gahn et al., Appl. Phys. Lett. **73**, 3662 (1998).
- ⁸J. Yu, Z. Jiang, J. C. Kieffer, and A. Krol, Phys. Plasmas **6**, 1318 (1999).
- ⁹T. Feurer et al., Phys. Rev. E **56**, 4608 (1997).
- ¹⁰C. Gahn, G. D. Tsakiris, A. Pukhov, J. Meyer-ter-Vehn, G. Pretzler, P. Thirolf, D. Habs, and K. J. Witte, Phys. Rev. Lett. **83**, 4772 (1999).
- ¹¹K. B. Wharton et al., Phys. Rev. Lett. **81**, 822 (1998).
- ¹²P. A. Norreys et al., Plasma Phys. Controlled Fusion **40**, 175 (1998).
- ¹³G. Pretzler et al., Phys. Rev. E **58**, 1165 (1998).
- ¹⁴H. Chen, B. Soom, B. Yaakobi, S. Uchida, and D. D. Meyerhofer, Phys. Rev. Lett. **70**, 3431 (1993).
- ¹⁵W. Theobald, R. Hässner, C. Wülker, and R. Sauerbrey, Phys. Rev. Lett. **77**, 298 (1996).
- ¹⁶M. Zepf et al., Phys. Rev. E **58**, R5253 (1998).
- ¹⁷D. G. Stearns, O. L. Landen, E. M. Campbell, and J. H. Scofield, Phys. Rev. A **37**, 1684 (1988).
- ¹⁸M. M. Murnane, H. C. Kapteyn, and R. W. Falcone, Phys. Rev. Lett. **62**, 155 (1989).
- ¹⁹J. A. Cobble, G. T. Schappert, L. A. Jones, A. J. Taylor, G. A. Kyrala, and R. D. Fulton, J. Appl. Phys. **69**, (1991).
- ²⁰S. Bastiani, A. Rousse, J. P. Geindre, P. Audebert, C. Quoix, G. Hamiaux, A. Antonetti, and J. C. Gauthier, Phys. Rev. E **56**, 7179 (1997).
- ²¹T. Feurer, Appl. Phys. B: Lasers Opt. **B68**, 55 (1999).
- ²²J. Steingruber, S. Borgström, T. Starczewski, and U. Litzen, J. Phys. B **29**, L75 (1996).
- ²³T. Missalla, I. Uschmann, E. Förster, G. Jenke, and D. von der Linde, Rev. Sci. Instrum. **70**, 1288 (1999).

A thermoluminescence detector-based few-channel spectrometer for simultaneous detection of electrons and photons from relativistic laser-produced plasmas

R. Behrens^{a)}

*Physikalisch-Technische Bundesanstalt, Bundesallee 100, 38116 Braunschweig, Germany
and Institut für Optik und Quantenelektronik, Friedrich-Schiller-Universität, Max-Wien-Platz 1,
07743 Jena, Germany*

H. Schwoerer and S. Düsterer

*Institut für Optik und Quantenelektronik, Friedrich-Schiller-Universität, Max-Wien-Platz 1,
07743 Jena, Germany*

P. Ambrosi

Physikalisch-Technische Bundesanstalt, Bundesallee 100, 38116 Braunschweig, Germany

G. Pretzler and S. Karsch

Max-Planck-Institut für Quantenoptik, Hans-Kopfermann-Straße 1, 85748 Garching, Germany

R. Sauerbrey

*Institut für Optik und Quantenelektronik, Friedrich-Schiller-Universität, Max-Wien-Platz 1,
07743 Jena, Germany*

(Received 23 July 2002; accepted 29 October 2002)

A new method was applied to simultaneously measure the absolute energy- and angle-dependent emission of electrons (500 keV to 20 MeV) and photons (50 keV to 2 MeV) emitted by laser-produced plasmas. For this purpose, a newly developed few-channel spectrometer based on thermoluminescence detectors was used. The device measures the curve of depth dose values in a stack of different materials. The deconvolution of electron and photon spectra from the depth dose curve was performed using a computing algorithm based on a Bayesian inference using Gibbs sampling. Several characteristics of the measured particle spectra were investigated: The electron distribution function of the electrons was found to be describable by Maxwellian distributions in energy. The hot electron temperatures obtained (between 1.1 and 1.7 MeV depending on target material and thickness) are in accordance with well-known scaling laws. The angular emission of the electrons was found to be highly anisotropic with a maximum in the direction of the laser reflection (region of the target normal and parallel to the target surface) for a thick target and an additional maximum in the forward direction of the laser for a thin target. Conversion efficiencies depending on the material and thickness of the target for the conversion of laser light energy to relativistic electrons and of electrons to photons were determined to be up to 10% and 1%, respectively. © 2003 American Institute of Physics. [DOI: 10.1063/1.1532831]

I. INTRODUCTION

The investigation of plasmas produced by the interaction of ultrashort (100 fs) and ultraintense laser pulses with matter has obtained a new quality since laser intensities in excess of 10^{19} W/cm² are accessible. The alternating electrical field of the laser light is as high as 10¹¹ V/cm. This is high enough to rapidly field ionize atoms by barrier suppression ionization¹ so that the main pulse of the laser interacts with a plasma. Electrons in the plasma are accelerated to relativistic energies and collide with the rest of the plasma and with the solid target producing Bremsstrahlung.^{2,3} In addition, ions are accelerated by electric space-charge fields due to the separation of nuclei and electrons induced by the ponderomotive force. The duration of emission of energetic particles is about 1 ps. In order to compare existing theories of accel-

eration mechanisms within the plasma, a detailed measurement of all components emitted has to be performed. Due to the short duration and small size of the accelerating fields, the particle source is very brilliant both in spatial and temporal terms. This fact, together with the number of accelerated electrons on the order of 10^{12} – 10^{14} , leads to serious problems for conventional spectroscopic methods.

In these radiation fields, spectrometry using the pulse-height analysis technique is seriously impaired by dead-time and pile-up effects, as the typical detector dead time of an active counting detector (e.g., a high-purity-germanium detector) is about 1 μs. Since the energy of each individual particle has to be determined, the number of particles detected per laser pulse must be reduced to a maximum of one particle. This can be achieved by keeping a large distance and/or by providing a shielding between the laser plasma and detector. However, spectral information in the low-energy

^{a)}Electronic mail: rolf.behrens@ptb.de

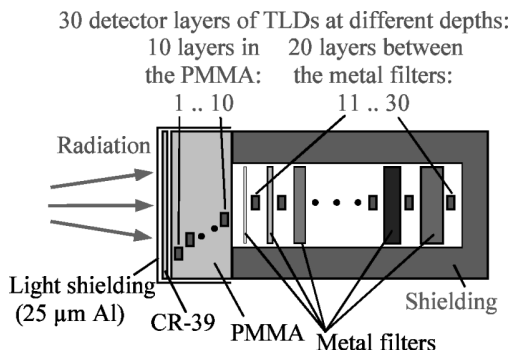


FIG. 1. Schematic assembly of the few-channel spectrometer. At the entrance of the spectrometer (left-hand side), a layer of CR-39 (nuclear track detector for detecting protons and ions) is mounted followed by a bulk of PMMA with TLD's embedded at different depths. Behind this, a stack of filters of different materials and thickness and TLD's is placed. Dimensions: About 21 cm in length and 7 cm in diameter; weight: About 7 kg.

region is lost by shielding. Furthermore, events induced by particles scattered in large shielding setups may complicate the analysis of the data obtained. In addition, the counting electronics are strongly disturbed by the great electromagnetic pulse caused by strong electrical currents in the plasma. In conclusion, a nonsaturable, parallel detection technique is required for characterizing relativistic laser plasmas.

The limitations just described can be overcome by measuring the total energy deposited by all incident electrons and photons (absorbed dose). In this case, spectral resolution is achieved by use of a set of differently filtered detectors and application of deconvolution techniques. The detectors are placed in a stack with filters of different thicknesses in between, leading to an increasing low-energy cutoff for each subsequent detector. This few-channel spectrometer allows the spectral fluences of pulsed electron and photon radiation to be simultaneously determined with moderate resolution, although the spectral resolution cannot compete with that of spectrometers employing pulse-height analysis.

To measure the absorbed dose in the different layers of the stack, thermoluminescence detectors (TLD's) were used. They consist of pieces of doped lithium fluoride (standard material TLD-700) which are about 4.5 mm in diameter and 0.6 mm in thickness. They are suitable for detecting fast pulsed radiation, since there is no evidence that their response depends on the dose rate (up to 10^{10} Gy/s). This is explained by the fact that the response of these detectors is based on the excitation of individual decoupled atoms. The angular dependence of the emitted radiation can be measured simultaneously using several few-channel spectrometers arranged around the focus of the laser. Due to the compact setup of the stack, the whole spectrometer is small enough to place up to 12 items around the laser focus within the vacuum target chamber.

II. CHARACTERISTICS OF THE FEW-CHANNEL SPECTROMETER

A schematic drawing of the few-channel spectrometer is shown in Fig. 1. The device consists of layers of different materials and thicknesses which are interspersed with TLD's. At its front (left-hand side in Fig. 1), a light shield and a

nuclear track detector are placed, followed by a region consisting of 4 cm of poly(methylmethacrylate) (PMMA). In the TLD's within the PMMA, most of the electrons are detected. Behind this layer, a region made up of 20 different metal filters is mounted where high-energy photons in particular are detected. This region is shielded with 5 mm of copper and 17 mm of lead to prevent radiation from penetrating through the side wall of the spectrometer into the TLD's. Further design and calibration details are given in Ref. 4. The interaction mechanisms for the different types of radiation are as follows:

- (1) To protect the TLD's from visible and ultraviolet light, they are shielded with an aluminum foil, 25 μm in thickness.
- (2) Ions and protons are detected by the nuclear track detector (CR-39, 750 μm in thickness). If these charged particles (in addition to electrons) get into the TLD's, they produce significant dose readings due to their large energy loss. In order to obtain dose values that are only due to electrons and photons, this effect must be taken into account: The amount of dose caused by ions has to be estimated from the readings of the CR-39 detectors and then subtracted from the dose measured in the TLD's.
- (3) Electrons with energies up to 300 keV are stopped in the aluminum and CR-39 where they produce a small amount of Bremsstrahlung that is detected by the TLD's.
- (4) Electrons with energies above 300 keV penetrate into the bulk of PMMA and produce the dose directly in the TLD's. In addition, they produce Bremsstrahlung that can penetrate into the region of the metal filters. Only electrons with energies higher than 9 MeV penetrate into the region of the metal filters.
- (5) Photons with energies above 3 keV penetrate into the bulk of PMMA and are detected by the TLD's.
- (6) Photons with energies above 20 keV produce significant doses in the TLD's placed between the different metal filters.

Consequently, the dose readings measured in the different detector layers result from a mixture of several dose contributions from different particles with different energies. Therefore, the deconvolution of the spectral fluence of electrons and photons requires knowledge of the dose response (dose reading per incident fluence) of all the detector layers to monoenergetic particles (response matrix). This response matrix was calculated using the Monte Carlo electron photon transport code EGS4 (Ref. 5) in the energy region between 10 keV and 100 MeV (for electrons) and between 3 keV and 100 MeV (for photons). Figure 2 shows the response matrix for electrons. The dose reading per incident fluence (on a logarithmic scale) depending on the electron energy is given. The different curves represent the responses for the different TLD layers starting with number 1 at the front of the spectrometer (see Fig. 1). The responses of the first 25 detector layers (that were used to evaluate the data) are shown. The fluctuations at low values of the response are due to a lack of computing time and, therefore, of a statistical nature. As can be seen, the low-energy electrons (below 0.3 MeV particle

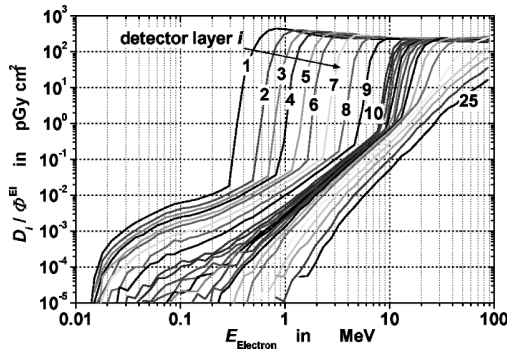


FIG. 2. Response matrix calculated for electrons with energies, E^{El} , between 10 keV and 100 MeV for the first 25 detector layers. Response D_i/Φ^{El} : dose, D_i , in detector layer i per incident fluence, Φ^{El} , on the front of the few-channel spectrometer. The fluctuations at low values of D_i/Φ^{El} are due to a lack of computing time and, therefore, of a statistical nature.

energy) produce only small dose values (equivalent to small response values) as just stated in point 3. According to point 4, electrons with energies above 0.3 MeV reach the TLDs and produce high response values in the TLD layers in the front of the spectrometer. Their penetration depth is deeper the higher their particle energy. An additional small amount of Bremsstrahlung is produced in the rear TLD layers (up to layer 25). Figure 3 shows the response matrix for photons. In this graph, no sharp bends as in Fig. 2 are seen. The reason for this is that photons do not have a finite penetration depth but a certain probability of penetration through a material layer without any interaction. As a result, with increasing photon energy, the response values increase up to 5 pGy cm^2 at about 0.01 MeV photon energy. The decrease at energies of about 0.1 MeV and the increase at higher energies are due to the conversion factor from photon fluence to dose. This factor behaves accordingly. At photon energies above 2 MeV, the curves of the first detector layers do not increase any more. This is due to the fact that in the layer in front of the corresponding TLD, not enough secondary particles (electrons) are produced by the incident photons to build up significant dose values. In other words: Due to their high particle energy, most of the photons penetrate through the front material of the spectrometer without any interaction and, thus, without producing dose values. An experimental check

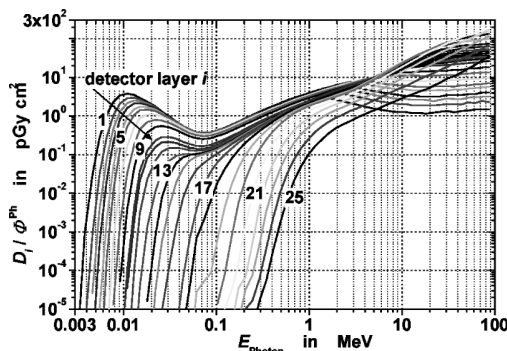


FIG. 3. Response matrix calculated for photons with energies, E^{Ph} , between 3 keV and 100 MeV for the first 25 detector layers. Response D_i/Φ^{Ph} : dose, D_i , in detector layer i per incident fluence, Φ^{Ph} , on the front of the few-channel spectrometer.

of the calculation of the response matrices was performed by irradiating the spectrometer in several well defined radiation fields of electrons and photons with different mean particle energies. The results were compared to corresponding calculations and agree within $\pm 20\%$. Further details are given in Ref. 4. To achieve good energy discrimination, the response curves for different detector layers must not be parallel. The reason is, that by this, the ratios of the dose readings in the different detector layers depend on particle energy. So, the set of ratios is characteristic of a certain particle energy. As can be seen in Figs. 2 and 3, this requirement is fulfilled for electrons with energies between 500 keV and 20 MeV and for photons with energies below 2 MeV. Nevertheless, in radiation fields with a large amount of low-energy particles (as from laser-produced plasmas), this fact cannot be used for energy discrimination because the dose values in the TLD layers in the front of the spectrometers are dominated by low-energy particles. It shall be emphasized that the responses were calculated for a broad range of values, namely from about 10^{-5} pGy cm^2 to about 10^2 pGy cm^2 , i.e., seven orders of magnitude, resulting in a long computing time (about five years of central processing unit time on a Pentium III 800 MHz) to minimize statistical fluctuations at low response values.

As the laser focus and thus the electron and photon source are approximately a point source, the response matrices were calculated for a divergent radiation beam for the approximate distance during the experiments (18 cm). If the distance between the front end of the spectrometer and the laser focus differs from 18 cm, the response matrix is corrected according to the quadratic decrease of dose with distance.

III. MEASUREMENTS

The laser plasma measurements were performed at two different multi-TW Ti:Sapphire laser systems in Garching and Jena. Both laser systems have a center wavelength of 800 nm and a repetition rate of 10 Hz. The pulse duration is 90 fs (in Jena) / 140 fs (in Garching) and the pulse energy 0.3 J (in Jena) / 0.6 J (in Garching). The pulses are focused with an $f/2$ parabola to a focal spot about $3 \mu\text{m}$ to $4 \mu\text{m}$ [full width at half maximum (FWHM)] in diameter. These parameters lead to a peak intensity that is averaged over the FWHM area of about $(1 \pm 0.5) \cdot 10^{19} \text{ W/cm}^2$. The incident angle with the target is 45° , and the polarization of the laser light was parallel to the plane of target normal and the laser direction.

The emission from targets with a different atomic number Z and different thicknesses of the same material was measured. In addition, several spectrometers were located around the target and the angular dependence of the particle emission was investigated. Detailed information about the targets is given in Table I of Sec. V.

During the experiment, the target was moved so that every laser shot hits a new part of the target surface. In order to obtain significant dose readings also in the rear detector layers of the few-channel spectrometers, the radiation from a

few thousand laser shots was accumulated for each run. The dose readings to be measured cover a huge range: From about 10^{-5} Gy ($10 \mu\text{Gy}$) in the rear layers to about 10^2 Gy in the front layers, i.e., seven orders of magnitude.

In Jena, the few-channel spectrometers were placed in the plane defined by the incident laser beam and the target normal. As too little space was available for the experiment in Garching, they were here located at about 20° to 25° below this plane.

IV. EVALUATION OF THE DATA

It is the objective of the measurement to obtain only the dose readings that are due to electrons and photons. Then, the mathematical relationship between the dose reading D_i in the detector layer i and the fluence of the electrons and photons in the energy group j , Φ_j^{El} and Φ_j^{Ph} , respectively, is given by

$$D_i = \sum_{j=1}^{53} R_{i,j}^{\text{El}} \cdot \Phi_j^{\text{El}} + \sum_{j=1}^{60} R_{i,j}^{\text{Ph}} \cdot \Phi_j^{\text{Ph}} \quad \text{for } i \\ = 1-30 \quad (\text{detector layers}), \quad (1)$$

where $R_{i,j}^{\text{El}}$ and $R_{i,j}^{\text{Ph}}$ denote the response (single values of the response matrices described in Sec. II) to electrons and photons, respectively. $R_{i,j} = D_i / \Phi_j$ represents the dose, D_i , in detector layer i per incident fluence, Φ_j , in the energy group j on the front of the few-channel spectrometer. The 60 energy groups are equidistant on a logarithmic energy scale. For electrons, the first seven energy groups (3 keV to 10 keV) are omitted, as in this energy region the response is zero.

To obtain good estimates of the fluences Φ_j^{El} and Φ_j^{Ph} , Eq. (1) must simultaneously be fulfilled for all 30 detector layers. This is the classical problem of few-channel deconvolution. As usual, this problem is mathematically underdetermined: More than one combination of fluences Φ_j^{El} and Φ_j^{Ph} fulfills Eq. (1). It is, therefore, helpful to have prior information about the fluences. The spectral distribution of electrons produced in a laser plasma is often assumed to be a classical Maxwellian distribution (as will be discussed next),^{6,7} usually with two parts of different Maxwellian temperatures.⁸ The Bremsstrahlung spectra arising from these electron distributions can be calculated and are obtained as an exponential decay.⁹ This prior information allows deconvolution of Eq. (1) using a computer code for parameter estimation. The code chosen performs a Bayesian inference using Gibbs sampling.¹⁰ This is performed by applying Markov chain Monte Carlo methods¹¹ (within the computer program WINBUGS).¹² The ansatz for the fluences of the electrons and photons is given by Eqs. (2) and (3), respectively, for three degrees of freedom (electrons in the plasma can be considered to be free particles, with the freedom to move in any direction). T_1 is considered the low-temperature value and T_2 is the high-temperature of a two-temperature distribution

$$\Phi_j^{\text{El}} = a_1^{\text{El}} \cdot (k \cdot T_1^{\text{El}})^{-3/2} \cdot \sqrt{E_j^{\text{El}}} \cdot \exp(-E_j^{\text{El}}/k \cdot T_1^{\text{El}}) \\ + a_2^{\text{El}} \cdot (k \cdot T_2^{\text{El}})^{-3/2} \cdot \sqrt{E_j^{\text{El}}} \cdot \exp(-E_j^{\text{El}}/k \cdot T_2^{\text{El}}), \quad (2)$$

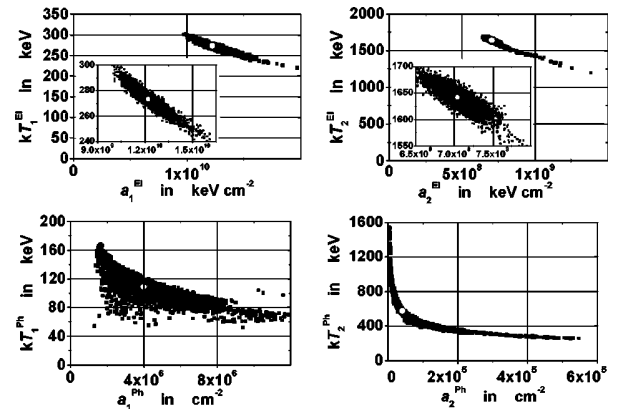


FIG. 4. Correlation between different parameters for 4500 iteration steps: Amplitude vs the corresponding temperature. The single dots represent the parameters chosen to determine the spectra.

for $j = 1$ to 53, and with E_j^{El} as the mean electron energy of the energy group j and

$$\Phi_j^{\text{Ph}} = a_1^{\text{Ph}} \cdot \exp(-E_j^{\text{Ph}}/k \cdot T_1^{\text{Ph}}) + a_2^{\text{Ph}} \cdot \exp(-E_j^{\text{Ph}}/k \cdot T_2^{\text{Ph}}), \quad (3)$$

for $j = 1$ to 60 and with E_j^{Ph} as the mean photon energy of the energy group j . k denotes the Boltzmann constant.

These eight free parameters (four amplitudes and four temperatures) have to be determined by deconvolution. The WINBUGS computer code needs regions in which the parameters may be varied and a starting value for each parameter. When the regions of the parameters were set, a side condition was taken into account: The total energy of the emitted radiation must not exceed the energy of the incoming laser light. For the spectrometers placed behind the thick targets, the values for $k \cdot T_2^{\text{El}}$ (high temperature) and a_2^{El} (corresponding amplitude) are set to zero, as only very few electrons can penetrate through the target.

In the measurements performed in this work, the dose readings in the rear detector layers (26–30) were very small. For the deconvolution, only the dose readings up to detector layer 25 were, therefore, taken into account (for experiment J1-Ta, only up to detector layer 22).

The computing algorithm is iterative. After a few hundred iterations (about 500), most of the parameters are stable. To make sure that convergence is achieved, 5000 iteration steps were performed. The iterated parameters for the amplitude and the corresponding temperature correlate strongly. This is plausible because a high temperature and a low amplitude result in almost the same absolute fluence in a spectrum as a low temperature and a high amplitude. This correlation is shown in Fig. 4. As the best estimate for the eight parameters, the median value of the iterated values (after the iteration had become stable) was chosen (dots in Fig. 4). In addition, Fig. 4 shows one of the major advantages of using the computer code WINBUGS for the data evaluation: The variation of the parameters to be optimized (e.g., the temperature of the Maxwellian distribution) during the iteration steps directly shows how “strong” the measured data are to fix the parameter. The standard uncertainty of the optimized parameter (median value) is given by the interval within

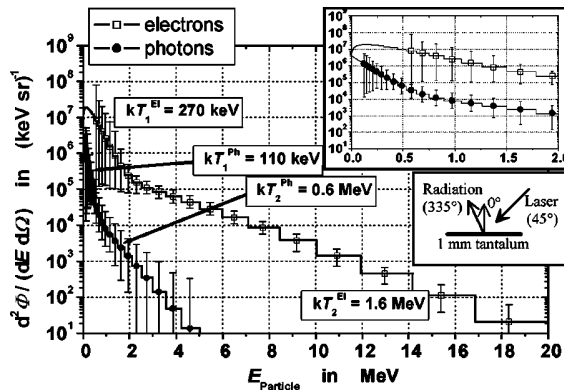


FIG. 5. Example of the spectral fluences per laser shot obtained from deconvolution. Target: 1.0 mm tantalum, 335° angle of emission. For very low particle energies the uncertainties become very large (\gg factor of ten). Therefore, no data points are shown but only the spectra [according to Eqs. (2) and (3)]. In the inset, the energy region up to 2 MeV is shown in detail.

which 63% of all the iterated values. The resulting uncertainties for the parameters are in line with the uncertainties of the fluence spectra determined independently of the data evaluation, see next. The spectral fluences (corresponding to Fig. 4) for electrons and photons with their uncertainties depending on the particle energy are given in Fig. 5. The direction in which the radiation was measured is given in the small inset. In the boxes of Fig. 5, the evaluated temperatures according to Eqs. (2) and (3) are given. The given uncertainties are mainly due to the uncertainty of the dose measurements (about 20% in the dose range between 0.01 and 0.1 mGy, 5% in the range between 0.1 and 3 Gy, and up to a factor of 2 for doses above 3 Gy). The standard uncertainty of the spectra were determined so that the following applies: If approximate five coherent energy bins of the spectra were equally modified within the ranges given by the indicated uncertainties, this would result in a variation of the dose readings within the aforementioned uncertainty of the dose measurement. For very low particle energies (electrons below 0.5 MeV and photons below 0.1 MeV), no data points are given, as the uncertainty is larger than a factor of 100. Therefore, for these particle energies, only the values according to Eqs.

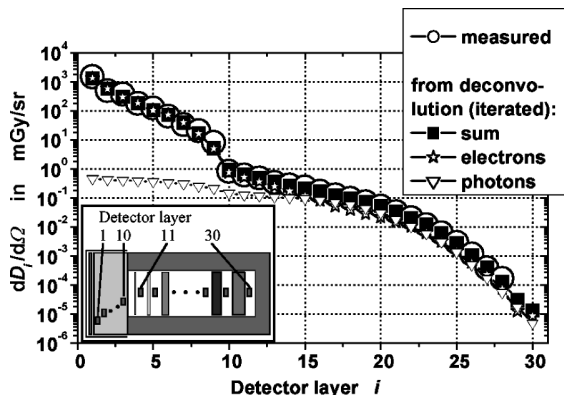


FIG. 6. Comparison of the measured dose values per solid angle, $dD_i/d\Omega$, per laser shot and the result of the deconvolution (depending on detector layer i) for the example given in Fig. 5. The iterated values are calculated from the fluence spectra [according to Eq. (1) with Eqs. (2) and (3)] for electrons and photons, respectively.

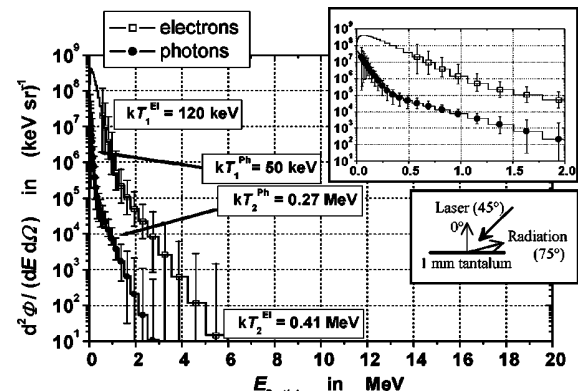


FIG. 7. Second example of the spectral fluences per laser shot obtained from deconvolution. Target: 1.0 mm tantalum, 75° angle of emission. For better comparison, the scales of Figs. 5 and 7 and of Figs. 6 and 8 are the same.

(2) and (3) are indicated by the solid line. Figure 6 shows the comparison of the measured dose readings and the dose readings calculated from the spectra shown in Fig. 5 that were obtained by the deconvolution. In the inset, the locations of the detector layers are shown. It can be easily seen that the result of the deconvolution fulfills Eq. (1). This clearly shows that the choice for the model functions is appropriate and, therefore, the simultaneous measurement of electrons and photons is indeed possible with the method presented.

In Fig. 6, it can also be seen that the iterated dose contribution, due to electrons, dominates. In contrast to this example, Fig. 7 shows the spectra from a measurement where the dose contribution due to photons is larger. As indicated in Fig. 7, the spectra were measured at a different angle of emission. The corresponding dose readings are shown in Fig. 8. It can clearly be seen that the contribution from electrons is dominant only in the first five detector layers. The uncertainty of the electron spectrum shown in Fig. 7 is, therefore, larger than the uncertainty for the electron spectrum shown in Fig. 5, and vice versa for the uncertainty for the photon spectra. In general: The most dominant type of radiation has the smallest uncertainty. Nevertheless, the uncertainties obtained are small compared to the broad range of fluence values (eight orders of magnitude).

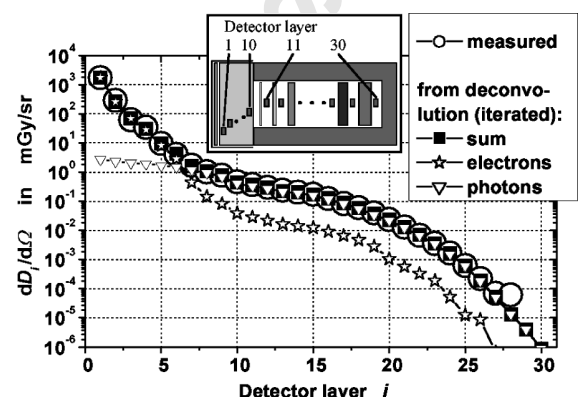


FIG. 8. Comparison of the measured dose values per solid angle, $dD_i/d\Omega$, per laser shot and the result of the deconvolution (depending on detector layer i) for the example given in Fig. 7.

The figures given for the temperature values (see boxes in Figs. 5 and 7) are directly taken from the output of the WINBUGS computer code: For electrons, the temperature of the classical Maxwellian distribution, see Eq. (2) and for photons, the temperature (slope) of the exponential decay, see Eq. (3). As just shown, the values for temperature and amplitude are correlated. This leads to an uncertainty for the presented temperatures of up to 50%. The high uncertainties apply especially to the temperatures of those photon spectra, for which the dose readings are dominated by dose readings due to electrons, as just mentioned.

For other applications (e.g., measurement of photon Bremsstrahlung spectra from pulsed particle accelerators or pulsed x-ray tubes), different models can be applied in the place of Eqs. (2) and (3), depending on the specific *a priori* information. If no *a priori* information is available, a mathematical basis, e.g., a set of Gaussian curves, may be used to represent the particle spectra.

V. RESULTS

A. Charged particles

As can be seen in Fig. 1, a layer of CR-39 track detector is placed in the front of the spectrometer to detect protons and ions. Such detectors were used during experiments in Jena. In no direction of emission was a significant number of particle tracks observed. As a result, no correction for the influence of the heavy charged particles on the dose readings in the TLD's had to be performed. All the dose readings are due to electrons and photons. In the Garching experiments, no CR-39 foils were used. It is assumed that no ions and protons with energies high enough to penetrate through the 25 μm of aluminum (e.g., above 1 MeV for protons) were present as in Jena.

B. Electron distribution functions

In literature, electron distribution functions (EDF's), other than the classical Maxwellian one given by Eq. (2), are proposed: They are of the form $\exp(-[E^{\text{El}}/k \cdot T^{\text{El}}]\mu)$ with $\mu \in (1-2.5)$.¹³ Also, the fully relativistic Maxwellian distribution of the form $(E^{\text{El}})^2 \cdot \exp(-E^{\text{El}}/k \cdot T^{\text{El}})$ is proposed in Ref. 14. These two options were included in the model function of Eq. (2), and the deconvolution was performed again. The results are as follows: Model functions with $\mu > 1$ are not capable of exactly fulfilling Eq. (1), i.e., the experimental data cannot be described by such a model. Model functions with the fully relativistic Maxwellian distribution are capable of fulfilling Eq. (1). In this case, the temperature is significantly lower (e.g., about 1 MeV instead of 1.5 MeV) than in the classical Maxwellian EDF as stated in Ref. 14. Nevertheless, in the energy region between 1 and 10 MeV, the resulting electron spectra are almost the same. This shows that the results of the deconvolution are almost independent of the choice of the model functions. This is another strong indication for the usefulness of the method employed for data evaluation. For the aforementioned reasons, in this article, the classical Maxwellian EDF as given in Eq. (2) is used to

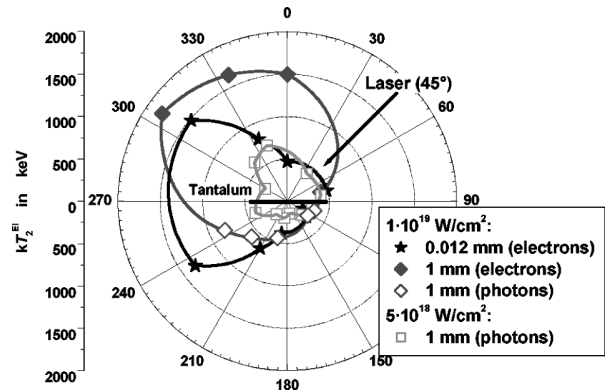


FIG. 9. Angular dependence of the hot electron temperature for tantalum targets of different thickness derived from the measured electron and photon spectra as indicated.

evaluate the data. This leads to electron temperatures about 20% below the temperature that would be obtained by an exponential fit to the spectra.

C. Electron and photon spectra

Figures 5 and 7 show typical results for the absolute spectral fluences of electrons and photons per laser shot (average of several thousand laser shots) in two directions of emission. The evaluated electron temperatures are in accordance with the well-known ponderomotive scaling law^{2,15} that predicts about 1 MeV at 10^{19} W/cm^2 . In addition, the evaluated photon temperatures are always significantly lower than the electron temperatures. This is plausible, as every electron produces a photon energy distribution that decreases with increasing photon energy and contains only very few photons at the initial energy of the electron.

D. Angular distribution of hot electron temperatures

To study the accelerating mechanisms in an fs laser-produced plasma, the angular distribution of the emitted radiation was determined via the measurement of the particle spectra (see Sec. V C). In Fig. 9, the obtained hot electron temperatures (evaluated according to the second last paragraph of Sec. IV) around solid tantalum targets are shown. At the rear side of the thick target, the dose readings due to electrons were too small to evaluate reasonable spectra, therefore, the photon spectra were used to determine a hot electron temperature (open symbols in Fig. 9). The values for the thick target (1.0 mm) at a laser intensity of 10^{19} W/cm^2 roughly reproduce the results of former measurements where the laser intensity was lower by about a factor of 2, namely $5 \times 10^{18} \text{ W/cm}^2$.³ These former measurements were performed with a predecessor version of the spectrometer that was only able to measure photon spectra. Accordingly, these data were evaluated via the measurement of photon emission also in front of the target. In both cases, a peak of the hot electron temperature occurs at an angle of 330°, between the target normal and the direction of the specularly reflected laser light. This behavior is explained by relativistic kinematics and described in detail in Ref. 3.

TABLE I. Physical parameters (lines 2 to 7), conversion efficiencies (lines 8 and 9), and hot electron temperature (line 10) for the experiments performed.

Line	Designation and target material Pulse energy in J Quantity	M1-PE ^a	M2-Cu	M3-Ta	J1-Ta	J2-Ta
		0.6	0.3			
2	Atomic number of target, Z	4.7	29	74	74	74
3	Thickness of target in mm	10	10	10	0.012	1
4	Macroscopic density of target in g/cm ³	1.06	8.9	16.7	16.7	16.7
5	Electron density of target in 10 ²⁴ /cm ³	0.32	2.4	4.1	4.1	4.1
6	Continuous-slowing-down approximation (CSDA) range ^b of electrons with 2 MeV in mm	10	1.6	0.96	0.96	0.96
7	Radiation yield ^b for electrons with 1 MeV	0.0026	0.02	0.06	0.06	0.06
8	Measured efficiency of conversion from laser light energy to electron energy:	0.04	0.04	0.1	0.02	0.05
	$4 \cdot \pi \cdot \sum_j (\Phi_{j,\Omega}^{\text{El}} \cdot E_j^{\text{El}}) / E_{\text{Laser Light}}$ for $E_j \geq 0.5$ MeV					
9	Measured efficiency of conversion from electron energy to photon energy:	0.001	0.004	0.007	0.001 ^c	0.003
	$\sum_j (\Phi_j^{\text{Ph}} \cdot E_j^{\text{Ph}}) / \sum_j (\Phi_j^{\text{El}} \cdot E_j^{\text{El}})$ for $E_j \geq 0.5$ MeV					
10	Measured hot electron temperature in MeV	1.2	1.5	1.7	1.1	1.7

^aPolyethylene made of carbon and deuterium, (C₂D₄)n.^bData taken from the ESTAR database of the National Institute of Standards and Technology (NIST): <http://www.physics.nist.gov/PhysRefData/Star/Text/ESTAR.html>^cThis value was not taken from the range of angle of emission between 305° and 335° as no values with sufficiently small uncertainties were available here but from 360°.

In addition, the values for the thin tantalum target (12 µm) are shown. Beside the maximum at about 310° (similar to the thick target), a clear maximum arises in the forward direction of the incident laser. Such a maximum in the forward direction of the laser was observed in former experiments¹⁶ and can be attributed to forward accelerated electrons by Wake-Field¹⁷ or direct laser acceleration¹⁸ processes in the preplasma in front of the target. In addition, in this work, a direct comparison with the amount of radiation simultaneously emitted at the front side of the target is available for the first time. As the emerging radiation is not influenced by a thick target, this experiment is a direct measurement of the initial radiation emitted from the plasma.

E. Conversion efficiencies and hot electron temperatures

The measured fluence spectra were used to evaluate further characteristics of the emitted radiation. In the upper part of Table I, physical parameters for the different target materials used in the experiments are given. In the lower part of Table I, conversion efficiencies and hot electron temperatures are given. The values are taken as mean values of the spectrometer positions (mostly two items) in the range of the angle of emission between 305° and 335° (see Fig. 9 for the definition of the direction).

Comparing the thickness of the target with the CSDA range (line 3 and line 6), the targets of all experiments except for experiment J1-Ta can be considered to be thick targets: Electrons with energies up to 2 MeV particle energy are stopped in the targets. As can be seen in line 8, the measured conversion efficiency from laser light energy to electron energy lies between 2% and 10% for the different experiments.

In line 9, the measured conversion efficiencies from electron energy to photon energy are given. In line 10, the measured hot electron temperatures are stated. For all three values, the following trend is apparent: The conversion efficiencies and the electron temperature increase with increasing atomic number, Z, and with increasing target thickness. With respect to the atomic number, this trend is the same for the theoretical radiation yield given in line 7. As the target in experiment J1-Ta is a thin target, not enough material is present to produce as many high-energy particles as in the other experiments. For this reason, the conversion efficiencies and the temperature are lower than those obtained with the thick target. The values for the conversion efficiencies (lines 8 and 9) in experiments M3-Ta and J2-Ta (both thick tantalum targets) are different by a factor of 2. This correlates with the differences in the pulse energies (see top of Table I).

ACKNOWLEDGMENTS

The authors thank R. Nolte for the idea of using the WINBUGS code¹⁹ for data evaluation, M. Reginatto for the introduction to the use of the WINBUGS code, M. Ahlborn for the readout of thousands of TLDs, as well as F. Ewald and F. Ronneberger for their support in running the laser system in Jena.

¹S. Augst, D. D. Meyerhofer, D. Strickland, and S. L. Chin, *J. Opt. Soc. Am. B* **8**, 858 (1991).²G. Malka and J. L. Miquel, *Phys. Rev. Lett.* **77**, 75 (1996).³H. Schwoerer, P. Gibbon, S. Düsterer, R. Behrens, C. Ziener, C. Reich, and R. Sauerbrey, *Phys. Rev. Lett.* **86**, 2317 (2001).⁴R. Behrens and P. Ambrosi, *Radiat. Prot. Dosim.* **101**, 73 (2002).⁵W. R. Nelson, H. Hirayama, and D. W. O. Rogers, Report SLAC-265, Stanford Linear Accelerator Center, 1985.

- ⁶T. Schlegel, S. Bastiani, L. Gráemillet, J.-P. Geindre, P. Audebert, and J.-C. Gauthier, Phys. Rev. E **60**, 2209 (1999).
- ⁷S. Bastiani, P. Audebert, J.-P. Geindre, T. Schlegel, and J.-C. Gauthier, Phys. Rev. E **60**, 3439 (1999).
- ⁸U. Teubner, I. Uschmann, P. Gibbon, D. Altenbernd, E. Förster, T. Feurer, W. Theobald, R. Sauerbrey, G. Hirst, M. H. Key, J. Lister, and D. Neely, Phys. Rev. E **54**, 4167 (1996).
- ⁹G. McCall, J. Phys. D **15**, 823 (1982).
- ¹⁰A. F. M. Smith and G. O. Roberts, J. R. Statist. Soc. **55**, 3 (1993).
- ¹¹Edited by W. R. Gilks (Chapman and Hall, London, 1996).
- ¹²D. J. Spiegelhalter, A. Thomas, and N. Best, MRC Biostatistics Unit , (1999).
- ¹³A. B. Langdon, Phys. Rev. Lett. **44**, 575 (1980); P. Porshnev, G. Ferrante, and M. Zarcone, Phys. Rev. E **48**, 2081 (1993); S. A. Uryupin, S. Kato, and K. Mima, Phys. Plasmas **2**, 3100 (1995); E. Fourkal, V. Y. Bychenkov, W. Rozmus, R. Sydora, C. Kirkby, C. E. Capjack, S. H. Glenzer, and H. A. Baldis, Phys. Plasmas **8**, 550 (2001).
- ¹⁴P. A. Norreys, M. Santala, E. Clark, M. Zepf, I. Watts, F. N. Beg, K. Krushelnick, M. Tatarakis, A. E. Dangor, X. Fang, P. Graham, T. McCanny, R. P. Singhal, K. W. D. Ledingham, A. Creswell, D. C. W. Sanderson, J. Magill, A. Machacek, J. S. Wark, R. Allott, B. Kennedy, and D. Neely, Phys. Plasmas **6**, 2150 (1999).
- ¹⁵S. C. Wilks, W. L. Kruer, M. Tabak, and A. B. Langdon, Phys. Rev. Lett. **69**, 1383 (1992).
- ¹⁶Y. T. Li, J. Zhang, L. M. Chen, Y. F. Mu, T. J. Liang, Z. Y. Wei, Q. L. Dong, Z. L. Chen, H. Teng, S. T. Chun-Yu, W. M. Jiang, Z. J. Zheng, and X. W. Tang, Phys. Rev. E **64**, 046407 (2001).
- ¹⁷F. Amiranoff, S. Baton, D. Bernard, B. Cros, D. Descamps, F. Dorchies, F. Jacquet, V. Malka, J. R. Marquès, G. Matthieu, P. Miné, A. Modena, P. Mora, J. Morillo, and Z. Najmudin, Phys. Rev. Lett. **81**, 995 (1998).
- ¹⁸C. Gahn, G. D. Tsakiris, A. Pukhov, J. Meyer-ter-Vehn, G. Pretzler, P. Thirolf, D. Habs, and K. J. Witte, Phys. Rev. Lett. **83**, 4772 (1999).
- ¹⁹This software is available at <http://www.mrc-bsu.cam.ac.uk/bugs/welcome.shtml>

7.4 Weitere eigene Veröffentlichungen

R. Pausch, M. Heid, T. Chen, H. Schwoerer, W. Kiefer;
„Quantum control by stimulated Raman scattering“,
J. Raman Spectrosc. **31** 7-13 (2000).

H. Schwoerer, S. Düsterer, R. Sauerbrey;
„Novel applications of table top Tera-Watt lasers“,
Photonics Science News **5** (2), 52-58 (2000).

T. Feurer, A. Morak, I. Uschmann, C. Ziener, H. Schwoerer, E. Förster, R. Sauerbrey;
„An incoherent sub-picosecond X-ray source for time-resolved X-ray-diffraction experiments“,
Appl. Phys. B **72** (1), 15-20 (2001).

S. Düsterer, H. Schwoerer, K. Gäbel, R. Sauerbrey;
„Schnellere Computer mit EUV“,
Spektrum der Wissenschaft, September 2001, S. 78-80.

T. Feurer, A. Morak, I. Uschmann, C. Ziener, H. Schwoerer, C. Reich, P. Gibbon, E. Förster, R. Sauerbrey, K. Ortner, C. Becker;
„Femtosecond silicon K_α pulses from laser produced plasmas“,
Phys. Rev. E. **65**, 016412 (2001).

A. Nohe, G. Lermann, H. Schwoerer, W. Kiefer, J. Sawatzki, G. Surawic;
„High resolution/low wavenumber Fourier transform Raman spectroscopy with a rubidium vapor filter and a Ti:sapphire laser“,
J. Mol. Struct. **410-411**, 65-68 (1997).

W. Kiefer, G. Knopp, A. Materny, R. Pausch, M. Schmitt, H. Schwoerer;
„Femtosecond Spectroscopy on Simple Molecular Systems: Pump-Probe and CARS Techniques“,
Chinese Journal of Light Scattering, **9** (2-3), 45-46 (1997).

T. Chen, V. Engel, M. Heid, W. Kiefer, G. Knopp, A. Materny, S. Meyer, R. Pausch, M. Schmitt, H. Schwoerer, T. Siebert;
„Determination of wave packet dynamics by femtosecond time-resolved pump-dump-probe and four-wave mixing techniques“,
XXIVth European conference on molecular spectroscopy, Prag, 23.-28.8.1998,
Journal of Molecular Structure, **480-481**, 33-43 (1999).

T. Chen, V. Engel, M. Heid, W. Kiefer, G. Knopp, A. Materny, S. Meyer, R. Pausch, M. Schmitt, H. Schwoerer, T. Siebert;
„Femtosecond pump-probe and fourwave-mixing spectroscopies applied to simple systems“,
Vibrational Spectroscopy **19**, 23-31 (1999).

M. Heid, T. Chen, R. Pausch, H. Schwoerer, W. Kiefer;
„Ultrafast coherent control in the electronic ground state of a molecule,“
J. Chin. Chem. Soc. **47**, 637-645 (2000).

Lebenslauf

Heinrich Schwoerer

19.10.1964	geboren in Waiblingen, Baden-Württemberg verheiratet mit Dr. Burga Schwoerer, 3 Kinder
1971 - 1975	Besuch der Grundschule in Waiblingen
1975	Besuch des Salier-Gymnasiums in Waiblingen
1976 - 1984	Besuch des humanistischen Gymnasiums Christian Ernestinum in Bayreuth
29.6.1984	Allgemeine Hochschulreife
2.7.1984 -	Zivildienst im Rettungsdienst und Krankentransport des Bayerischen Roten Kreuzes in Bayreuth
31.10.1985	Studium der Physik an der Ruprecht-Karls-Universität in Heidelberg
1985 - 1991	Diplom in Physik mit einer experimentellen Diplomarbeit „Dynamik von Tunnelsystemen in KBr:KCN-Mischkristallen, Dielektrische Dispersion und Rotationsechos“, Ruprecht-Karls-Universität Heidelberg
25.9.1991	Wissenschaftlicher Mitarbeiter am Laboratorium für Physikalische Chemie der Eidgenössischen Technischen Hochschule in Zürich
1.10.1991 -	Verleihung des Titels Doktor der Naturwissenschaften durch die Eidgenössische Technische Hochschule Zürich mit einer experimentellen Arbeit „Spektrale Lochbrennmaterialien als hochauflösende Amplituden- und Phasenfilter für ultrakurze Laserpulse“
31.12.1994	Wissenschaftlicher Assistent am Institut für Physikalische Chemie der Julius-Maximilians-Universität Würzburg
19.12.1994	Wissenschaftlicher Assistent am Institut für Optik und Quantenelektronik der Friedrich-Schiller-Universität Jena
1.2.1995 -	
31.12.1998	
1.1.1999 -	
heute	

Ehrenwörtliche Erklärung

Ich erkläre hiermit, daß mir die Habilitationsordnung der Friedrich-Schiller-Universität Jena bekannt ist. Ferner erkläre ich, daß ich die vorliegende Arbeit ohne unzulässige Hilfe Dritter und ohne Benutzung anderer als der angegebenen Hilfsmittel angefertigt habe. Die aus anderen Quellen direkt oder indirekt übernommenen Daten und Konzepte sind unter Angabe der Quellen gekennzeichnet. Bei den experimentellen Arbeiten, ihrer Auswertung und Veröffentlichung haben mir die jeweiligen Mitautoren der Veröffentlichungen unentgeltlich geholfen.

Weitere Personen waren an der inhaltlich-materiellen Erstellung der Arbeit nicht beteiligt. Insbesondere habe ich hierfür nicht die entgeltliche Hilfe von Vermittlungs- bzw. Beratungsdiensten in Anspruch genommen. Niemand hat von mir unmittelbar oder mittelbar geldwerte Leistungen für Arbeiten erhalten, die im Zusammenhang mit dem Inhalt der vorgelegten Arbeit stehen.

Die Arbeit wurde bisher weder im Inland noch im Ausland in gleicher oder ähnlicher Form einer anderen Prüfungsbehörde vorgelegt.

Ich versichere, daß ich nach bestem Wissen die reine Wahrheit gesagt und nichts verschwiegen habe.

Jena, den 1. Juli 2002

Schlußbemerkung

Ich möchte zum Schluß all denjenigen danken, die meine Arbeit in den vergangenen siebeneinhalb Jahren gefördert und begleitet haben.

Es sind dies meine Diplomanden und Doktoranden Mario Heid, Tao Chen, Christian Ziener, Stefan Düsterer, Rolf Behrens, Christian Fauser, Giuseppe Sansone, Kay-Uwe Amthor, Volker Ulrich und Jonas Burghoff. Es ist eine Freude, sie zu lehren selbständig zu werden und nicht immer eine, sie gehen zu sehen. Zwei, die unsere gemeinsame Arbeit in besonderem Maße vorangetrieben haben, sind mir auch zu guten Freunden geworden: Roman Pausch und Friederike Ewald.

Ich danke Falk Ronneberger, Wolfgang Ziegler, Burgard Beleites und Andreas Morak, ohne deren verantwortungsvolle und gute Arbeit der große Jenaer Laser nicht zum beinahe stärksten der Welt geworden wäre.

Professor Wolfgang Kiefer danke ich dafür, daß er mir nach meiner Doktorarbeit die Möglichkeit geboten hat, in seinem Institut ein modernes Experiment zur zeitaufgelösten Molekülspektroskopie aufzubauen.

Ich danke Professor Hans-Christoph Wolf und Professor Klaus Witte für die sorgfältige und kritische Begutachtung dieser Arbeit.

Und schließlich danke ich sehr herzlich Professor Roland Sauerbrey, der mich als endlos sprudelnde Ideenquelle und mit stets großem Vertrauen unterstützt hat. Sein Spaß an der Physik wirkt stets ansteckend und anspornend und sein kluger Umgang mit seinen Mitarbeitern ist ein großes Vorbild.